School of Biosciences

Quantitative Optical Microscopy of Bio-nanostructures

Joseph Marc Douglas Bleddyn Williams
Supervisors: Prof. Paola Borri & Prof. Wolfgang Langbein

A thesis submitted in fulfillment of the requirements for the degree of Doctor of Philosophy

Biophotonics and Quantum Optoelectronics Group

Cardiff University

30-09-2019

Acknowledgements

Yn gyntaf, diolch i fy nheulu, a pob un sydd wedi fod o gymorth i mi dros y blynyddoedd, yn enwedig Mam, Dad, Celyn, Morgan a Rich, Weelyn a Dacu, Mama a Dats, Frank a Merle, Owen, y criw o'r Alban, a Millicent a Mabli am gadael i mi aros yn y ty dros dro! Diolch hefyd i'r teulu Willis, yn enwedig i Jonathan, ffrind hyd oes, a Gary - a wnaeth rhoi fi'r siawns i ddysgu mathemateg yn gywir tuag at diwedd ysgol, a cadw ar y trywydd gwyddonol yn ystod y blynyddoedd caled yna. Diolch hefyd i'm ffrindiau yn Caerdydd, yn enwedig Ally, Josh, Emily, Rory, Caerwyn, Iwan, Sarah, Dan, Tomo a Callum. Diolch i fy ffrindiau o Exeter, yn enwedig Iona a Florence, Alex a Rayko. Diolch i Prifysgol Caerdydd, mae hi di fod yn fraint mawr i allu astudio yma.

Special thanks to my supervisors Prof. Paola Borri and Prof. Wolfgang Langbein, both of whom are freakishly talented scientists, and inspirational role models, who have kindly offered me their considerable patience and support over these past 4 years.

Thanks to members within the Biophotonics and Quantum optoelectronics group, namely (and in no particular order) David and Alex mainly for your general help and our stupid conversations after meetings, Dr. George Zorinyants and Dr. Francesco Masia, both of whom helped me a great deal with MATLAB. Thanks to Dr. Lukas Payne, Dr. Yisu Wang, Dr. Attilo Zilli, Dr. Naya Giannakopoulou, Ryan Lewis, Sion Harlow, Jacob Pope and Dale Boorman for your help over the years and your great company in the lab!

Finally, thanks to the Engineering and Physical Sciences Research Council (EPSRC) and Cardiff School of Biosciences, who have given me the opportunity to carry out the work in this thesis (EPSRC DTA studentship [EP/M507842/1]).

List of Abbreviations

AuNP	Gold Nanoparticle
NP	Nanoparticle
DIC	Differential Interference Contrast
qDIC	Quantitative Differential Interference Contrast
FWM	Four Wave Mixing
JACoP	Just Another Colocalization Plugin
LSPR	Localised Surface Plasmon Resonance
CLEM	Correlative Light Electron Microscopy
EM	Electron Microscopy
ICPM	Interferometric Cross Polarisation Microscopy
BFE	Bright Field Extinction
FFT	Fast Fourier Transform
FWHM	Full Width Half Maximum
NA	Numerical Aperture
PS	Polystyrene
GPU	Graphics Processing Unit
A488	Alexa 488
A647	Alexa 647
DF	Dark field microscopy
PI	Photothermal Imaging
iSCAT	Interferometric scattering microscopy
QPI	Quantitative Phase Imaging

Contents

1 Introduction and Motivations 1

1.1 Linear optical microscopy of bio-nanostructures 1

1.2 Quantitative microscopy methods 3

1.3 Motivations and thesis highlights 5

1.3.1 Improving quantitative capabilities of qDIC analysis (incl. time course experiments) 6

1.3.2 Correlative extinction - fluorescence microscopy of nanoparticles 6

1.3.3 Improving quantitative data analysis tools (cross-correlation algorithm) 7

1.3.4 Application of qDIC to measure changes in lipid-membrane thickness due to AuNP heating 8

1.4 Thesis Outline 8

2 Background concepts 10

2.1 Extracting optical phase from DIC images with a phase bias 10

2.1.1 Extraction of absolute phase retardation from differential phase 12

2.2 Optical extinction of a gold nanoparticle 13

2.2.1 Dielectric function of Gold 13

2.2.2 Extinction cross sections 14

2.2.3 Extinction cross sections in the Rayleigh limit 15

2.2.4 Localised surface plasmon resonance (LSPR) 15

2.2.5 Extinction microsopy measurements 16

2.3 Nanoparticle photothermal heating 17

2.4 Metallic Nanoparticle heating in a dielectric medium 18

3 Materials and Methods 21

3.1 Correlative extinction, epi-fluorescence and FWM samples 21

3.1.1 10nmAuNP-SA(A488)-Bi-Tf(A647) in HeLa cells 21

3.1.2 15nmAuNP-PC-Tf(A488) in HeLa cells 21

3.1.3 40nmAuNP-SA-Bi-Tf(A647) in HeLa cells 22

3.2 Correlative epi-fluorescence and extinction samples 23

3.2.1 20nmAuNP-PC-Ab(A647) 23

3.2.2 10nmAuNP-SA(A488) 23
3.3 Samples used with qDIC 23
3.3.1 Supported Lipid Bilayers 24
3.3.2 Polystyrene Beads sample 24
3.3.3 SU-8 2000 Permanent Epoxy Negative Photoresists 24
3.3.4 Lipid bilayer with Gold nanoparticles 24
3.4 Glass cleaning 25
3.4.1 Dropcasting nanoparticles 25
3.4.2 Nanoparticle sedimentation (controlled NP density on piranha etched glass) 25
3.4.3 Spin coating of Nanoparticles 25
3.4.4 Addition of immersion oil into imaging gasket via a Teflon tube 25
3.5 Experimental setups 27
3.5.1 Cameras 27
3.5.2 qDIC 28
3.5.3 Extinction and Epi-Fluorescence 28
3.5.4 Nanoparticle heating setup and alignment 29

4 Quantitative DIC: Results and discussion 30
4.1 Polynomial Background correction 33
4.2 Apodization 34
4.3 Region exclusion 40
4.4 Flip Method 42
4.5 3D processing 44
4.6 Balancing 44
4.7 In-band k-filter 44
4.8 Time course functionality 47
4.8.1 Example of time course (Polystyrene beads) 47
4.9 Energy Minimisation 51
4.10 Extracting Thickness from samples 57
4.10.1 SU-8 Waveguide 57
4.10.2 Lipid bilayers 58

5 Correlative Extinction, Epi-fluorescence and FWM microscopy 60
5.1 Quantitative data analysis: Cross-correlation 60
5.2 Experimental results 63
5.3 Correlative wide-field fluorescence and extinction microscopy of 20nmAuNP-PC-Ab(A647) and 10nmAuNP-SA(A488) 66
5.4 FWM and fluorescence correlation results 69
5.4.1 10nmAuNP-SA(A488)-Bi-Tf(A647) 70
5.4.2 15nmAuNP-PC-Tf(A488) 72

5.4.3 40nmAuNP-SA-Bi-Tf(A647) 73

6 Nanoparticle Heating **76**

6.1 Experimental results 77

7 Conclusions and Outlook **83**

A qDIC Theory: Jones matrix formulation **85**

A.1 Variable Retarder 86

B Image rotation code **88**

C Normalised cross-correlation algorithm (Pearson's coefficient) **90**

Bibliography **95**

List of Figures

2.1 Optical setup of a De Sénarmont configured microscope. 11
2.2 qDIC imaging of SU-8 waveguide. 12
2.3 Calculated surface plasmon absorption, scattering and total extinction efficiencies of gold nanoparticles with diameters of 20nm,40nm,80nm 16
2.4 Image method used to derive the temperature distribution originating from a heat source facing a surface. 20

3.1 Equipment required for creating a sample chamber to enable sequential addition of immersion media. 26
3.2 Arrangement for sample chamber to enable sequential addition of immersion media. 27
3.3 Optical path of the nanoparticle heating setup. 29

4.1 Extracting absolute phase from supported lipid bilayers. 31
4.2 Difference image between non-apodized and apodized phase (φ) images of supported lipid bilayers. 32
4.3 Extracting absolute phase from an SU-8 waveguide. 33
4.4 Polynomial background subtraction. 34
4.5 First step of the apodization process. 35
4.6 Result of the edge smoothing method for the extended image, for horizontal and vertical edges. 36
4.7 Corner array interpolation for the horizontal edge extension. 37
4.8 Corner array interpolation for the vertical edge extension. 38
4.9 Apodized images. 39
4.10 Results of the apodization for different smoothing rates. 40
4.11 Example of the region exclusion method. 41
4.12 Excluded region and smoothed arrays D_1,D_2,D_3 and D_4. 41
4.13 Merged arrays D_v, D_h and D. 42
4.14 Extending the δ image using the flip method. 43
4.15 Comparison between phase images (φ) produced with the flip method and apodization. 44

4.16 Profile of the in-band k-filter. 45
4.17 k-filtering for qDIC images of lipid bilayers acquired with a 100× objective with 1.5× multiplier. 46
4.18 Differential phase (δ) and phase (φ) image of the 100nm polystyrene beads sample. 48
4.19 Time course differential phase (δ) and phase (φ) image of the 100nm PS beads sample. 49
4.20 Retrieved polystyrene bead diameters from the contrast in figure 4.19. 50
4.21 Phase measured at the peak pixel value of signal corresponding to PS beads. 50
4.22 Synthetic bilayer-like phase and differential phase images. 52
4.23 Synthetic smooth object phase and differential phase images. 52
4.24 Error Δ_{BT} of the retrieved phase versus iteration number i of the energy minimization for the synthetic bilayer-like image with $S = |\nabla\varphi|^{\alpha}$. 53
4.25 As figure 4.24, but using $S = |\mathbf{u}^{\perp} \cdot \nabla\varphi|^{\alpha}$. 54
4.26 Error Δ_{BT} of the retrieved phase versus iteration number i of the energy minimization for the smooth object with $S(\nabla\varphi) = |\nabla\varphi|^{\alpha}$. . . 55
4.27 As figure 4.26, but using $S = |\mathbf{u}^{\perp} \cdot \nabla\varphi|^{\alpha}$. 56
4.28 Examples of phase profiles taken over bilayer edges. 58

5.1 The extraction of the central portion of a rotated image. 61
5.2 Cross correlation results from sample images. 62
5.3 Extinction images through focus for the 10nmAuNP-SA(A488) sample. 64
5.4 Fluorescence measured on 20nmAuNP-PC-Ab(A647) deposited onto a glass coverslip in air. 65
5.5 Fluorescence measured on 10nmAuNP-SA(A488) deposited onto a fused silica coverslip in air. 66
5.6 20nmAuNP-PC-Ab(A647) imaged by correlative wide-field fluorescence and extinction microscopy. 67
5.7 Cross correlation coefficient r_{P} as a function of relative translation (Δx,Δy) coordinates for the 20nmAuNP-PC-Ab(A647) construct shown in figure 5.6. 67
5.8 10nmAuNP-SA(A488) imaged by correlative wide-field fluorescence and extinction microscopy. 68
5.9 Cross correlation coefficient r_{P} as a function of relative translation (Δx,Δy) coordinates for the 10nmAuNP-SA(A488) construct shown in figure 5.8. 69
5.10 Correlative FWM and fluorescence microscopy of Fixed HeLa cells that have internalized 10nmAuNP-SA(A488)-Bi-Tf(A647). 71

5.11 Cross correlation coefficient r_P as a function of relative translation (Δx,Δy) and rotation ($\Delta\theta$) coordinates for the results on HeLa cells loaded with the 10nmAuNP-SA(A488)-Bi-Tf(A647) construct shown in figure 5.10. 72
5.12 Correlative FWM and fluorescence microscopy of Fixed HeLa cells that have internalized 15nmAuNP-PC-Tf(A488). 73
5.13 Cross correlation coefficient r_P as a function of relative translation (Δx,Δy) and rotation ($\Delta\theta$) coordinates for the results on HeLa cells loaded with the 15nmAuNP-PC-Tf(A488) construct shown in figure 5.12. 73
5.14 Correlative FWM and fluorescence microscopy of Fixed HeLa cells that have internalized 40nmAuNP-SA-Bi-Tf(A647). 74
5.15 Cross correlation coefficient r_P as a function of relative translation (Δx,Δy) and rotation ($\Delta\theta$) coordinates for the results on HeLa cells loaded with the 40nmAuNP-SA-Bi-Tf(A647) construct shown in figure 5.14. 75

6.1 Quantification of melting fingerprint and temperature profile. 76
6.2 Nanoparticle heating experiment. 78
6.3 Time course DIC performed on the AuNP with increasing laser irradiation powers. 79
6.4 Blister effect observed during NP heating experiment. 79
6.5 Time course phase image of blister after 128s. 81
6.6 Geometry of the AuNP photothermal heating experiment. 82

Summary of thesis

The work in this thesis was motivated by three main questions, namely: i) how far can quantitative differential interference contrast (DIC) microscopy be expanded and improved to accurately measure the thickness of single lipid bilayers, ii) do Gold nanoparticle-fluorophore conjugates provide a stable and reliable dual probe for correlative imaging studies, iii) can DIC offer a label-free quantitative method to accurately measure the surface temperature of a Gold nanoparticle (AuNP). To address the first question, a software has been developed which extracts optical phase information from a specimen imaged with differential interference contrast. A Wiener filtering approach is used to integrate the differential phase contrast image, to obtain an optical phase image of the specimen. The quality of Wiener filtered images is improved through the use of an apodization process to produce a two dimensional window around the differential phase image similar to the Hann window often used in one dimensional Fast Fourier Transform algorithm. Additionally, an energy minimisation routine further improves the quality of the retrieved phase images. From results presented in this thesis, it has been shown that one can perform the energy minimisation algorithm on multiple images in parallel with varied parameters. Images reach a converged status after approximately 10^7 iterations. To perform 10^7 iterations on graphics processing units (GPUs), it takes approximately 72 hours. To address the second question, following the acquisition of a series of confocal fluorescence and four wave mixing (FWM) amplitude images from bioconjugated fluorescently labelled AuNPs in Naya Giannakopoulou's thesis [1], a cross-correlation algorithm has been developed to quantify the Pearson's coefficient for lateral shifts between these images. To accommodate for any angular discrepancies between these images, a further algorithm was developed in order to rotate images relative to one another so that cross the images may be cross correlated. Pearson's coefficients from cross correlated images showed a lack of colocalisation between FWM amplitude and fluorescence images of HeLa cells loaded with AuNP-fluorophore constructs, generally resulting in values $r_\mathrm{P} < 0.05$ (apart from one instance where $r_\mathrm{P} = 0.15$) which confirms what was qualitatively reported in [1]. A direct study of the correlation between extinction and epi-fluorescence images of AuNP-fluorophore constructs prepared (washed) as per manufacturer specification and deposited onto a glass surface was subsequently performed. The cross cor-

relation of extinction and epi-fluorescence images from a 10nm AuNP-fluorophore construct (10nmAuNP-SA(A-488)) gave Pearson's coefficients $r_{\mathrm{P}} < 0.06$ for 1× and 3× washes, clearly indicating that the supposedly attached fluorophores are not reliable reporters of the NP location. Conversely, 20nm diameter AuNPs covalently bound to fluorescently labelled antibodies revealed a good degree of colocalisation with the fluorophore ($r_{\mathrm{P}} = 0.476$) after 3× washes. To answer the third question, a AuNP heating set-up was developed, using the qDIC imaging method outlined in this thesis. Briefly, a lipid bilayer was overlaid above a AuNP bound to a coverslip, and was photothermally heated at the localised surface plasmon resonance (LSPR). The heat which dissipates from the AuNP induces a phase transition in the lipid bilayer in its vicinity. By locating the phase boundary in the lipid bilayer, one can quantitatively measure the surface heating of the AuNP. In principle, the precise location of a phase boundary in a lipid bilayer is observable in qDIC. However, the dynamics observed through acquiring a qDIC time course did not resemble the behaviour previously observed in fluorescence measurements [2]. In particular, it is hypothesized that a blister effect occurred during resonant photothermal heating of a 50nm AuNP at the LSPR, lifting the lipid bilayer and generating an apparent thickness change.

Chapter 1

Introduction and Motivations

1.1 Linear optical microscopy of bio-nanostructures

For decades, the use of fluorescent labels in the context of bioimaging has yielded insights into the intricacies of cell biology. Fluorescent antibody labelling [3] and/or protein labelling through genetic encoding via the green fluorescent protein (GFP) [4][5] and its derivatives [6], alongside technology developments in far field and near field fluorescence imaging, have allowed microscopists to achieve sensitivities at the single molecule level, with high spatio-temporal resolution and high chemical specificity. In terms of lateral spatial resolution, conventional optical microscopy is limited by diffraction (Abbe limit) of the order of $\lambda/2\mathrm{NA}$, where λ is the wavelength of light and NA is the numerical aperture of the imaging lens. For visible light and high NA objectives this is roughly 200 nm. Recently, various methods have been developed to overcome this limit and optically resolve nano-objects. The most high-profile examples of far-field super-resolution bioimaging methods which can resolve biological systems at the nanoscale by means of fluorescence labelling are stimulated emission depletion microscopy (STED), [7][8] stochastic optical reconstruction microscopy (STORM), [9] and photoactivated localization microscopy (PALM).[10] These breakthrough techniques were awarded the Nobel prize in Chemistry in 2014. Total internal reflection fluorescence microscopy (TIRF) [11] is also a widely used near-field method to achieve nanoscale resolution in the axial direction through the limited penetration depth of the evanescent wave, and can be combined with in-plane localisation microscopy PALM/STORM methods.[12]

A drawback of organic fluorescent probes is photo-bleaching with associated chemical degradation and phototoxicity which has led to searching more stable solid-state inorganic alternatives such as quantum dots, or carbon-based nanoparticles such as nanodiamonds.[13] Still, fluorescence emission from these systems is known to exhibit instabilities, e.g. on/off 'blinking' behaviors depending on the local chemical environment, limiting the ability to use them for quantitative intensity analysis. To that end, there has been increasing interest in searching optical labels that exhibit robust and stable optical properties alternative to fluorescence. Gold nanoparticles (AuNPs) are unique in that they have strong optical absorption and scattering (i.e. extinction) properties that derive from the localised surface plasmon resonance (LSPR). This resonance originates from a coherent oscillation of conduction-band electrons about the ion core in the metal, where the restoring force is due to the electric field created by the corresponding charge displacement. In turn, the LSPR frequency and linewidth is a function of the shape and size of the AuNP and its dielectric environment, and can be tuned accordingly.[14]. AuNPs are also suitable for tagging in cell biology applications as they are chemically inert and have low-toxicity, which renders them biocompatible. They are relatively easy to fabricate in a variety of sizes and shapes, and can be readily functionalised with polymers, ligands, surfactants, biomolecules etc. [15][16] Fluorescently labelled biomolecules such as antibodies, peptides, nucleotides or protein ligands can be attached to AuNPs to create AuNP-fluorophore conjugates. These in turn are very powerful dual-probes where the cell entry and subsequent intracellular fate of these systems can be tracked in real time and *in situ*, through the use of fluorescence microscopy of the fluorescent molecule combined with e.g. dark-field scattering microscopy and/or electron microscopy of the AuNP. Due to their biocompatibility and functionalisibility, AuNPs are also used as vehicles for drug delivery, broadening their application space well beyond tagging. [17] To that end, understanding the interactions between AuNPs (of various sizes) and the cell is key to probing the suitability of these nanostructures for drug delivery. Notably, AuNPs exhibit strong photothermal effects (ie absorption of light converted into heat) and have been exploited for hyperthermal treatments. Generally, AuNPs have been widely utilized in biomedical applications, [18] [19] and cancer therapies, [20] also through their controllable toxicity with the aid of functionalisation. [21]

Besides nanoparticles, important nanostructures naturally occurring in biology are membrane bilayers. They have been the subject of many investigations by means of fluorescence microscopy. Fluorescence labelling has also been used for fluidity and hydration measurements in lipid bilayers, [22] to probe lipid composition, [23] and to quantitatively analyse the extent of lipid ordered and disordered domain sizes.[24] Interestingly, the interaction between AuNPs and lipid membrane bilayers has been exploited recently, for example through the photothermal properties of AuNPs as a mean to locally perturb the membrane fluidity, and even create nanopores for cellular entry, by-passing endocytosis [25]. Fluorescently labelled lipid bilayers have been used to measure the photothermal surface heating of AuNPs through locating a solid/fluid phase boundary that occurs at a distance away from the nanoparticle upon heating which depends on the temperature profile around the AuNP. [2] Also for these studies, fluorescence microscopy introduces limitations for accurate quantitative analysis due to photo-bleaching. Moreover, fluorescent lipid probes might perturb the naturally occurring phase transition and partitioning behaviours.

To that end, it is important to develop alternative label-free quantitative optical detection methods.

1.2 Quantitative microscopy methods

In light of the shortcomings of fluorescence microscopy methods mentioned above, linear quantitative fluorophore-free methods for detecting nanostructures are needed to accompany the information gained from using fluorophore labels. A selection of methods capable of achieving this, specifically in the context of imaging lipid bilayers and/or AuNPs (which are the systems investigated in this thesis), are discussed below.

Dark field (DF) microscopy is a powerful method to detect strongly scattering objects such as AuNPs. It is based on illuminating the sample using a cone of light at high angles of incidence, and detecting the light which is scattered through a smaller angular range. In the absence of scattering objects, no incident light is collected, hence this technique offers very high contrast against a virtually black background. In the context of bioimaging with AuNPs, DF microscopy has been used to probe the nuclear uptake of peptide conjugated AuNPs and tracking during the full cycle of cancer cells from birth to division, [26] and in the study of the nanometric stepwise movements of molecular motors with AuNPs attached. [27] Furthermore, the endocytosis and intracellular trafficking of DNA decorated AuNPs has been probed using correlative fluorescence and dark field microscopy. [28] Due to the need to distinguish AuNPs against the endogenous scattering from the cellular structure, typically either large AuNPs are used in these studies (with diameters above 50nm), or nanoparticle aggregates are detected, rather than individual AuNPs. An alternative technique which is more sensitive to small individual AuNP is photothermal imaging (PI). [29][30][31] This is a method similar to differential interference contrast (DIC) in that it measures refractive index changes around photothermally heated nanoparticles, and has been used to track 5nm AuNPs in live COS7 cells. [32] PI is however not fully free from background, since endogenous organelles such as mitochondria have been shown to exhibit PI signals. [33] Moreover, PI typically lacks high axial spatial resolution and, in turn, 3D localisation precision. [34] To probe the correlation of fluorescence with the optical extinction from AuNP-fluorophore conjugates, Interferometric scattering microscopy (iSCAT) [35] [36] and interference cross-polarisation microscopy (ICPM) [37][38] have been used. By being sensitive to the linear optical extinction, these techniques are also not free from background originating from debris and/or cellular structures in the samples. Moreover, they require complicated optical instrumentation for interferometric detection. In comparison with these imaging modalities, bright field extinction (BFE) - a method developed in the Biophotonics and Quantum optoelectronics group at Cardiff University [39][40][41] - is a simpler widefield technique. This is the method also used in this thesis and described in details in Chapter 3 and 5. Importantly, the method is capable to provide the *magnitude* of the optical extinction cross-section in absolute units and as a function of wavelength, therefore offering a powerful quantitative readout that can be correlated with the AuNP size and shape. [42] Whilst BFE, DF, PI and ICPM have their limitations in that they are not background free methods. Four Wave mixing (FWM) has been shown to be a highly precise microscopy method in probing the non-linear optical responses from single nanostructures.[43][44][45] FWM microscopy was also recently demonstrated by the Biophotonics and Quantum optoelectronics group at Cardiff University, offering unprecedented background-free detection of single small AuNPs inside cells, owing to the highly specific origin of the FWM signal at the LSPR of AuNPs. [46][47][48]

The various examples of correlative bioimaging of biological systems mentioned above show how fluorescence and other bioimaging modalities can compliment each other. Yet, in those cases where the use of fluorophore labels raises the question of sample physico-chemical alterations, the implementation of fluorophore-free methods becomes essential. This is specifically true when imaging lipid membrane bilayers, whereby fluorophore lipid analogues are known to alter the lipid order and phase transition. Notably, beyond qualitative imaging, for these systems it is valuable to develop method able to extract quantitative information about, for example, the bilayer thickness and chemical composition. Notable examples of quantitative microscopy methods able to do that are mentioned below.

Quantitative Phase Imaging (QPI) methods which allow microscopists to view the optical phase distribution over an illuminated sample as an amplitude modulation in the image contrast produced [49] is increasingly being used for the study of nanoscale objects. The field of quantitative phase imaging covers a variety of imaging modalities. Some examples of QPI measurements of nanoscale objects are listed as follows: Diffraction phase microscopy was used to generate time-resolved topographic profiles of evaporating sessile droplets. [50] A quasi-2π holographic detection scheme has been used to image diatoms, Escheria coli bacteria and dendrititic spines. [51] Polystyrene nanoparticles and influenza A (H1N1) viral particles have been imaged using self assembled nanolenses around individual nanoparticles to increase contrast between scattered and background light via a holographic method. [52] The topographies of sickle red blood cells have been obtained through the use of wide field digital interferometry. [53]

Beyond optical methods, atomic force microscopy [54] [55] is widely used in topographical measurements and has also been used in order to extract quantitative information from phase transitions in lipid bilayers, a phenomenon experimentally investigated in this thesis. [56]

Whilst novel and increasingly sensitive methods of quantitative phase imaging are necessary and undoubtedly contribute to our understanding of nanometric objects exhibiting optical phase contrast, and related dynamics, it also important to use optical setups which are already widely available, and require minor or no instrument modifications. This is why a quantitative differential interference (qDIC) method developed by the Biophotonics and Quantum optoelectronics group has been further developed as part of this thesis (see section 1.3.1). Such a set-up had been previously used to measure the lamellarity of giant lipid vesicles [57] and to measure the sizes of a population of individual nanodiamonds. [58] This method is based on a widely used De Sénarmont DIC setup, and can provide topographical information from phase objects or detect individual nanopartcles such as polymer beads without the need of any harware modifications.

As mentioned already, AuNPs are promising drug delivery vehicles as well as optical labels, and also have interesting photothermal properties. Previously, methods by which one can quantitatively measure the surface heating of AuNPs have been conducted in a number of ways. These include i) studying the temperature dependent photoluminescence from Er^{3+} ions that are embedded in a thin film of $Al_{0.94}Ga_{0.06}N$, [59] ii) using a QPI method to probe refractive index changes around AuNPs,[60] and iii) making viscosity measurements around a heated AuNP using an optical trap. [61] Heated metallic nanoparticles have steep temperature gradients around them and optical setups which probe refractive index and viscocity changes in the vicinity of the AuNP are limited by low spatial resolution [2]. The refractive index and viscocity responses also become non linear at high temperatures. Interestingly, this is not a limitation when using lipid bilayers as effective thermometers [2]. In this thesis, qDIC is proposed as a method by which one can precisely measure the location of phase boundaries that occur due to the melting of the lipid bilayer around a photothermally heated nanoparticle, significantly increasing the accuracy of fluorescence measurements made previously [2] (see section 1.3.4).

1.3 Motivations and thesis highlights

The work in this thesis was motivated by three main questions: i) how far can the quantitative analysis capabilities of DIC be expanded and improved to accurately measure the thickness of single lipid bilayers, ii) do AuNP-fluorophore conjugates provide a stable and reliable dual probe for correlative studies, iii) can DIC offer a label-free quantitative method to accurately measure the surface temperature of a AuNP. I give below a short list of highlights from this thesis work addressing these questions.

In the context of recent literature, the work was partly inspired by the following specific papers.[38] studied the co-localisation between individual 10nm AuNPs conjugated with the fluorophore Alexa-633, using interferometric cross polarisation microscopy. They demonstrated that there was a significant lack of correlation between the spatial patterns from the fluorescence emitted by the Alexa-633 and the cross-polarised scattering from the AuNP, and in turn lack of co-localisation.

[2] used confocal fluorescence microscopy to measure the phase transition of a labelled lipid due to the photothermal heating of a single AuNP, and in turn to derive the NP surface temperature.

The work in this thesis aims to expand on these recent works, and demonstrate improved measurements and data analysis capabilities.

1.3.1 Improving quantitative capabilities of qDIC analysis (incl. time course experiments)

Previously, a 1D deconvolution method [62] has been used in order to extract optical path differences from samples imaged in DIC. There are various approaches that one can take in order to extract quantitative information from DIC images. Using Wiener filtering in the context of DIC imaging has previously been reported [63][64], though it has not been used widely as a means by which one can extract quantitative information from DIC images. Transport of intensity equations have also been used in order to extract optical path differences from samples [65], though the Wiener filtering deconvolution method provides a simple and fast method by which one can extract optical path differences from samples.

A 2D deconvolution algorithm was previously developed in-house to extract quantitative information from phase objects.[57] To improve the quality of the outputted data, the algorithm was developed further in this thesis. Development highlights include an apodization step, background subtraction, spatial frequency filtering, 3D stack integration, a modified energy minimization routine initially developed by Koos et al. [66] amongst other features. These developments are discussed in detail in Chapter 4.

1.3.2 Correlative extinction - fluorescence microscopy of nanoparticles

In the context of this thesis, we specifically investigated AuNP-fluorophore conjugates, by means of correlative optical extinction/fluorescence microscopy (see Chapter 5). This was motivated in part by a recent study using interferometric cross polarisation microscopy (ICPM) [37] to optically detect the extinction from 10nm AuNPs conjugated with a fluorescently labelled Alexa-633 streptavidin. The study demonstrated that there was a lack of spatial correlation between the detected fluorescence and optical extinction and therefore a lack of colocalisation of the AuNPs and the supposedly conjugated fluorophores.[38] Considering the widespread use of these conjugates in bioimaging, it is crucial to fully understand their integrity (or lack of), especially while trafficking inside cells, which led to the investigation of various constructs as described in Chapter 5 of this thesis. Notably, the work in [37] attributed the lack of correlation to fluorescence quenching near AuNPs, a known reported phenomenon detrimental for the use of AuNP-fluorophore conjugates as optical labels.[67][68][69] AuNPs-fluorophore conjugates are also common dual probes for Correlative Light Electron Microscopy (CLEM) where AuNPs give a strong contrast in EM due to the high density of electrons. Notably, the question about the integrity of a AuNP-fluorophore construct is also difficult to answer via CLEM which requires sample processing that might degrade the fluorescence emission.[70] These findings provided a motivation for using quantitative microscopy methods to further investigate the colocalisation between AuNPs and fluorophore tags.

A lack of colocalisation between confocal fluorescence and FWM amplitude signals from bioconjugated fluorescently labelled AuNPs [1] was qualitatively observed in fixed HeLa cells that have internalized 10nm AuNPs fluorescently labelled with Alexa647 (10nmAuNP-SA(A488)-Bi-Tf(A647)), (see section 3.1.1 for further details), fixed HeLa cells that have internalized 15nm AuNPs fluorescently labelled with Alexa488 (15nmAuNP-PC-Tf(A488)), (see section 3.1.2 for further details) and fixed HeLa cells that have internalized 40nm AuNPs fluorescently labelled with Alexa647 (40nmAuNP-SA-Bi-Tf(A647)), (see section 3.1.3 for further details). These experimental results were part of the work from a former PhD student in the Biophotonics group at Cardiff University. To further investigate these findings, a correlative study between the extinction and epi-fluorescence signals from individual AuNPs was performed experimentally and quantitatively analysed in this thesis (see Chapter 5).

1.3.3 Improving quantitative data analysis tools (cross-correlation algorithm)

When different microscopy setups are used to acquire images from the same samples (for example with modalities such as FWM, extinction, confocal fluorescence and epi-fluorescence) it is often difficult to accurately locate and overlay the same field of view for quantitative correlative analysis. There may be a discrepancy between the position of the sample within the field of view, for example the precise position of the objects under scrutiny may be translated or rotated with respect to an image of the same objects measured on a different microscope setup. Determining this correction is especially challenging in the absence of fiducials visible in multiple modalities. To account for such discrepancies, in this thesis an algorithm was developed to cross-correlate images with varying pixel shifts and angular rotations and, in turn, get a precise measure of the correlation (Pearson's coefficient) between images acquired with different microscopy setups. Note that the JACoP plugin freely available in the widely used ImageJ software may be used in order to get a Pearson's coefficient value for two images that are not shifted relative to one another, [71] i.e. it is assumed that they have been measured on the exact same field of view. Imagej plugins such as Coloc2 also do not allow the user to probe angluar rotations of images relative to one another when performing a correlation analysis. Hence, an algorithm needed to be developed in order to account for the positional discrepancies of the objects within the field of views from measurements acquired with different set-ups. Specifically, the extinction method used in this work combines brightfield images shifted laterally with respect to one another, and such images are correlated with fluorescence images of nominally the same field of view. Due to e.g. sample drift and/or different sample holders, one cannot reliably assume that the object under observation will have returned to or remained at the same location within the field of view after shifting the sample or after a fluorescence timecourse. Therefore, the development of such cross-correlation algorithm in this thesis proved essential to achieve a truly quantitative analysis of the integrity of AuNP-fluorophore conjugates, as discussed in Chapter 5.

1.3.4 Application of qDIC to measure changes in lipid-membrane thickness due to AuNP heating

Based on the experimental setup reported in the recent literature comprising a AuNP surrounded by a lipid bilayer, [2] it is possible to measure the surface temperature of AuNPs. The particle is resonantly irradiated, and the resulting temperature increase in its vicinity induces a phase transition at a distance away from the AuNP. The phase transition of the lipid bilayer is well characterised, and a temperature profile around an irradiated AuNP can be modelled [72], using the location of the phase boundary between the fluid and solid gel phase of the lipid bilayer and literature values for the relevant physical parameters. However, the precise position of the phase boundary is not clearly observed when imaging using fluorescence labels. Conversely, label-free qDIC may produce a reliable phase contrast which precisely shows the location of the phase boundary. In this thesis, such experiment was performed and analyzed as described in Chapter 6.

1.4 Thesis Outline

This thesis is organised as follows: **Chapter 2** provides background concepts and the formalism needed to understand the measurements and data analysis described in the result-focussed chapters. **Chapter 3** describes the sample preparation and the experimental setups used in this work.**Chapter 4** describes the qDIC workflow for acquiring DIC data and the post processing steps to obtain quantitative information from specimens. Three example specimens are discussed. **Chapter 5** focusses on verifying findings made in ref. [1] regarding the lack of colocalisation between confocal fluorescence and FWM signals from bioconjugated fluorescently labelled AuNPs. This chapter then discusses the follow-up study which I performed on the measurement of colocalisation between extinction and epi-fluorescence signal from fluorescently labelled AuNPs (the same type of nanoparticles used in [1]). **Chapter 6** Describes the experimental results obtained by the resonant photothermal heating of individual AuNPs embedded in a lipid bilayer on a planar glass surface, and their study by qDIC. It also features an example of a time course qDIC experiment.

Chapter 2

Background concepts

2.1 Extracting optical phase from DIC images with a phase bias

DIC microscopy is a widespread tool for observing transparent objects such as living cells and tissues. It measures the difference of the optical phase between two points in the sample plane, spatially separated by an amount typically comparable with the optical resolution. These changes in the optical phase are associated to changes in sample thickness and refractive index. In the following, I summarise the mathematical formalism necessary to understand the image formation in DIC, as a foundation to the quantitative DIC data analysis implemented in this thesis, and further discussed in Chapter 4. I used DIC with a de-Sénarmont compensator consisting of a polariser and a quarter-wave plate ($\lambda/4$) in the illumination beam path (shown in figure 2.1).

The elliptically polarised light which emerges after traversing the $\lambda/4$ waveplate is described as the following field vector [57]:

$$\mathbf{E_i} = \frac{\mathbf{E_0}}{\sqrt{2}} \begin{pmatrix} 1 \\ e^{i\psi} \end{pmatrix} \tag{2.1}$$

A schematic of the DIC optical elements is shown in fig. 2.1. Briefly, the Wollaston prism in the back-focal plane of the condenser lens splits the two polarization components in direction, resulting in a shift of the illumination in the sample plane. After propagation through the objective lens, the two beams are recombined by a Nomarski prism on the DIC slider, and pass through an analyzer, so that the final electric field is given by the Jones matrix expression:

$$\mathbf{E_{out}} = \frac{\mathbf{E_0}}{2\sqrt{2}} \begin{pmatrix} 1 & -1 \\ -1 & 1 \end{pmatrix} \begin{pmatrix} e^{i\varphi_+} & 0 \\ 0 & e^{i\varphi_-} \end{pmatrix} \begin{pmatrix} 1 \\ e^{i\psi} \end{pmatrix} \tag{2.2}$$

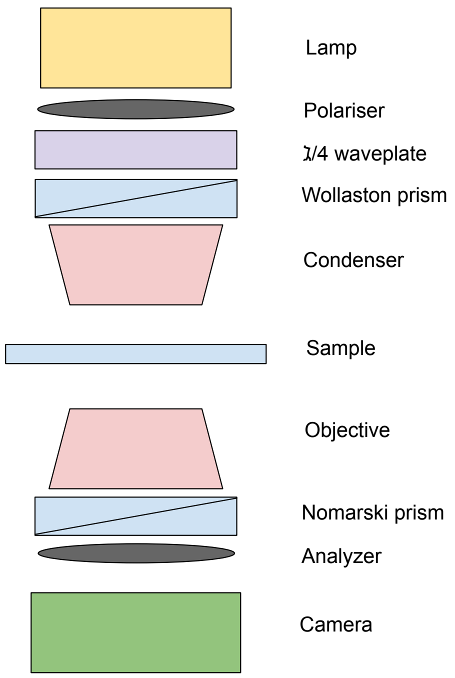

Figure 2.1: Optical setup of a De Sénarmont configured microscope.

which gives the following intensity at the camera:

$$I_{out}(\mathbf{r}, \psi) = \frac{I_{ex}}{2}[1 - \cos(\psi - \delta(\mathbf{r}))] \tag{2.3}$$

where I_{ex} is the excitation intensity, $\mathbf{r}$ is the position within the sample plane, ψ is the phase offset of the incident light see eq, 2.2, and $\delta(\mathbf{r})$ is the differential phase between two waves that are sheared by the Wollaston prism and (separated by the distance $|\mathbf{s}|$) traverse the sample:

$$\delta(\mathbf{r}) = \varphi(\mathbf{r} + \mathbf{s}/2) - \varphi(\mathbf{r} - \mathbf{s}/2) = \varphi_+ - \varphi_- \tag{2.4}$$

where $\mathbf{s}$ is the shear vector and φ is the optical phase. In order to extract the differential $\delta(\mathbf{r})$, one can create a contrast image with intensity I_c through imaging a sample with a positive phase offset $I_+(\psi_+)$ and then a negative phase offset $I_-(\psi_-)$. The contrast image is calculated as per eq. 2.5, which minimises the effect of non-uniform illumination of I_{ex}:

$$I_c(\mathbf{r}) = \frac{I_+(\mathbf{r}) - I_-(\mathbf{r})}{I_+(\mathbf{r}) + I_-(\mathbf{r})} \tag{2.5}$$

An example of the production of a contrast image I_c is seen in figure 2.2 **C**. $I_+(\psi_+)$ and $I_-(\psi_-)$ are shown in figure 2.2 **A** and **B** respectively. The sample shown is an SU-8 waveguide immersed in silicone oil (see section 3.3.3 for further details).

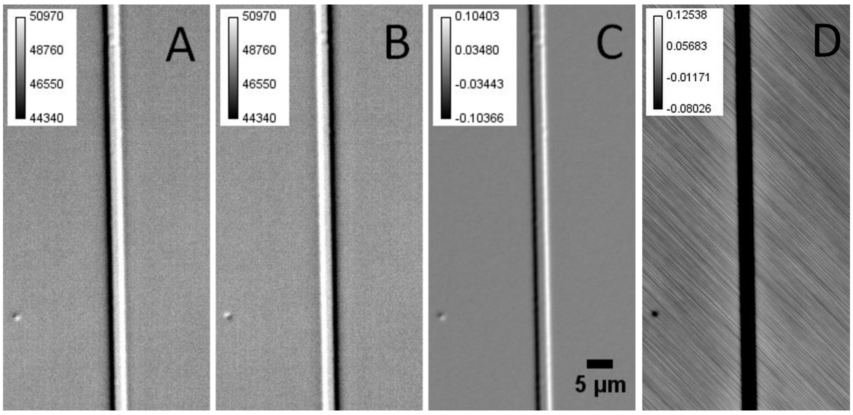

Figure 2.2: qDIC imaging of SU-8 waveguide. **A** Positive phase offset DIC image $I_+(\psi_+)$ of an SU-8 waveguide, **B** Negative phase offset DIC image $I_-(\psi_-)$ of the waveguide **C** Contrast image I_c of the waveguide (background corrected) **D** Phase image φ of the waveguide.

D shows a phase image of the waveguide in radians, details of how this image is retrieved from the contrast image **C** are detailed below. The SU-8 waveguide was imaged with an acquisition time of 50ms with 256 averaging, at a polariser angle of 45°. Note that a dark counts background image is subtracted from $I_+(\psi_+)$ and $I_+(\psi_+)$ before creating the contrast image I_c. A polynomial background subtraction may also be applied to I_c at this stage, for further details see section 4.1. I_c may also be expressed as the following:

$$I_c(\mathbf{r}) = -\frac{\sin(\psi)\sin(\delta)}{1-\cos(\psi)\cos(\delta)} \tag{2.6}$$

And $\delta(\mathbf{r})$ may subsequently be extracted with a known value of ellipticity angle ψ, if the following condition is satisfied:

$$0 \leq |\delta(\mathbf{r})| \leq |\psi| \leq \pi/2 \tag{2.7}$$

Through trigonometry we may extract δ from equation 2.6:

$$\sin(\delta) = -I_c \frac{1-\cos(\psi)\sqrt{1-{I_c}^2}}{\sin(\psi)} \frac{1}{1+I_c^2\cot^2\psi} \tag{2.8}$$

2.1.1 Extraction of absolute phase retardation from differential phase

δ as per eq. 2.4 and eq. 2.8 is a differential phase. The quantity that is of physical interest for quantification is the optical phase . To retrieve such integrated phase, we considered equation 2.4 in the Fourier domain. This is

$$\mathcal{F}[\delta] = 2i\sin\left(\frac{\mathbf{s}\cdot\mathbf{k}}{2}\right)\mathcal{F}[\varphi] \tag{2.9}$$

We can thus introduce the Fourier multiplier term:

$$\xi = 2i \sin\left(\frac{\mathbf{s} \cdot \mathbf{k}}{2}\right) \tag{2.10}$$

Where $\mathbf{s}$ is the shear vector introduced previously, and $\mathbf{k}$ is spatial frequency. To obtain the optical phase from δ one has to multiply $\mathcal{F}[\delta]$ with the term below and then make an inverse transformation:

$$G(\mathbf{k}) = \frac{1}{\xi + \frac{1}{\kappa \xi^*}} \tag{2.11}$$

the Fourier multiplier $G(\mathbf{k})$ incorporates a component in order to minimise artefacts that arise from dividing through 0 near $\mathbf{k} = 0$. This procedure is called Wiener deconvolution. κ is the signal to noise ratio parameter. An example of an integrated phase image (φ) of an SU-8 waveguide is shown in figure 2.2.

2.2 Optical extinction of a gold nanoparticle

During the 1850s, Michael Faraday was researching the interactions between light and matter, and in doing so he was preparing microsocope slides with gold sheets to be mounted on them. The gold sheets were prepared through chemical means for them to be thin enough to be transparent, since mechanical methods such as hammering produced gold sheets that were too thick. This process involved a washing step, which resulted in the production of a faint ruby fluid. This scattering phenomenon which causes the ruby colour of the suspension is referred to as the Faraday-Tyndall effect. In 1908, Gustav Mie solved Maxwell's equations with the appropriate boundary conditions in order to describe the interaction of a plane wave with a metallic nanoparticle. The optical properties of spherical gold nanoparticles are described below.

2.2.1 Dielectric function of Gold

The Fermi energy of Gold is in the 6sp band and the dynamics in this band can be described by the Drude-Sommerfeld model for a free electron gas. To gain an expression for the dielectric function of gold, the equation of motion for a single electron which interacts with an electric field is obtained, and this electronic response is multiplied by the number of electrons per unit volume. This results in the following expression for the dielectric function:[14]

$$\varepsilon(\omega) = 1 - \frac{\omega_p^2}{\omega^2 + i\gamma_b\omega} \tag{2.12}$$

the plasma frequency is given by $\omega_p = \sqrt{\frac{n_e e^2}{\varepsilon_0 m_e}}$, where ε_0 is the permittivity of free space, e is the charge of an electron, n_e is the number density of electrons and m_e is the effective mass of a conduction band electron. γ_b is the bulk damping constant, related to the Fermi velocity v_F and mean free path l via $\gamma_b = \frac{v_F}{l}$. The above expression does not adequately describe particles that have a diameter less than the mean free path, in order to do so a size dependent damping term is introduced.[14]

This model holds for frequencies up to the near infra-red. For optical frequencies a term is introduced, which takes into account the effects of interband transitions [14]:

$$\varepsilon(\omega) = \varepsilon^{ib} + 1 - \frac{\omega_p^2}{\omega^2 + i\gamma_b\omega} \tag{2.13}$$

2.2.2 Extinction cross sections

The interaction between a electromagnetic plane wave in a medium with permittivity ε_m and a spherical metallic nanoparticle is fully described by Mie theory [73] and provides the expression for the absorption and the scattering of light.

The optical cross section, given by the superposition of the scattering and the absorption from the particle, is called the extinction cross section, which can be expressed as the following [74]:

$$\sigma_{ext} = \sigma_{sca} + \sigma_{abs} \tag{2.14}$$

and equivalently

$$\frac{P_{ext}}{I_{inc}} = \frac{P_{sca}}{I_{inc}} + \frac{P_{abs}}{I_{inc}} \tag{2.15}$$

where I_{inc} is the illumination intensity, P_{abs} is the power absorbed, P_{sca} is the power scattered and P_{ext} is the power extincted. Due to the fact that the metallic particles are spherical in this treatment, P_{sca} and P_{ext} are independent of the polarisation state of the incident light. Mie theory provides the expressions:

$$\sigma_{sca} = \frac{2\pi}{k^2} \sum_{n=1}^{\infty} (2n+1)(|a_n|^2 + |b_n|^2) \tag{2.16}$$

$$\sigma_{ext} = \frac{P_{ext}}{I_{inc}} = \frac{2\pi}{k^2} \sum_{n=1}^{\infty} (2n+1)\mathrm{Re}\{a_n + b_n\} \tag{2.17}$$

for the case where the permeability of the particle and the surrounding medium are the same, a_n and b_n are expressed as

$$a_n = \frac{m\psi_n(mx)\psi_n'(x) - \psi_n(x)\psi_n'(mx)}{m\psi_n(mx)\xi_n'(x) - \xi_n(x)\psi_n'(mx)} \tag{2.18}$$

$$b_n = \frac{\psi_n(mx)\psi_n' - m\psi_n(x)\psi_n'(mx)}{\psi_n(mx)\xi_n'(x) - m\xi_n(x)\psi_n'(mx)} \tag{2.19}$$

where $\psi_n(\rho) = \rho j_n(\rho)$ and $\xi_n = \rho {h_n}^{(1)}(\rho)$ are Riccatti-Bessel functions.

2.2.3 Extinction cross sections in the Rayleigh limit

In the limit $\lambda >> 2\pi R$ where the particle diameter $2R$ is much smaller than the wavelength of the incident light (known as the Rayleigh limit) the expressions for the extinction of such particles may be simplified by treating the spherical NP as an ideal dipole.

For a sphere of radius R, the polarisation α given by the Claussius-Mossotti homogenisation[74] is:

$$\alpha = 4\pi R^3 \Big(\frac{\varepsilon_p - \varepsilon_m}{\varepsilon_p + 2\varepsilon_m} \Big) \tag{2.20}$$

ε_p is the permittivity of the metallic particle, and ε_m is the permittivity of the medium. The following expressions for the scattering and absorption cross sections apply:

$$\sigma_{sca} = \frac{k^4}{6\pi} |\alpha^2| = \frac{8}{3} \pi k^4 R^6 \Big| \frac{\varepsilon_p - \varepsilon_m}{\varepsilon_p + 2\varepsilon_m} \Big|^2 \tag{2.21}$$

$$\sigma_{abs} = k \ \mathrm{Im}(\alpha) = 4\pi k R^3 \ \mathrm{Im} \Big(\frac{\varepsilon_p - \varepsilon_m}{\varepsilon_p + 2\varepsilon_m} \Big) \tag{2.22}$$

where $k = 2\pi n_m / \lambda$ is the wave vector within the medium.

2.2.4 Localised surface plasmon resonance (LSPR)

When a metallic object is placed in an electric field, the electrons in the conduction band are driven by the external field and oscillate around the ion core. In driving the electrons away from the ionic core, the external electric field induces a dipole oscillation. Based on eq.2.21 and eq.2.22 for spherical particles, a resonance occurs at the frequency at which the real part of the dielectric function of the particle is double that of the medium's dielectric function ($\mathrm{Re}(\varepsilon_p) = -2\mathrm{Re}(\varepsilon_m)$), which results in a minimum denominator in eq.2.21 and eq.2.22 and thus maximum optical cross section. This resonance is called LSPR.

Plasmonic nanoparticles have relatively large extinction cross sections, owing to the fact that they have large electron densities. LSPRs are tunable by changing the size and shape of gold nanoparticles. [75][76] Broadly speaking, the frequency position of the LSPR is determined by the real part of the dielectric function, while the LSPR linewidth, related to the electron dephasing characteristics, is described by the imaginary part. [14] For small gold nanospheres up to 40nm, absorption effects dominate the extinction cross section which approximately scales with the volume of the NP [74][77], whilst scattering effects are more prominent in particles as the diameter is increased above 40nm. This can be seen in figure 2.3, where the extinction curve (in green) is similar to that of the abosorbion curve (red dashed) for particle diameters of 20nm and 40nm, while for the 80nm AuNP, the scattering cross section (black dotted) makes a larger contribution to the extinction cross section.

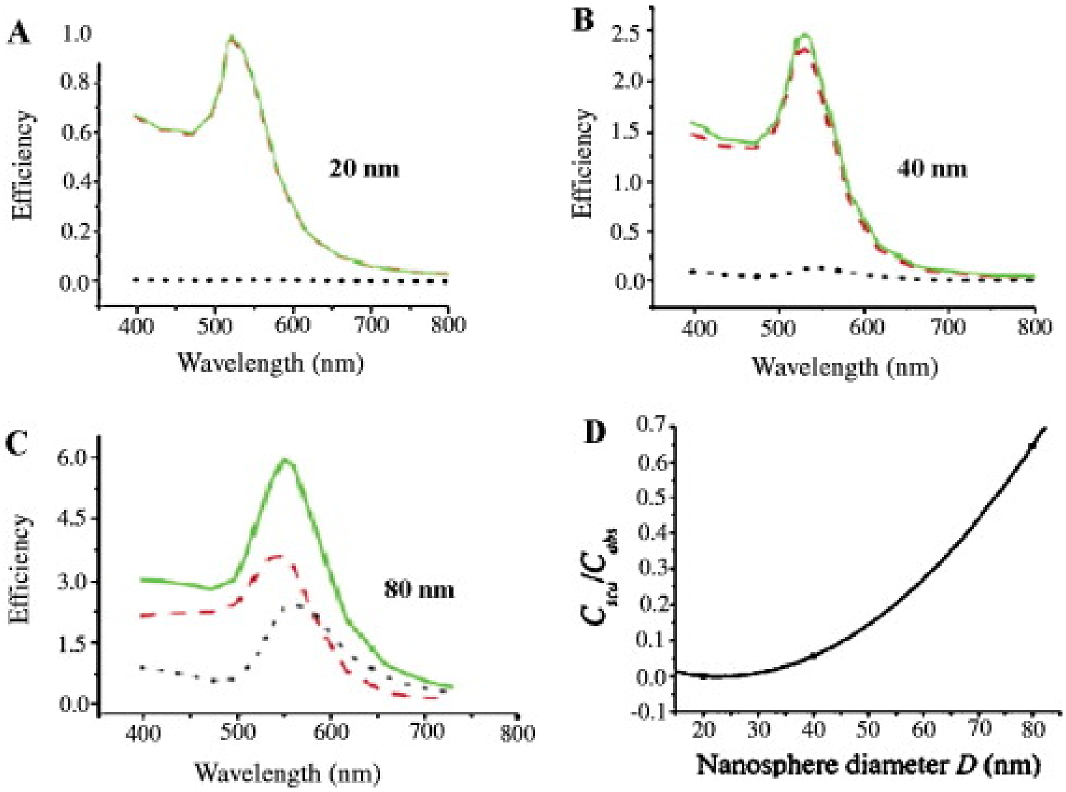

Figure 2.3: Calculated surface plasmon absorption, scattering and total extinction efficiencies of gold nanoparticles in diameter of (A) 20 nm; (B) 40 nm and (C) 80 nm. (D) Dependence of the ratio of the scattering to absorption cross-sections on the diameter of gold nanoparticles. Increasing particle sizes leads to increased contribution from Mie scattering. The calculations are made by using full Mie theory. (Reproduced with permission from Ref. [75].)

Note that absorption, scattering and extinction efficiencies are shown in this figure, these are defined as the ratio between the absorption/scattering/extinction cross section and the particle's geometric cross section.

2.2.5 Extinction microsopy measurements

A quantitative wide-field optical method of measuring the extinction cross sections of metallic nanoparticles has been developed within the biophotonics group by Prof. Borri and Prof. Langbein at Cardiff University. [39][40][41] It is based on a commercial transmission wide-field microscope set up (for details, see also Chapter 3). In order to obtain the necessary data, an extinction image Δ is measured (see eq.2.23) which is in essence a differential transmission image. This is obtained by taking a set of transmission images in bright field of an in focus metallic nanoparticle (corresponding to the term I_f in equation 2.23), and after shifting the stage by an amount larger than the observable influence of the point spread function of the nanoparticle(s) under scrutiny [78], acquiring the same amount of images in the shifted position to generate I_s. To reduce the amount of noise in the images, multiple images are averaged at each position, this reduces the photon shot noise by a factor of $1/\sqrt{N}$, where N is the number of images acquired. The extinction image is given by:

$$\Delta = 1 - \frac{I_f}{I_s} = \frac{(I_s - I_f)}{I_s} \tag{2.23}$$

To derive a value for the extinction cross section one needs to spatially integrate Δ:

$$\sigma_{\text{ext}} = \int_{A_i} \Delta dA \tag{2.24}$$

the area A_i corresponds to a disk with a radius $r_i = 3\lambda/2\text{NA}$ which is centred on the nanoparticle, λ is the excitation wavelength and NA is the numerical aperture of the illumination condenser matching that of the imaging objective used. This disk covers the area occupied by the first two Airy rings of the point spread function (PSF) of the objective. Further increasing the disk radius results in a saturation of σ_{ext}. This is due to the short spatial coherence length of the lamp illumination in the microscope $d_c \approx \lambda/\text{NA}$, a spatially coherent illumination source would give σ_{ext} fringes that would decay as $1/\sqrt{r}$. These are suppressed for $r > d_c$ under incoherent lamp illumination. [39]. Differences between I_f and I_s due to sample drift, defocusing or drift of illumination intensity can be accounted for by background correction. A local background extinction $\Delta_b = {A_b}^{-1} \int_{A_b} \Delta dA$ is obtained through integrating the extinction in the region A_b between r_i and $2r_i$, and correcting Δ for it as follows:

$$\sigma_{\text{ext}} = \int_{A_i} (\Delta - \Delta_b) dA \tag{2.25}$$

The images are shifted by a minimum distance of $2r_i$.

2.3 Nanoparticle photothermal heating

An analytical solution exists for a temperature profile around a plasmonic metallic particle on a glass interface which is illuminated by laser light [72]. As a result, an experimental setup reported in [2] used a lipid bilayer as an effective thermometer on the microscopic scale which gives a measure of the surface temperature of the metallic nanoparticle. The heat profile around the nanoparticle melts the lipid bilayer in the region where the temperature is above the phase transition threshold. To gain a measure of the surface heating of the metallic nanoparticle, the precise location of the phase boundary is required. In the reported experiment in [2] fluorophore labels are used which preferentially partition into the fluid phase, and the phase boundary is observed in fluorescence. In this thesis, we measured this phenomenon in DIC label-free. The quantitative DIC method is used as the phase transition can be imaged as a change in height of the bilayer thickness, which is detectable by qDIC as discussed in Chapter 4 and 6.

2.4 Metallic Nanoparticle heating in a dielectric medium

The heat transfer equation which describes the optothermal heating of NPs in a medium is as follows[79]:

$$\rho(\mathbf{r})c(\mathbf{r})\frac{\partial T(\mathbf{r},t)}{\partial t} = \nabla\kappa(\mathbf{r})\nabla T(\mathbf{r},t) + q(\mathbf{r},t) \tag{2.26}$$

where $\rho(\mathbf{r})$ is the mass density (as a function of position $\mathbf{r}$), $c(\mathbf{r})$ is the heat capacity, $T(\mathbf{r},t)$ is temperature (as a function of position $\mathbf{r}$, and time t), $\kappa(\mathbf{r})$ is specific heat and $q(\mathbf{r},t)$ is the time averaged local heat intensity, which accounts for the effect of light disspiation in the NP:

$$q(\mathbf{r},t) = \langle \mathbf{j}(\mathbf{r},t) \cdot \mathbf{E}(\mathbf{r},t)\rangle_t \tag{2.27}$$

where $\mathbf{j}(\mathbf{r},t)$ is current density and $\mathbf{E}(\mathbf{r},t)$ is electric field. If the nanoparticle is placed in a homogenous and isotropic medium and is in a steady state, equation 2.26 becomes[72]:

$$\kappa\nabla^2 T(\mathbf{r}) = -q(\mathbf{r}) \tag{2.28}$$

As there are no heat sources present in the medium equation 2.28 can be further reduced into the Laplace equation :

$$\nabla^2 T(\mathbf{r}) = 0 \tag{2.29}$$

An expression for $T(\mathbf{r})$ in the region outside the NP (of radius a) can be found through solving equation 2.29 in spherical coordinates. Temperature is taken to be constant within the NP at T_0:

$$T(\mathbf{r}) = \begin{cases} T_0 & : a \geq |\mathbf{r} - \mathbf{r_i}| \\ T_0 \frac{a}{|\mathbf{r}-\mathbf{r_i}|} & : a \leq |\mathbf{r} - \mathbf{r_i}| \end{cases}$$

Where $\mathbf{r_i}$ is the location of the NP. The temperature within the metallic nanoparticle is considered constant as the heat conductivity of the metal nanoparticle is much larger than that of the dielectric surrounding (e.g. water). The temperature profile outside the NP may be interpreted as analogous to the electrostatic Coulomb potential around a uniformly charged sphere within a homogeneous dielectric medium, as both physical setups may be described via the Laplace equation (equation 2.29).[80] This method of detecting surface heating of metallic NPs assumes that the power absorbed by the nanoparticle through laser irradiation is fully converted into heat power, and thus the total heat power can be derived through via an energy conservation equation:

$$Q = \int_{surface} -\kappa \nabla T(\mathbf{r}) \cdot d\mathbf{S} \tag{2.30}$$

which gives a value for T_0:

$$T_0 = \frac{Q}{4\pi\kappa a} \tag{2.31}$$

This is the surface temperature of the nanoparticle. The temperature outside the nanoparticle is given by the expression:

$$T(\mathbf{r}) = \frac{Q}{4\pi\kappa \left|\mathbf{r} - \mathbf{r_i}\right|} \tag{2.32}$$

Which contains the scalar Green's function:

$$G(\mathbf{r}, \mathbf{r_i}) = \frac{1}{4\pi\kappa \left|\mathbf{r} - \mathbf{r_i}\right|} \tag{2.33}$$

and $T(\mathbf{r}) = G(\mathbf{r}, \mathbf{r_i})Q$. Equation 2.33 describes the case in which NPs are placed in a linear, homogenous and isotropic medium (in experiments this will be liquid water), however if NPs are bound to glass, a correction factor must be used in order to account for the discontinuity in bulk material thermal properties. This configuration has been shown to be solvable through the use of the method of images commonly used in electrostatics. [72]. In this instance the expression becomes:

$$G(\mathbf{r}, \mathbf{r_i}) = \frac{1}{4\pi\kappa_1}\left[\frac{1}{R} + \left(\frac{\kappa_2 - \kappa_1}{\kappa_2 + \kappa_1}\right)\frac{1}{R'}\right] \tag{2.34}$$

When viewed through a fluorescence microscope, one can gain a radial profile of the fluorescence intensity, in this case R is the radial distance from the centre of the NP within the sample plane (see figure 2.4), and $R' = \sqrt{R^2 + r_d^2}$ where r_d is twice the distance between the NP and the glass surface. κ_1 and κ_2 are the thermal conductivities of the water and glass respectively.

The change in temperature around spherical NPs in homogeneous dielectric media due to photothermal heating can be expressed as the following in the limit $t \to \infty$

$$\Delta T(\mathbf{r}) = \frac{V_{NP} q}{4\pi\kappa r} \tag{2.35}$$

Where $\Delta T(\mathbf{r})$ is the local change in temperature , κ is the thermal conductivity of water and r is radial position from the NP centre. An equivalent expression for ΔT can be obtained:

$$\Delta T(r) = \frac{I C_{abs}}{4\pi\kappa r} \tag{2.36}$$

Where I is intensity, C_{abs} is the absorbtion cross section of the NP in water. This expression is used in reference [2], as the thermal conductivity κ is well defined, C_{abs} can be found for spherical NPs through Mie Theory and I of the excitation

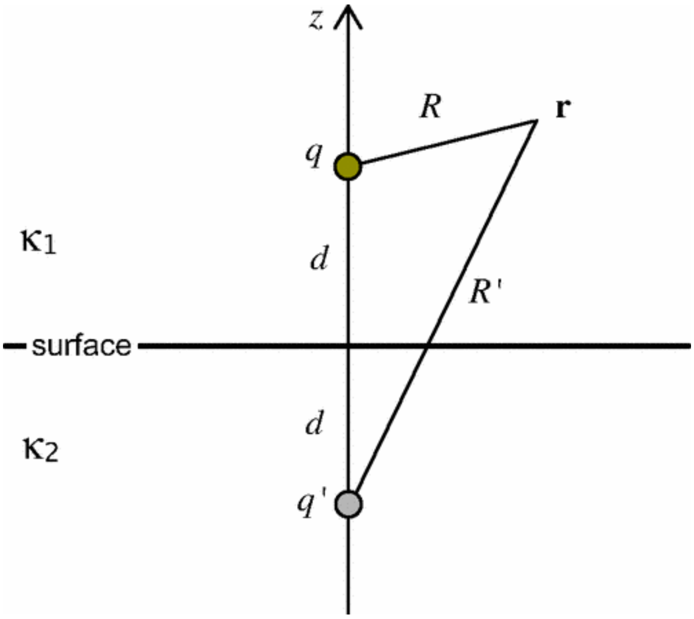

Figure 2.4: The temperature distribution originating from a heat source q facing a surface can be derived by the image method usually used in electrostatics. Reproduced with permission from [72].

laser is known. The full expression therefore becomes:

$$\Delta T = \frac{IC_{abs}}{4\pi\kappa_1}\left[\frac{1}{R} + \left(\frac{\kappa_2-\kappa_1}{\kappa_2+\kappa_1}\right)\frac{1}{R'}\right] \tag{2.37}$$

Chapter 3

Materials and Methods

3.1 Correlative extinction, epi-fluorescence and FWM samples

The following samples were imaged as part of a project carried out by a fellow member of the Biophotonics and Optoelectronics group Naya Giannakopoulou. Images of these samples are featured in Chapter 5, and are the focus of the correlative epi-fluorescence and FWM microscopy measurements.

3.1.1 10nmAuNP-SA(A488)-Bi-Tf(A647) in HeLa cells

This construct consists of commercially available AuNPs of 10nm diameter that have streptavidin, fluorescently labelled with Alexa488, adsorbed on their surface (Alexa Fluor 488 streptavidin, 10 nm colloidal gold conjugate 30μg protein/mL, Molecular Probes). HeLa cells were grown on 25 mm diameter circular coverslips of thickness #1.5 (Fisher Scientific). Cells were incubated for 30 minutes in serum-free medium, to allow recycling of serum-derived transferrin. They were then placed on ice for 15 min to inhibit endocytosis, incubated with 20 μg/mL Bi-Tf(A647) in ice-cold serum-free medium for 15 min and washed 3 times in ice-cold PBS pH 7.4. Cells were then incubated with the 10 nm diameter AuNP-SA(A488) at a particle concentration of 3.5×10^{11} AuNPs/mL (1 μg protein/mL) in ice-cold serum-free medium for 15 min, and washed 3 times in ice-cold PBS pH 7.4. They were then fixed in 4% PFA for 20 min at 4 °C, washed 3 times in PBS at room temperature, and mounted onto a microscope glass slide in Mowiol 4-88 (Sigma) mounting medium. This sample was prepared by Naya Giannakopoulou and Peter Watson.

3.1.2 15nmAuNP-PC-Tf(A488) in HeLa cells

This construct consists of AuNPs of 15 nm diameter covalently bound to a polymer shell onto which Tf fluorescently labelled with Alexa488 is covalently attached. This construct was developed in house as per methods described in detail in [81] (where it is called Tf-AuNP-3). It has an average of 3 Tf molecules per AuNP. The polymer is nonthermoresponsive, with the Tf exposed for cellular uptake. The hydrodynamic diameter of this construct was measured to be 49 ± 1 nm. The stock solution contained 1.27×10^{14} AuNP/mL. HeLa cells were grown on #2 thickness photoetched gridded coverslips, containing 520 alphanumeric coded squares of 0.6 mm×0.6 mm each (Electron Microscopy Sciences). Cells were incubated for 30 minutes in serum-free medium, to allow recycling of serum-derived transferrin. Cells were then incubated with the 15nmAuNP-PC-Tf(A488) at a concentration of 1.27×10^{13} AuNP/mL (1 in 10 dilution of the stock concentration) in serum-free medium for 2 hours. They were then washed 3 times in PBS pH 7.4, and incubated in pre-warmed imaging medium for 4 hours. At this point, they were fixed in 3% PFA for 10 mins at room temperature, washed 3 times in PBS at room temperature, and mounted onto a microscope glass slide in 80% DAKO mounting medium (Dako UK Ltd). This sample was prepared by Naya Giannakopoulou and Peter Watson.

3.1.3 40nmAuNP-SA-Bi-Tf(A647) in HeLa cells

This construct consists of commercially available AuNPs of 40 nm diameter, covalently bound to streptavidin (40nmAuNP-SA - InnovaCoat GOLD-Streptavidin 10OD, Innova Biosciences) which were subsequently bound to commercially-available biotinylated Tf (Sigma Aldrich) labelled in house with the fluorophore Alexa647 (Fisher Scientific). The generation of Bi-Tf(A647) was as per protocol described in [82]. Briefly, lyophilized biotinylated Tf (5 mg) suspended in 1 ml phosphate-buffered saline (PBS) pH 7.4, was added to 1 mg NHS-Alexa647 and reacted for 1 hour at room temperature to generate Bi-Tf(A647). The conjugate was purified from unreacted Alexa647 into PBS pH 7.4 using a G-50 sephadex gel filtration column (Life Technologies, Paisley, UK). To avoid aggregation and lack of functionality of the Tf, a sequential labelling method was utilised, were the 40nmAuNP-SA were added onto HeLa cells pre-loaded with Bi-Tf(A647) and maintained at 4 °C. To facilitate correlative experiments on different microscopes, HeLa cells were grown on #2 thickness photoetched gridded coverslips, containing 520 alphanumeric coded squares of 0.6 mm×0.6 mm each (Electron Microscopy Sciences). Cells were incubated for 30 minutes in serum-free medium (phenol red-free DMEM pH 7.4, containing 25 mmol/l HEPES, supplemented with 1 mg/ml BSA) to allow recycling of serum-derived transferrin. Cells were placed on ice for 10 min to inhibit endocytosis, incubated with 50 μg/mL Bi-Tf(A647) in ice-cold serum-free medium for 8 min and washed 3 times in ice-cold PBS pH 7.4. Cells were then incubated with the 40 nm diameter AuNP-SA at a concentration of $7\text{x}10^{10}$ AuNP/mL (1 in 10 dilution of the stock concentration) in ice-cold serum-free medium for 10 min then washed 3 times in PBS pH 7.4. Subsequently, cells were incubated in pre-warmed imaging medium to enable endocytosis for 6 hours. They were then fixed in 3% PFA for 10 mins at room temperature, washed 3 times in PBS at room temperature, and mounted onto a microscope glass slide in 80% DAKO mounting medium (Dako UK Ltd). This sample was prepared by Naya Giannakopoulou and Peter Watson.

3.2 Correlative epi-fluorescence and extinction samples

The following samples were imaged as part of the correlative epi-fluorescence and extinction microscopy measurements. Images of these samples are featured in Chapter 5.

3.2.1 20nmAuNP-PC-Ab(A647)

This construct was made from a commercially available kit (InnovaCoat GOLD 20OD Conjugation Kit, Innova Biosciences). It consists of 20nm diameter AuNPs with a proprietary protective surface polymer coat (PC) onto which proteins or antibodies can be covalently bound. Goat-antirabbit antibodies fluorescently labelled with Alexa647 (Thermo Fisher Scientic) were bound to these AuNPs following the manufacturer's protocol. InnovaCoat GOLD nanoparticles in the kit are freeze dried. The conjugation reaction is initiated simply by reconstituting the dry mixture with a reaction buffer and a diluted antibody stock (at 0.25mg/ml), which becomes attached (via lysine residues) to the InnovaCoat surface. We called this construct 20nmAuNP-PC-Ab(A647). In order to obtain a conjugate nominally 100% free from unbound antibody, we followed the manufacturer recommended wash protocol. Specifically, 20uL of stock solution was added to 1mL of deionised (DI) water (Sigma Aldrich). AuNPs were centrifuged at 9,000 g for 20 mins. 1mL of supernatant was removed. The protocol was performed once (1xwash sample), or repeated three times (3xwash sample).

3.2.2 10nmAuNP-SA(A488)

This construct consists of commercially available AuNPs of 10nm diameter that have streptavidin, fluorescently labelled with Alexa488, adsorbed on their surface (Alexa Fluor 488 streptavidin, 10 nm colloidal gold conjugate 30 g protein/mL, Molecular Probes). Also in this case, we followed the manufacturer recommended wash protocol. Specifically, 20uL of stock solution was added to 1mL of deionised (DI) water (Sigma Aldrich). AuNPs were centrifuged at 20,000 g for 30 mins. 1mL of supernatant was removed. The protocol was performed once (1xwash sample), or repeated three times (3xwash sample).

3.3 Samples used with qDIC

The following samples were used to exhibit the capabilities of the qDIC method:

3.3.1 Supported Lipid Bilayers

A supported lipid bilayer sample comprising the lipid 1,2-dioleoyl-sn-glycero-3-phosphoethanolamine (Avanti Polar Lipids) with the fluorophore label Atto488 and the lipid $DC_{15}PC$ in the following ratio $DC_{15}PC$:Atto488-DOPE(99.9:0.1) was provided by David Regan (a colleague in the Biophotonics group at Cardiff University) and was prepared using the following method: a lipid solution was formed by disolving the stock lipid in HPLC grade 2-propanol solvent (Sigma-Aldrich) with a concentration of 1.0 mg/mL. 150μL was deposited on the glass coverslip, and spin coated at 3600rpm, the coverslip was rotated about its centre axis. The coverslip was incubated for one hour in a humidified nitrogen environment at 37 °C. A SecureSeal imaging spacer (Grace Bio-Labs) was used to seal the sample and a phospate buffered saline (PBS) solution (Gibco) with a pH of 7.4 was added to its interior. The sample was then incubated in a water bath at 40-60 °C. Small air bubbles which are visible in DIC were removed by degassing the sample in a vacuum. Preparation of supported lipid bilayers was carried out by David Regan.

3.3.2 Polystyrene Beads sample

Coverslips were coated with several drops of Poly-L-Lysine and left for several hours. The coverslips were then stood upright to allow any excess polylysine to drain off, and left to dry for two hours. A SecureSeal imaging spacer (Grace Bio-Labs) was used to seal the 100nm Polystyrene Microspheres (Malvern Panalytical), (refractive index of $n = 1.58$) in DI water. The stock solution was diluted in water 1:1000. The coverslips were then sonicated for 10 minutes to reduce surface roughness which would result in a background in DIC. The Polystyrene beads sample was prepared by Timothea Konstinantinou and Iestyn Pope.

3.3.3 SU-8 2000 Permanent Epoxy Negative Photoresists

A sample which consisted of SU-8 2000 Permanent Epoxy Negative Photoresists (Micro Chem) with a measured refractive index of $n = 1.604 \pm 0.002$ at 550nm±10nm was prepared by Robin Islam [83]. The sample was manufactured by spin coating the polymer and subsequenctly irradiating the deposited polymer though a contact lithography mask which produced parallel stripes with an approximate width of 3μm and a spacing of 50μm. The sample was sealed in silicone oil (Sigma-Aldrich) which has a refractive index of $n = 1.516$.

3.3.4 Lipid bilayer with Gold nanoparticles

This sample was prepared in order to test the suitability of the qDIC method for the quantification of the surface heating of a AuNP. 50nm Gold nanoparticles (BBI Solutions) were sedimented onto a Caro's etched $24 \times 24\text{mm}^2$ coverslip. This process renders the surface of the coverslip hydrophilic which aids in the formation of lipid bilayers. $DC_{15}PC$:Atto425-DOPE (99.9:0.1) was then added to the coverslips in the same way as described in section 3.3.1.

3.4 Glass cleaning

A Caro's etch (also called Piranha etch) was performed to clean the glass used in experiments, as well as to render the surface hydrophilic. Coverslips and microscope slides were first wiped with optical lens paper (Whatman) soaked in acetone to remove any visible debris. The glass was then placed in a 3:1 volumetric ratio of Sulfuric Acid to Hydrogen Peroxide which was heated to 95°C for 30 minutes. $24 \times 24\text{mm}^2$ Menzel Gläser glass coverslips with thickness No.1.5 were used for all samples apart from the 10nmAuNP-SA(A488) sample which were deposited onto a fused silica coverslip (UQG) thickness 1.5.

3.4.1 Dropcasting nanoparticles

A coverslip was placed on optical lens paper (Whatman), 200μL was deposited onto the coverslip (200μL is enough to wet the entire surface of a Caro's etched $24 \times 24\text{mm}^2$ coverslip) and left to dry in air under the fume hood, whilst partially covered for 10 minutes. The coverslip was then recovered and washed with DI water.

3.4.2 Nanoparticle sedimentation (controlled NP density on piranha etched glass)

For the sedimentation method, 200μL of solution is deposited on a $24 \times 24\text{mm}^2$ coverslip, which is then covered with a glass lid, containing a piece of wetted tissue. This was done in order to saturate the enclosed atmosphere with humidity and thus to reduce the "coffee ring" aggregation effect observed under drop-cast and drying conditions.

3.4.3 Spin coating of Nanoparticles

20μL of AuNP solution was spin coated at a speed of 2000rpm for 35s, then at 4000rpm for 30s. The spin coater used was manufactured by Laurell Technologies.

3.4.4 Addition of immersion oil into imaging gasket via a Teflon tube

This protocol was developed in order to deliver silicone oil to an imaging gasket whilst the sample is mounted in the microscope, avoiding the need to dismount the sample during imaging. This was developed in order to carry out epi-fluorescence and extinction colocalisation studies, which required imaging fluorescently labelled

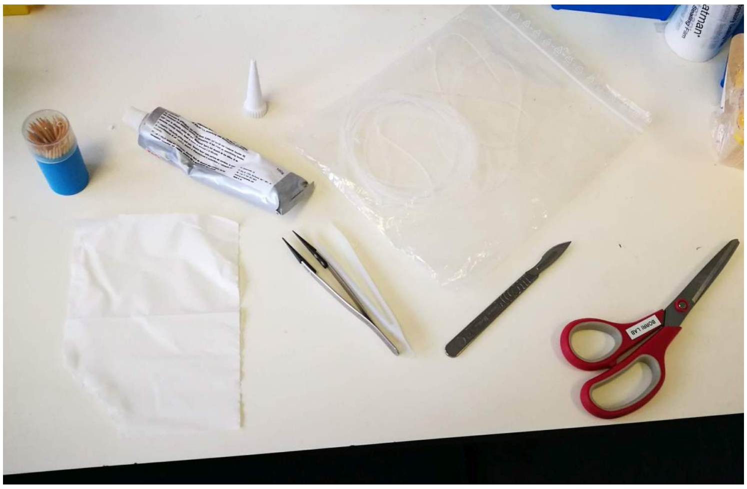

Figure 3.1: Equipment required for creating a fillable gasket, namely: Scalpel, Scissors, Tweezers, Teflon tubing, Cocktail sticks, optics paper, slicone glue

gold nanoparticles in air and then adding oil to the imaging gasket in order to suppress backgrounds from surface roughness in the extinction measurements by using an index matched immersion medium (Cargille RI matching liquids, series A,$n_D = 1.46$). The equiment used for this procedure were as follows: a Microscope slide, falcon tube, imaging gasket, coverslip, plastic syringe, teflon tubing silicone sealant, cocktail sticks, scissors, scalpel, tweezers and tissue paper (shown in figure 3.1). The following procedure was used to create fillable gasket samples:

The slide and coverslip were prepared for imaging using standard cleaning procedures i.e. piranha etching or Hydrogen Peroxide immersion. The imaging gasket was then cut in half before both halves of the imaging gasket were placed onto the coverslip, with the cut section running along the length of the slide. This section provided a chamber for the oil to be inserted and for air to be pushed out. After the coverslip was prepared, it was placed onto the imaging gasket. A small section of teflon tubing was then cut for addition to the imaging gasket (no longer than 10cm). At one end, the tubing was cut diagonally with the scalpel, from the centre of the opening of the end, this made the surface area of the teflon tube opening larger. A bead of silicone glue was added to the side of the coverslip, this was to ensure that there is a seal so that the oil that entered the gasket and did not come out of the side. With a cocktail stick, the glue was spread towards the coverslip, ensuring that there were no gaps in the silicone sealant.The tubing was placed (with a diagonally cut edge) at the edge of the coverslip above the chamber where the oil should flow through. The tubing was pushed through the glue at the side of the coverslip. After this, the sealant was left to dry for approximately 30 minutes. After making sure that the tubing was in the correct position at the edge of the coverslip, the tubing was glued around, care was taken to seal it properly - failure to do so would lead to leakage and also an incorrect calibration for filling the imaging gasket with oil. The slide and coverslip was then left to cure for 24 hours. When the slide was mounted,

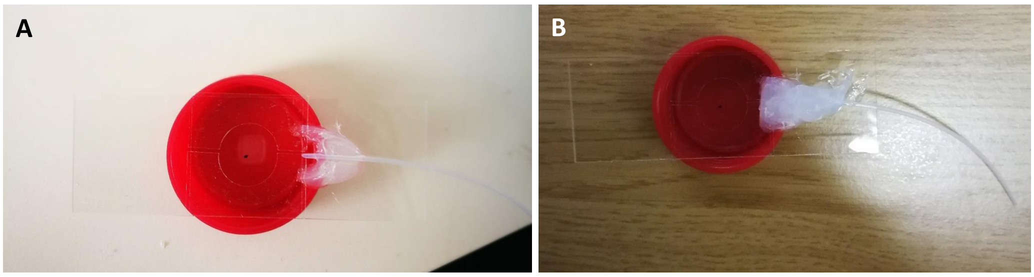

Figure 3.2: Arrangement for sample chamber to enable sequential addition of immersion media. **A**: Initial step in adding the teflon tubing to the side of the imaging gasket. Note that the shape of the added silicone glue is a crescent around the contact point between the teflon tubing and the opening at the edge of the gasket. **B**: Second step in gluing the teflon tubing to the imaging gasket. Once the crescent of glue is applied and the teflon tubing is placed, silicone glue is added in order to seal the area around edge of the teflon tube at the contact point. Care is taken to make sure that there are no holes in the glue, to prevent any leakage of oil.

(this protocol developed for use with the Galileo setup and use with the 60× objective) care was taken to make sure that the glued part of the sample did not interfere with the positioning of the objective - the sample was moved to a lateral point where the objective could be raised and lowered without contacting the glued part of the sample. The tip of the syringe was then inserted into the tubing before imaging. Images of the gluing process for the fillable gasket are shown in figure 3.2.

3.5 Experimental setups

DIC, Extinction and nanoparticle photothermal heating experiments were performed on two multi-modal experimental setups, both of which are built around a Nikon Ti-U inverted microscope. Optical elements used in DIC imaging were identical for both setups. Images were captured using the following objectives: 20× 0.75NA dry objective, 60× 1.27NA water immersion (Nikon lambda series) or a 100× 1.45NA oil immersion (Nikon lambda-S series). A 1.34NA oil condenser was used.

3.5.1 Cameras

The follwing cameras were used for DIC and fluorescence imaging. Different cameras were used as two separate microscope systems were used to acquire images. A PCO.edge 5.5 scientific-CMOS was used exclusively during the nanoparticle heating experiment, whilst a Hamamatsu Orca 285 was used in order to acquire images for the correlative extinction and fluorescence experiments. Both microscope systems are capable of imaging for qDIC.

3.5.1.1 PCO.edge 5.5 scientific-CMOS

This camera has a sensor size of 2560×2160 pixels and can operate at 100 frames per second (full sensor). It is water-cooled with a pixel size of 6.5μm, full well capacity of 30ke and a read noise of 1.1e.

3.5.1.2 Hamamatsu Orca 285

This CCD camera has a sensor size of 1344 × 1024 pixels, a pixel size of 6.45μm, 18ke full well capacity 7e read noise. It has a 12-bit A/D converter with a conversion of 4.45 photoelectrons/counts.

3.5.2 qDIC

DIC imaging was performed with a 20× 0.75 NA objective and a 1.5× tube lens (unless otherwise stated). A halogen Tungsten lamp was used to illuminate the sample (V2-A LL 100W, Nikon). A GIF filter with transmission band 550±20 nm was used to define the wavelength range for qDIC analysis. A BG-40 filter (Schott) was also used in order to block near infrared light as the polarisers in the set-up do not provide sufficient extinction at these wavelengths. For phase adjustment a De Sénarmont compensator was used, this comprised a $\lambda/4$ waveplate, and a rotatable linear polariser. For DIC a Wollaston prism was placed above the condenser; below the objective a Nomarski prism was inserted followed by an analyser (fixed linear polariser), (see figure 2.1) was placed below. Nikon N2 prisms with a shear distance of 238±10nm were used. [57]

3.5.3 Extinction and Epi-Fluorescence

Extinction microscopy was performed as follows: 250 bright field images with an exposure time of 100ms were taken at one position, the sample was then shifted laterally by approximately 2 μm and a further 500 images were acquired, then the sample was shifted back to its previous position and 250 images were acquired. A Prior ProScanIII microscope automation controller was used to shift the sample during extinction measurements. 250 dark background images (i.e. with light blocked) were taken. Using the average over the acquired images, the extinction image (i.e. a differential transmission image) was calculated as described in Chapter 2. Data analysis was performed using an in-house developed sofware by Dr Lukas Payne, called "Extinction Suite". [39][40][41] A 60× 1.27NA water immersion (Nikon lambda series) with a 1.5× tube lens magification or a 100× 1.45NA oil immersion (Nikon lambda-S series) objective and a 1.34NA oil condenser were used to acquire the images. A green GIF filter (transmission band 550 ±20 nm; Nikon) was used to define the wavelength range. The NA of the condenser was set to be equal to that of the objective in use, apart from when measuring samples sealed in air, where the NA was set to 1 to avoid total internal reflection.

Epi-fluorescence microscopy was performed with a metal-halide lamp (Prior Lumen 200) and the exciter/emitter/dichroic filter cubes used were the GFP-A-Basic-NTE GFP-A-Basic-NTE (Semrock, 469/35, Di500, 525/39) and the Cy5-A-Basic-NTE (Semrock, 630/38; Di655; 694/44). Time courses of 36 images with an exposure time of 10s were acquired. Over this duration, photo bleaching was observed in for both A-488 and A-647 labelled nanoparticles.

3.5.4 Nanoparticle heating setup and alignment

A sketch of the set-up is shown in figure 3.3. The alignment procedure was as follows. The laser source was a continuous wave 532nm GEM Laser (Laser Quantum), which was coupled to the back port of a commercial Ti-U inverted microscope. The laser beam was steered by first manually adjusting the rear port mirror M4 to centre the beam in the far field of the 20× 0.75NA objective. The field iris PH is conjugated to the sample plane and its size can be adjusted manually. The beam expander BE is used to change the size of the laser beam at PH, to adjust the maximum size and corresponding intensity at the sample. The filter cube used for 532nm laser excitation and 400-515nm and 550-800nm emission in this experiment comprised of a dichroic mirror ZT532dcrb (Chroma) and a 532 laser notch filter ZET532NF (Chroma).

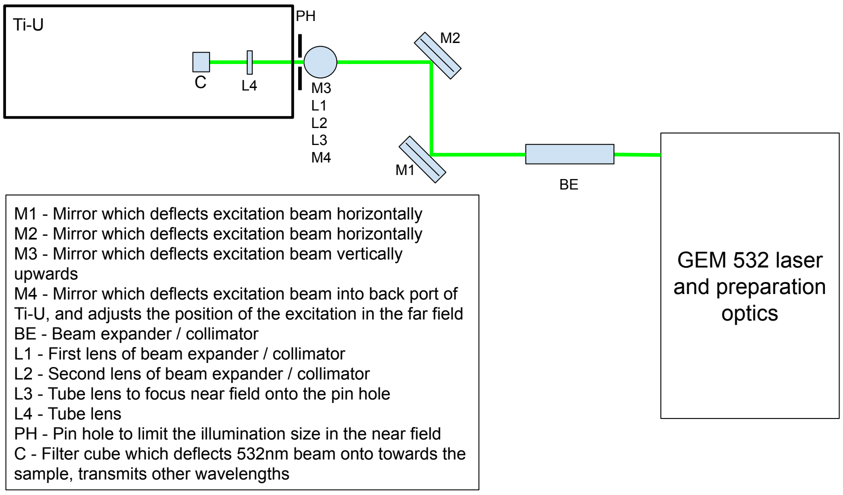

M1 - Mirror which deflects excitation beam horizontally
M2 - Mirror which deflects excitation beam horizontally
M3 - Mirror which deflects excitation beam vertically upwards
M4 - Mirror which deflects excitation beam into back port of Ti-U, and adjusts the position of the excitation in the far field
BE - Beam expander / collimator
L1 - First lens of beam expander / collimator
L2 - Second lens of beam expander / collimator
L3 - Tube lens to focus near field onto the pin hole
L4 - Tube lens
PH - Pin hole to limit the illumination size in the near field
C - Filter cube which deflects 532nm beam onto towards the sample, transmits other wavelengths

Figure 3.3: Optical path of the nanoparticle heating setup.

Chapter 4

Quantitative DIC: Results and discussion

This Chapter describes the workflow for acquiring DIC images, and the data analysis steps needed to obtain quantitatively the optical phase (and in turn the optical path length) from specimens. In order to extract quantitative information from a DIC image of a specimen, the following steps are taken (see also Chapter 2): The specimen is imaged with a positive phase offset (ψ_+), then with a negative phase offset (ψ_-), followed by the acquisition of a background image. In order to calibrate the polariser to give the desired phase offset, one must find the polariser angle (θ) position which corresponds to a maximum ($\theta = \pi/2$) and a minimum transmitted intensity ($\theta = 0$) through monitoring the intensity distribution from a histogram of counts viewed in live mode when imaging. The polariser position is related to the phase offset by $\psi = 2\theta$. By changing the polariser angle from zero the intensity increases as $I \propto 1 - \cos(\psi)$, with an additional intensity offset equal to the mean of the counts which are found at a phase offset angle $\psi = 0$ (assuming that there is no structure in the sample). Through finding the polariser angle which yields the maximum number of counts, one can find the mean number of counts which corresponds to a desired phase offset. Once these images are acquired (called I_+ and I_- in Chapter 2), one can use the in house developed qDIC software in order to extract the optical phase distribution over the specimen. Details of how an image of the optical phase is extracted from the acquired intensities I_+ and I_- can be seen in Chapter 2.1.

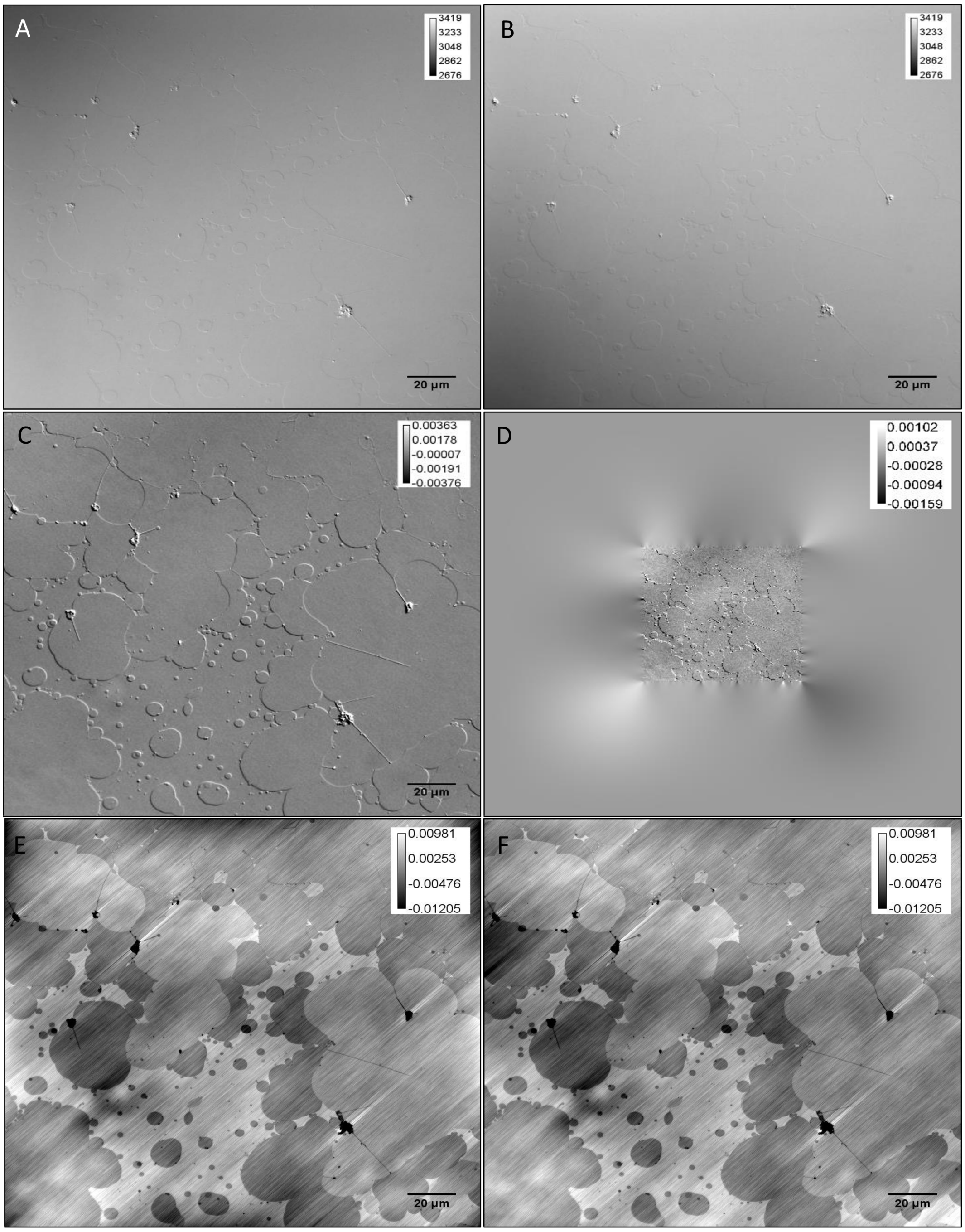
A
3419
3233
3048
2862
2676
20 µm
B
3419
3233
3048
2862
2676
20 µm
C
0.00363
0.00178
-0.00007
-0.00191
-0.00376
20 µm
D
0.00102
0.00037
-0.00028
-0.00094
-0.00159
E
0.00981
0.00253
-0.00476
-0.01205
20 µm
F
0.00981
0.00253
-0.00476
-0.01205
20 µm

Figure 4.1: Extracting absolute phase from supported lipid bilayers. **A** Negative phase offset image (I_-), **B** Positive phase offset image (I_+) **C** Differential phase (δ) image **D** Apodized version of image **C**, **E** Phase image derived from a contrast image that has not been apodized (signal to noise parameter $\kappa = 4000$). **F** Phase image derived from an apodized contrast image ($\kappa = 4000$).

Figure 4.1 (**A** and **B**) shows DIC images (with positive and negative phase offsets of 12.9°) of a supported lipid bilayer sample made of $DC_{15}PC$. DIC images of the lipid bilayer were acquired with the use of a 20× objective, and an acquisition time of 100ms with no averaging. This sample was chosen as it consists of stacks of lipid bilayers of different thicknesses which have clearly defined steps that are visible in

DIC. Images **A** and **B** are then used to yield a δ image (shown in figure 4.1(**C**)) which is the differential phase image (see section 2.1). The result of integrating the δ image through using the Fast Fourier Transform (FFT) algorithm to extract the optical phase image φ is shown in figure 4.1 (**E**). Aliasing artefacts occur at the edge of the retrieved phase (φ) images. These artefacts can encroach upon objects of interest. In order to reduce the effects of aliasing in the retrieved φ images, an apodization routine (discussed in section 4.2) was developed to reduce the edge artefacts seen in figure 4.1 (**E**). The result of the apodization routine can be seen in figure 4.1 (**F**), which has been retrieved from the apodized δ image in figure 4.1 (**D**).

A difference image between a non-apodized and apodized image of the supported lipid bilayer sample is shown in figure 4.2, which shows the extent of edge artefacts which occur if the apodization routine is not used.

0.00630
0.00269
-0.00091
-0.00452
-0.00812

Figure 4.2: Difference image between non-apodized and apodized phase (φ) images of supported lipid bilayers. The phase images shown in figure 4.1 **E** and **F** were used to create this difference image (the apodized phase image was subtracted from the non-apodized phase image).

When using Wiener deconvolution (see Chapter 2.1), to integrate differential phase images, line artefacts are generated along the shear direction. Increasing the signal to noise parameter κ produces more prominent line artefacts. Such line artefacts are visble in each phase image presented here (for example in figure 4.1 (**F**)). Figure 4.3 shows the process by which line plots are extracted from phase images. The image in **A** shows a differential phase (δ) image of the waveguide, **B** shows a phase (φ) image and a line plot which is parallel to the shear direction, as this is the direction in which the DIC images and consequently the contrast image

I_c are directly proportional to differential phase distribution over the sample. In this example the thickness of an optical waveguide made from a SU-8 photoresist was imaged using the method outlined above. Using low signal to noise parameter (κ) values gives phase profiles that deviate somewhat from the expected phase profile. In the case of the SU-8 waveguide stripe its edge should resemble a step function, with the exception that the width of the step is determined by the resolution limit of the 20× 0.75NA objective used. Higher values for κ give line profiles that are more step-like. The SU-8 waveguide was imaged with an acquisition time of 50ms with 256 averaging, at a polariser angle of 45°.

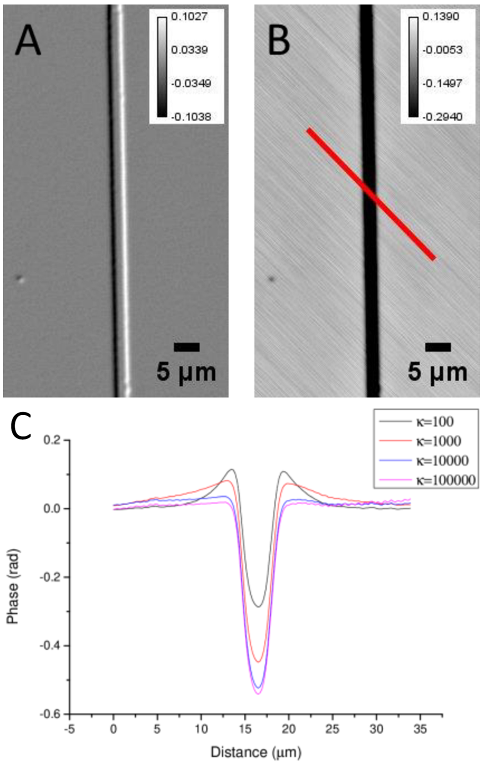

Figure 4.3: Extracting absolute phase from an SU-8 waveguide. **A**: differential phase image (δ) of a waveguide stripe fabricated with SU-8 photoresist, **B**: integrated phase image (φ) of the sample using a signal to noise parameter κ=10,000. **C**: line plots taken from **B** with increasing κ as given.

Generally, the lowest value of the κ parameter which maintains a step-like profile is used when producing phase images, as increasing this parameter causes line artefacts which encroach on nearby objects along the shear direction.

4.1 Polynomial Background correction

A second order polynomial background correction can be made to the contrast image before scaling to create a δ image. This removes an overall quadratic saddle-point-like background observed in the contrast image, which is thought to arise from a small mismatch between the splitting planes of the DIC prisms and the back focal planes of the condenser / objective, resulting in a phase offset depending slightly on the image position (this phenomenon is known as Haidinger's brushes).[84] An example of a polynomial background subtracted δ and phase φ image of a lipid bilayer sample as compared with non-background subtracted δ and φ images is shown in figure 4.4.

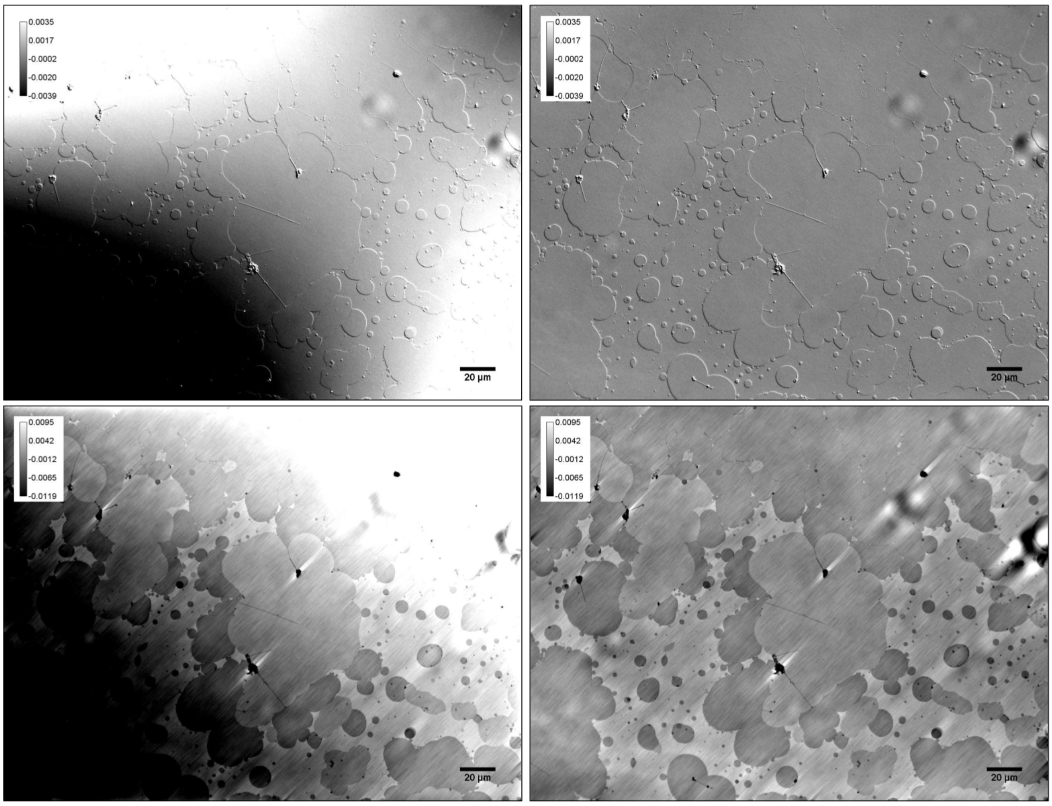

Figure 4.4: Polynomial background subtraction. Top left: differential phase (δ) image without polynomial background subtraction. Bottom left: Phase image (φ) corresponding to the δ image seen on the top left. Top right: differential phase with polynomial background subtraction. Bottom right: Phase image (φ) corresponding to the δ image seen on the top right.

4.2 Apodization

In the FFT algorithm the signal is assumed to be periodic, which is not the case for the structure measured. However, since the integration required is a spatially non-local operation, the result depends on the data across all space. Now, since data is only acquired over a finite size, one has to introduce assumptions for the boundary conditions, or the data outside the measured range. We present here an apodization which seeks to minimize the influence of the data outside the measured range. It extends the data and it removes the step at the periodic boundary in the FFT in value, first and second derivative, thereby suppressing high spatial frequency components introduced by the boundary.

In order to begin the smoothing process, the δ image is zero padded such that the total extended image size is 3× the size of the original DIC image. The corner values of the known δ image are then extended towards the edge of the zero padded region along the respective edge of the data (see figure 4.5).

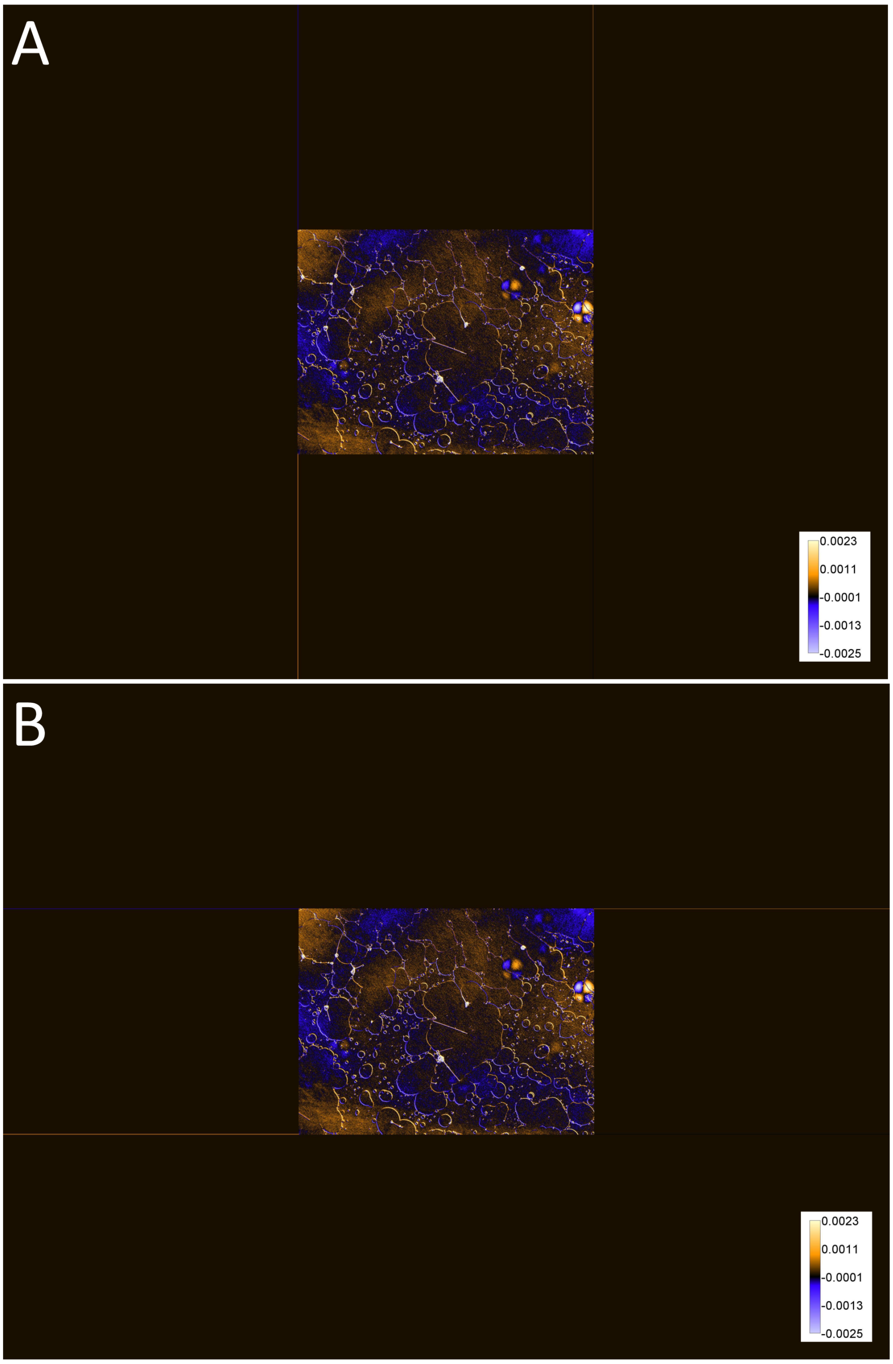

Figure 4.5: First step of the apodization process. Edge values are extended towards the edge of the zero padded image, which is 3× the size of the delta that is to be integrated. This is done separately horizontally and vertically (see **A** and **B** respectively).

Once the edge values are extended, the smoothing process occurs. The smoothing process for each individual line that is extended parallel to the selected edge of the data is as follows.

A Gaussian function with mean μ, and standard deviation σ, and unity integral, given by

$$y = f(x|\mu, \sigma) = \frac{1}{\sigma\sqrt{2\pi}} e^{\frac{-(x-\mu)^2}{2\sigma^2}}, \tag{4.1}$$

is convolved with the extended edge data extracted.

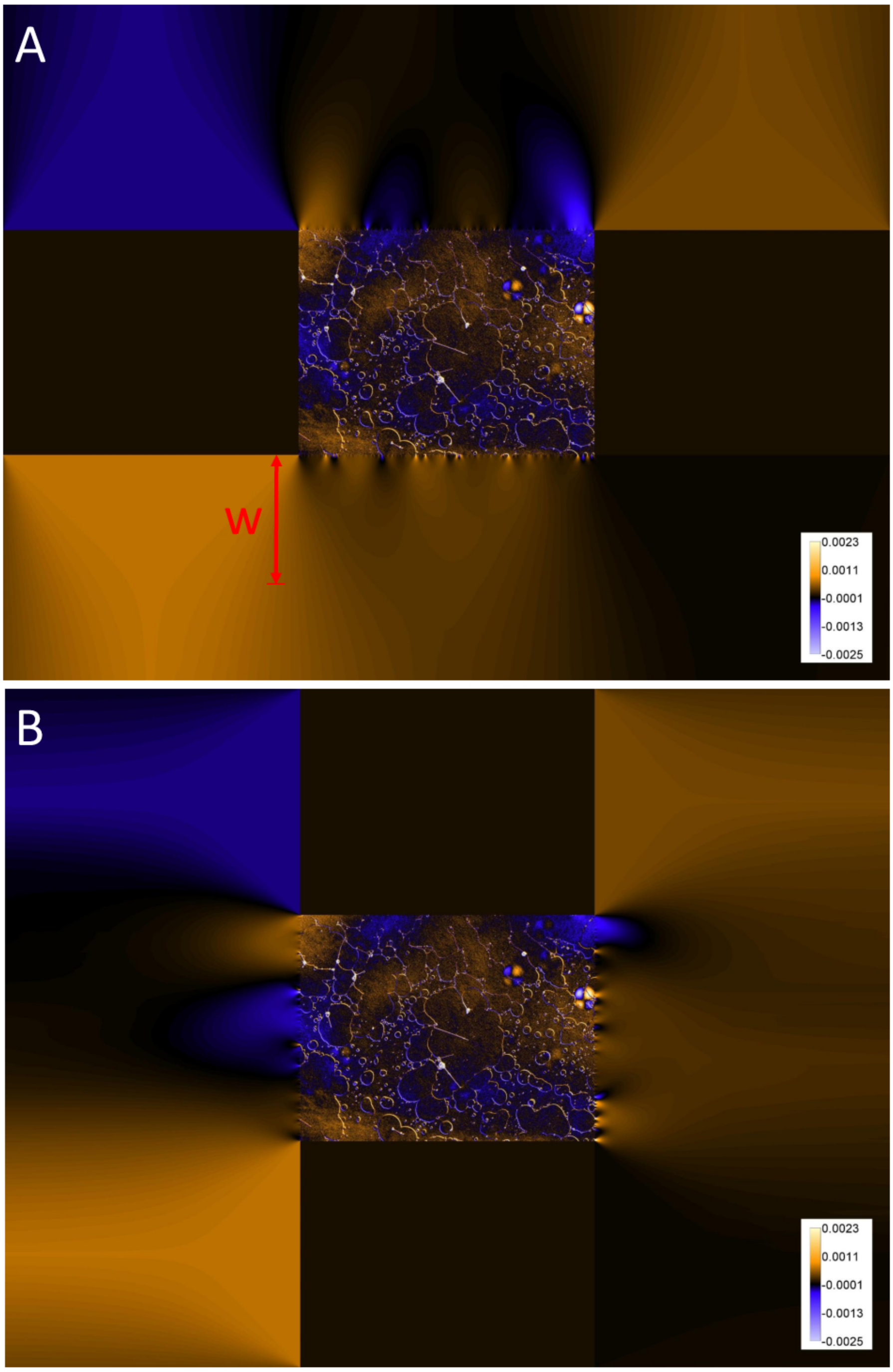

Figure 4.6: Result of the edge smoothing method for the extended image, for horizontal **A** and vertical **B** edges. The distance w from the edge for a selected line is indicated in **A**.

The full width half maximum (FWHM) of the gaussian ($\sigma\sqrt{8\ln 2}$) is chosen equal to the distance w from the extended data edge (see figure 4.6**A**)times a smooting rate s, so that $\sigma = ws/\sqrt{8\ln 2}$. The smoothing is thus increasing with distance, which is akin to a defocussing. Using this method the whole extended array is filled with smoothed values, and this procedure is performed separately for the horizontal and vertical directions as shown in figure 4.6 using $s = 1$.

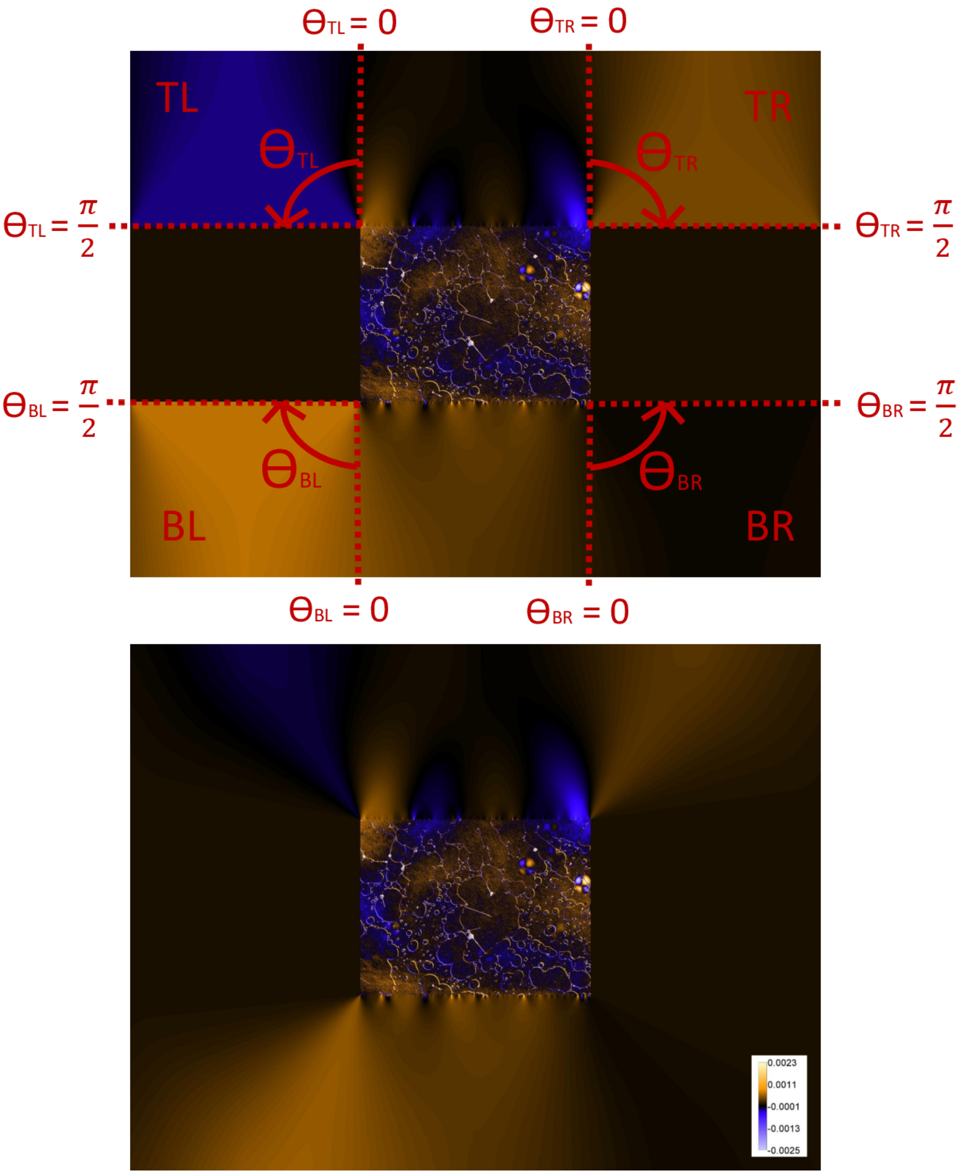
$\theta_{TL} = 0$
$\theta_{TR} = 0$
TL
TR
θ_{TL}
θ_{TR}
$\theta_{TL} = \frac{\pi}{2}$
$\theta_{TR} = \frac{\pi}{2}$
$\theta_{BL} = \frac{\pi}{2}$
$\theta_{BR} = \frac{\pi}{2}$
θ_{BL}
θ_{BR}
BL
BR
$\theta_{BL} = 0$
$\theta_{BR} = 0$
0.0023
0.0011
-0.0001
-0.0013
-0.0025

Figure 4.7: Corner array interpolation for the horizontal edge extension. Top: The corner arrays top left (TL), top right (TR), bottom left (BL) and bottom right (BR) are multiplied by a $\cos^2\theta$ function, where θ is defined as shown for each corner array, resulting in the image shown at the bottom.

To avoid discontinuities in the corners of the extended image, values are taken from the corners of the vertically and laterally smoothed images (see fig 4.6), and are blended by multiplying the corner arrays with a $\cos^2\theta$ or $\sin^2\theta$ which gives more weight to the values that are closer to the edges of the central smoothed arrays. The corner array interpolation process can be seen in figures 4.7 and 4.8. The corner arrays are blended by taking the average of the corner arrays from 4.7 and 4.8, while the side arrays are taken from the corresponding extended edge, the result of which is shown in figure 4.9 **A**.

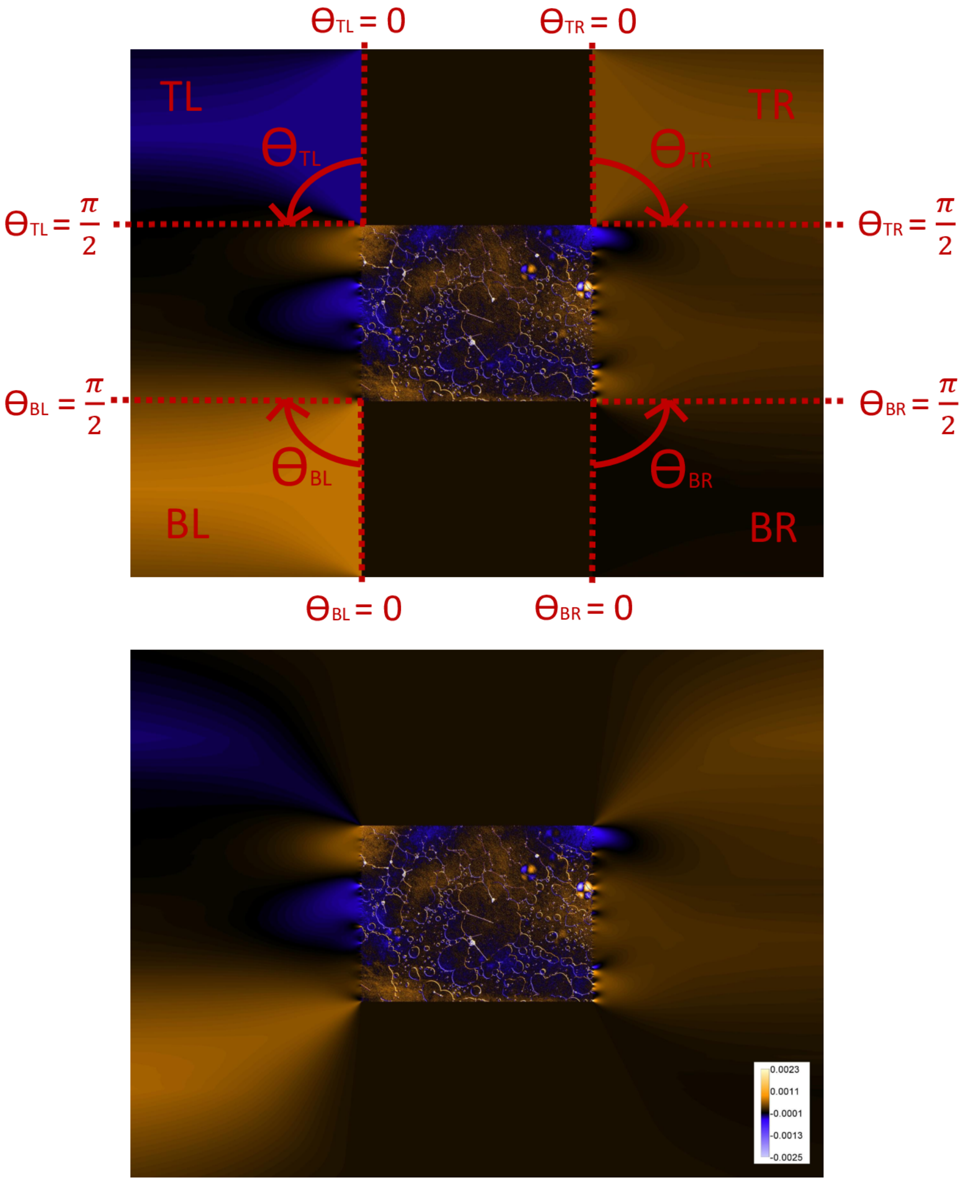
$\theta_{TL} = 0$
$\theta_{TR} = 0$
TL
TR
θ_{TL}
θ_{TR}
$\theta_{TL} = \frac{\pi}{2}$
$\theta_{TR} = \frac{\pi}{2}$
$\theta_{BL} = \frac{\pi}{2}$
$\theta_{BR} = \frac{\pi}{2}$
θ_{BL}
θ_{BR}
BL
BR
$\theta_{BL} = 0$
$\theta_{BR} = 0$
0.0023
0.0011
-0.0001
-0.0013
-0.0025

Figure 4.8: Corner array interpolation for the vertical edge extension. Above: The corner arrays top left (TL), top right (TR), bottom left (BL) and bottom right (BR) are multiplied by a $\sin^2 \theta$ function, where θ is defined as shown for each corner array, resulting in the image shown on the bottom.

A $\cos^2$ function is applied in both the horizontal and vertical directions of all extended areas to ensure that the edge values in the array are zero to minimise aliasing effects when using the Fast Fourier Transform. Using a $\cos^2$ function also ensures that the values in the extended area smoothly decrease towards zero at the edge of the image, removing boundary discontinuities in the zeroth, and first derivative. This is similar to the Hann window used in discrete fourier transforms to reduce spectral leakage. [85] The fully apodized extended image can be seen in figure 4.9**B**.

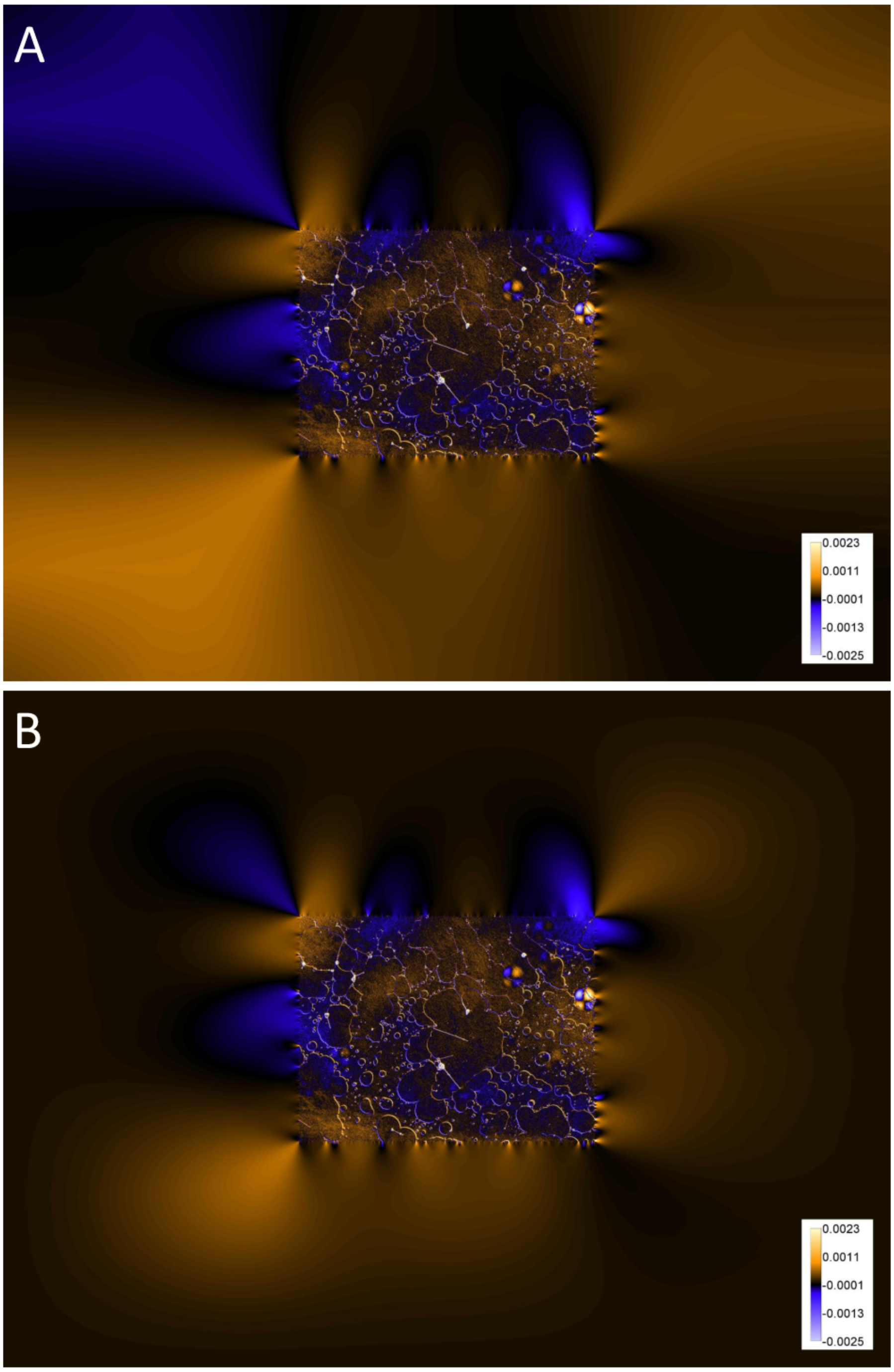

Figure 4.9: Apodized images.**A** shows the extended image with corner averaging. **B** shows the apodized version of the extended image.

The rate of smoothing can be controlled via the parameter s. Figure 4.10 shows the effect of varying the rate of smoothing. One can see that the effect of varying the smoothing rate on the integrated phase image is minimal (choosing s =0.5, 1 and 2), and it is only upon close inspection of the phase images that one can see differences at the edges of the phase images.

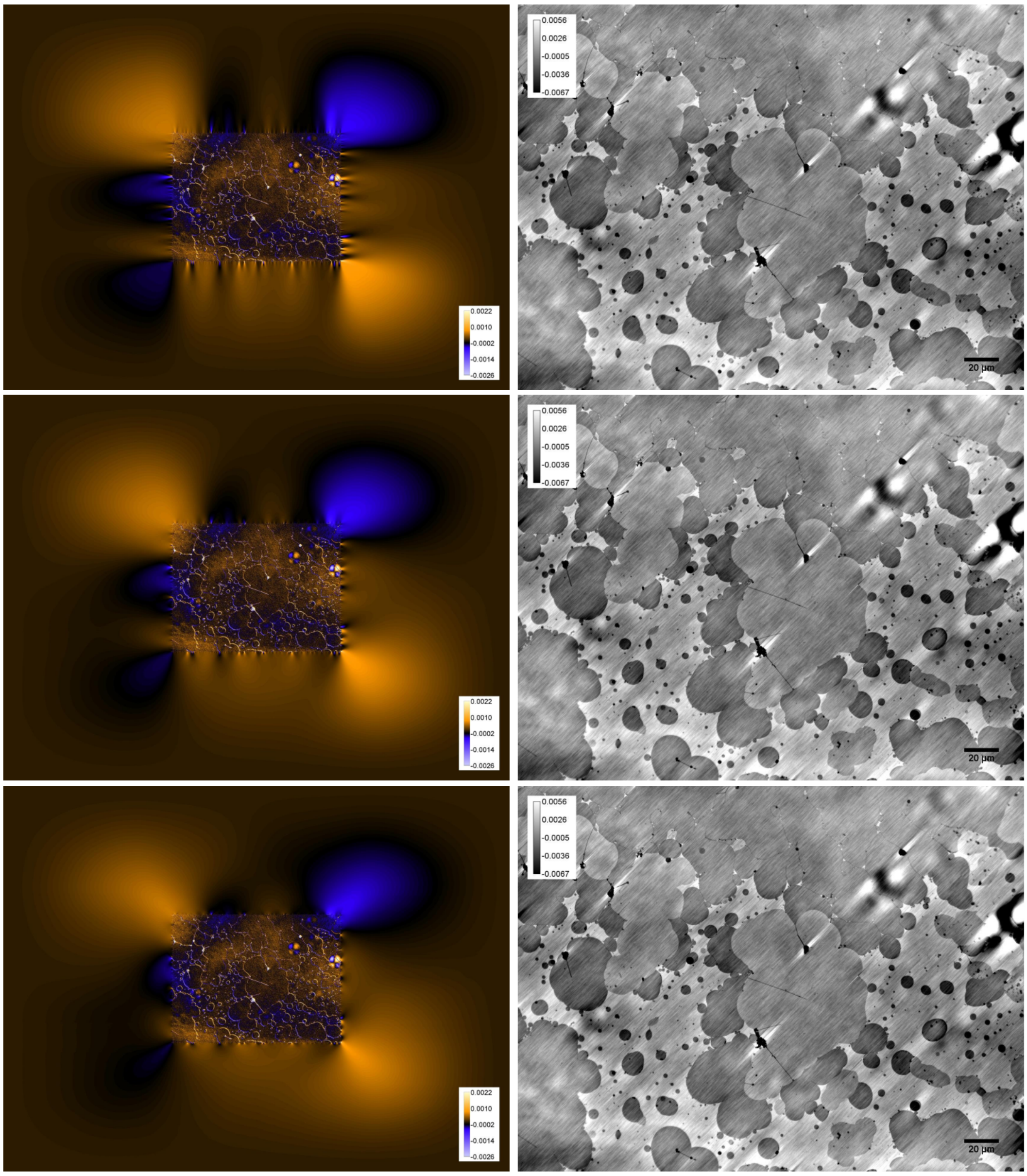

Figure 4.10: Results of the apodization for different smoothing rates. Left: Apodized image. Right: Resulting phase image after Wiener deconvolution with $\kappa = 1000$. Smoothing rates s used are 0.5 (top), 1(middle), 2 (bottom).

4.3 Region exclusion

To remove the integration artefacts that result from high contrast objects that are not of interest, a "region exclusion" feature has been developed, the result of this method in removing a high contrast object can be seen in figure 4.11.

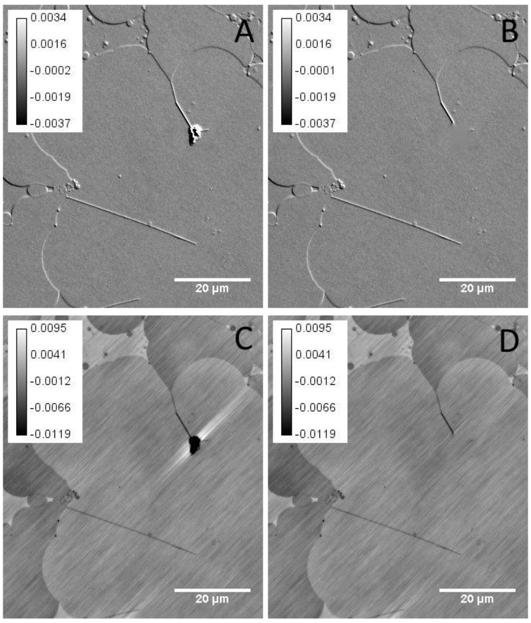
A
0.0034
0.0016
-0.0002
-0.0019
-0.0037
20 µm
B
0.0034
0.0016
-0.0001
-0.0019
-0.0037
20 µm
C
0.0095
0.0041
-0.0012
-0.0066
-0.0119
20 µm
D
0.0095
0.0041
-0.0012
-0.0066
-0.0119
20 µm

Figure 4.11: Example of the region exclusion method. **A**: differential phase (δ) image of lipid bilayer **B**: differential phase (δ) image with region excluded. **C**: Integrated image of lipid bilayer from **A** **D**: Integrated image from **B**. The region is replaced with smoothed values using a similar method to the apodization method.

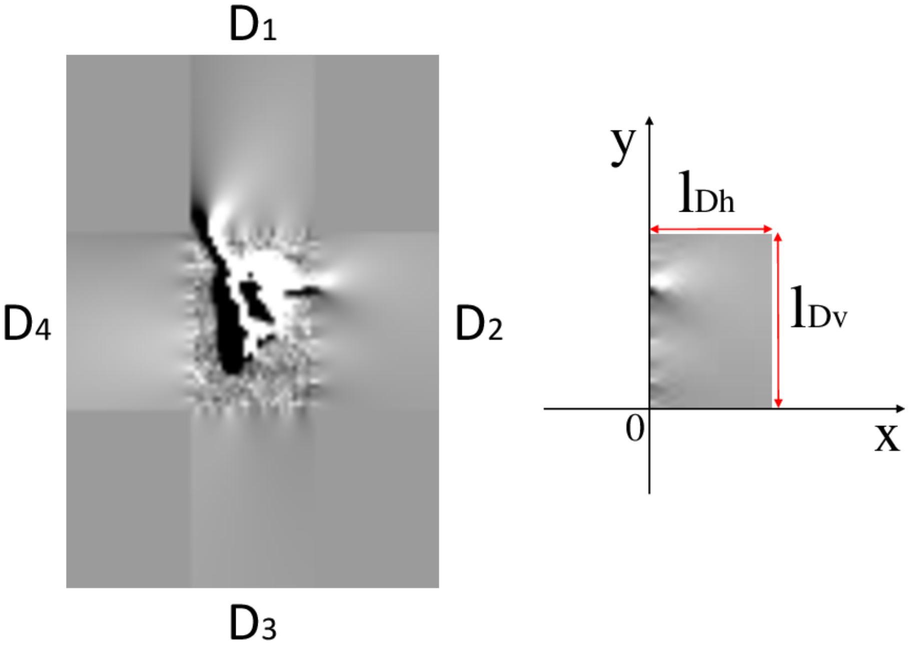
D1
D4
D2
D3
y
l_{Dh}
l_{Dv}
0
x

Figure 4.12: Excluded region and smoothed arrays D_1,D_2,D_3 and D_4. These smoothed arrays are used in order to create a array of values to replace the excluded region and reduce line artefacts upon integrating the differential phase image.

This method enables the user to filter out a rectangular area within an image and replace the object within the contrast image with a smoothed array which is created by using the following process:

The edge values of the region which is to be excluded are extended towards the

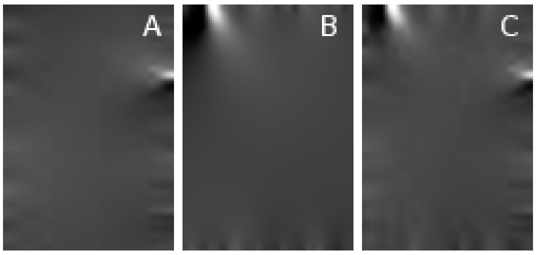

Figure 4.13: Merged arrays D_v (**A**) and D_h (**B**), as well as D (**C**).

edge of a zero padded array which extends the original image by 10× the size of the larger dimension. These edges are then smoothed as in the apodization discussed in section 4.2 to fill the extended array as seen in figure 4.12, in both the horizontal and vertical directions. An area the same size as the excluded region is then cut out on the edges which are adjacent to the excluded region as seen in figure 4.12, and flipped around the corresponding edge. These arrays are denoted as D_1, D_2, D_3 and D_4, and are merged according to equations 4.2 and 4.3:

$$D_h = \left(D_1 \cos^2\left(\frac{\pi y}{2l_v}\right) + D_3 \sin^2\left(\frac{\pi y}{2l_v}\right)\right), \tag{4.2}$$

$$D_v = \left(D_2 \cos^2\left(\frac{\pi x}{2l_h}\right) + D_4 \sin^2\left(\frac{\pi x}{2l_h}\right)\right), \tag{4.3}$$

where D_1 and D_3 are arrays which contain smoothed pixel values in the vertical direction, and D_2 and D_4 are arrays which contain values that are smoothed in the horizontal direction. Arrays D_h and D_v are then merged to give the region exclusion array D according to

$$D = \frac{D_h \sin^2\left(\frac{\pi x}{l_h}\right) + D_v \sin^2\left(\frac{\pi y}{l_v}\right)}{\sin^2\left(\frac{\pi x}{l_h}\right) + \sin^2\left(\frac{\pi y}{l_v}\right)} \tag{4.4}$$

where $l_v = l_{D_v} + 1$ and $l_h = l_{D_h} + 1$, (see figure 4.12 for dimensions of l_{D_v} and l_{D_h}). Figure 4.13 shows the smoothed values in each direction (i.e. D_h and D_v), these smoothed regions are merged by equation 4.4. The merged data D_h, D_v and D is shown in figure 4.13 (**A** and **B** and **C**) . This process is designed to preserve the values at the 4 smoothed edges, whilst blending the values to create a smooth internal region, which suppresses the striping artefacts along the shear direction around this excuded region.

4.4 Flip Method

A simple known way in which one can reduce the effects of aliasing by the FFT algorithm is by using an extended image created by flipping the image (both left-right and up-down) and tiling the images in such a way so that there are no steps of the value at the periodic boundaries (Volkov symmetrization [86]). An example of this method is shown in figure 4.14 Extending the δ image using the flip method produces a marked improvement compared with non-extended image (see figure 4.1(**E**)) and a comparison between the flip method and the apodization routine is shown in figure 4.15. Upon close inspection of the phase image produced using the flip method, one can see that the edge artefacts are more prominent than in the image produced when using the apodization routine. The flip method remains available within the in house developed qDIC software, as it is a faster process than the apodization method.

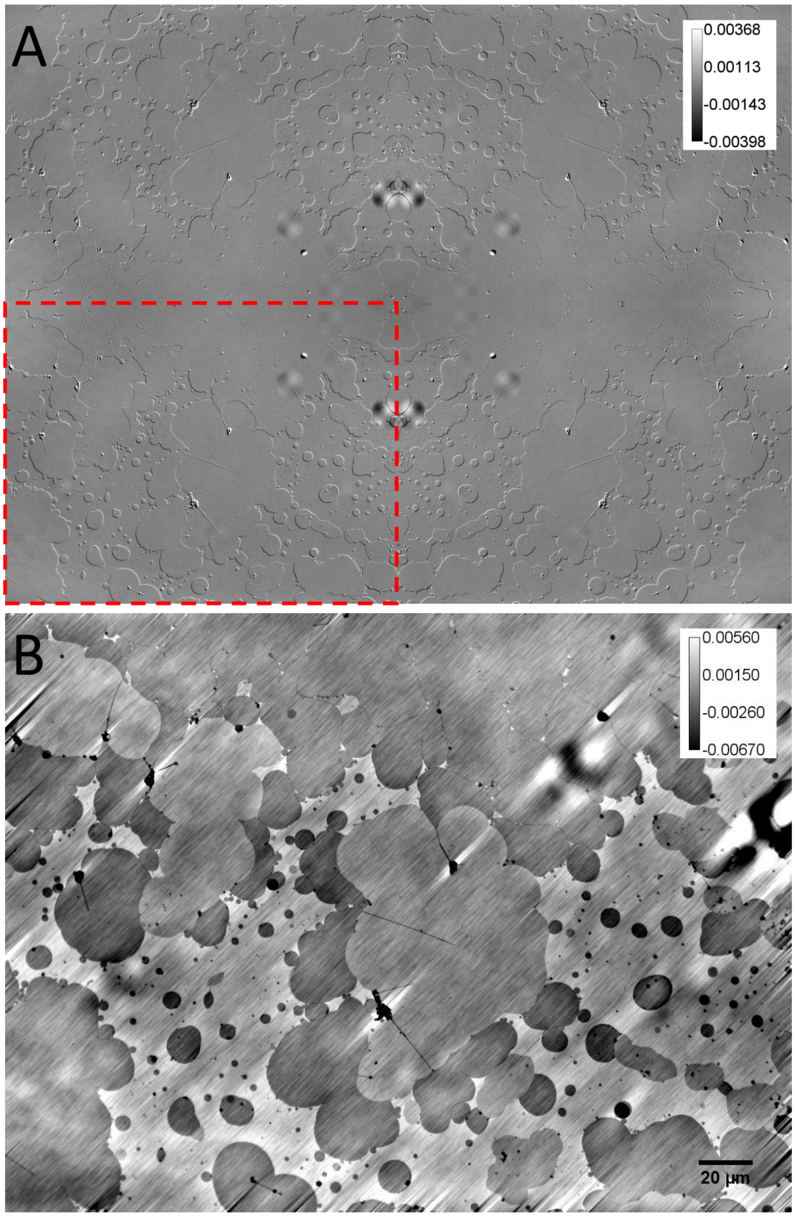

Figure 4.14: Extending the δ image using the flip method. **A** Extended differential phase (δ) image using the flip method, **B** Phase (φ) image produced when using the flip method on the portion of the extended image outlined by the dashed red outline.

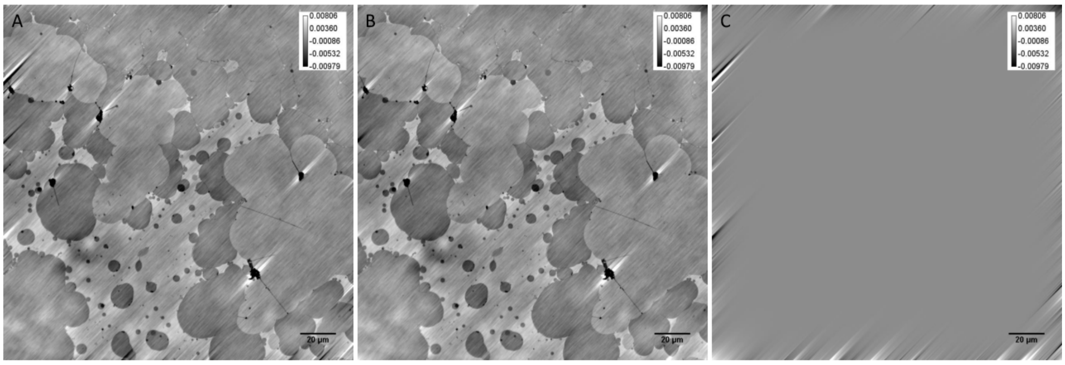

Figure 4.15: Comparison between phase images (φ) produced with the flip method and apodization. **A**: Phase image (φ) of lipid bilayers using the flip method **B**: Phase image (φ) using the apodization method **C**: Difference image between the apodized phase image and the integrated flipped phase image.

4.5 3D processing

To make a 3-dimensional map of specimens, an option in the qDIC software allows the user to integrate a stack of DIC images (both the positive and negative phase offset values are needed to create this stack).

4.6 Balancing

A balancing factor (α) is used to mitigate against phase offset errors which manifest in differences in pixel intensity value distributions of the positive phase offset and the negative phase offset images. It is defined as the root of the ratio of the average offset-corrected image intensities,

$$\sqrt{\frac{\langle I_+\rangle}{\langle I_-\rangle}} = \alpha \tag{4.5}$$

The α factor is then used to calculate corrected Intensities for the postive and negative phase offset images pixel-wise.

$$I_+{}' = (I_+)\alpha^{-1}; I'_- = (I_-)\alpha \tag{4.6}$$

4.7 In-band k-filter

The in-plane component of the k-vector of the light *field* collected by a microscope objective can be described as the following:

$$k_{||} = k_0 n \sin\theta \tag{4.7}$$

where θ is the angle relative to the image plane normal, n is the refractive index and $k_0 = 2\pi/\lambda$ is the wavevector in vacuum. By introducing the objective numerical aperture (NA) equation 4.7 for the maximum collected angle can be rewritten as

$$k_{||}^{\mathrm{NA}} = \frac{2\pi}{\lambda}\mathrm{NA} \tag{4.8}$$

The maximum k-vector k_{max} of the resulting image intensity occurs due to the interference of 2 fields at -$k_{||}^{\mathrm{NA}}$ and $+k_{||}^{\mathrm{NA}}$, resulting in $k_{max} = 2k_{||}{}^{\mathrm{NA}}$. In order to remove spatial frequencies in the intensity image above the pass band of the microscope objective, which do not correspond to the physical features of the specimen under scrutiny, a k-filter is used to remove spatial frequencies above the optical limit k_{max}. To remove spatial ringing which could be introduce by a sharp filter in k-space, the sharp edge of the filter is smoothed as follows. A cross section of the in-band k-filter is seen in figure 4.16 which illustrates the filter shape around k_{max}, which is constructed by replacing the edge with a $\cos^2$ function in the region ηk_{max}.

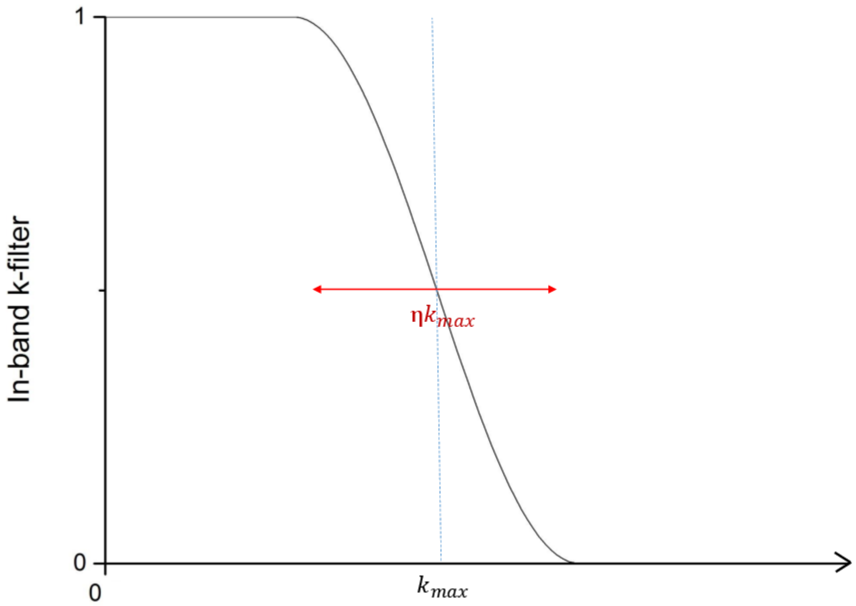

Figure 4.16: Profile of the in-band k-filter.

An example of the use of the k-filter is seen in figure 4.17, where a Wiener filtered phase (φ) image with and without performing in-band k-filtering on the differential phase image (δ) is shown. Line plots over a lipid bilayer edge are plotted for the filtered and non-filtered images, which shows the suppression of high frequency oscillations in the filtered image which is due to second minimum of the DIC transfer function. Suppressing high frequency oscillations is necessary when extracting optical phase images of phase transitions in lipid bilayers, where thickness changes are on the scale of 1nm,[87] and such oscillations can impact on the accuracy of lineplot measurements from optical phase images.

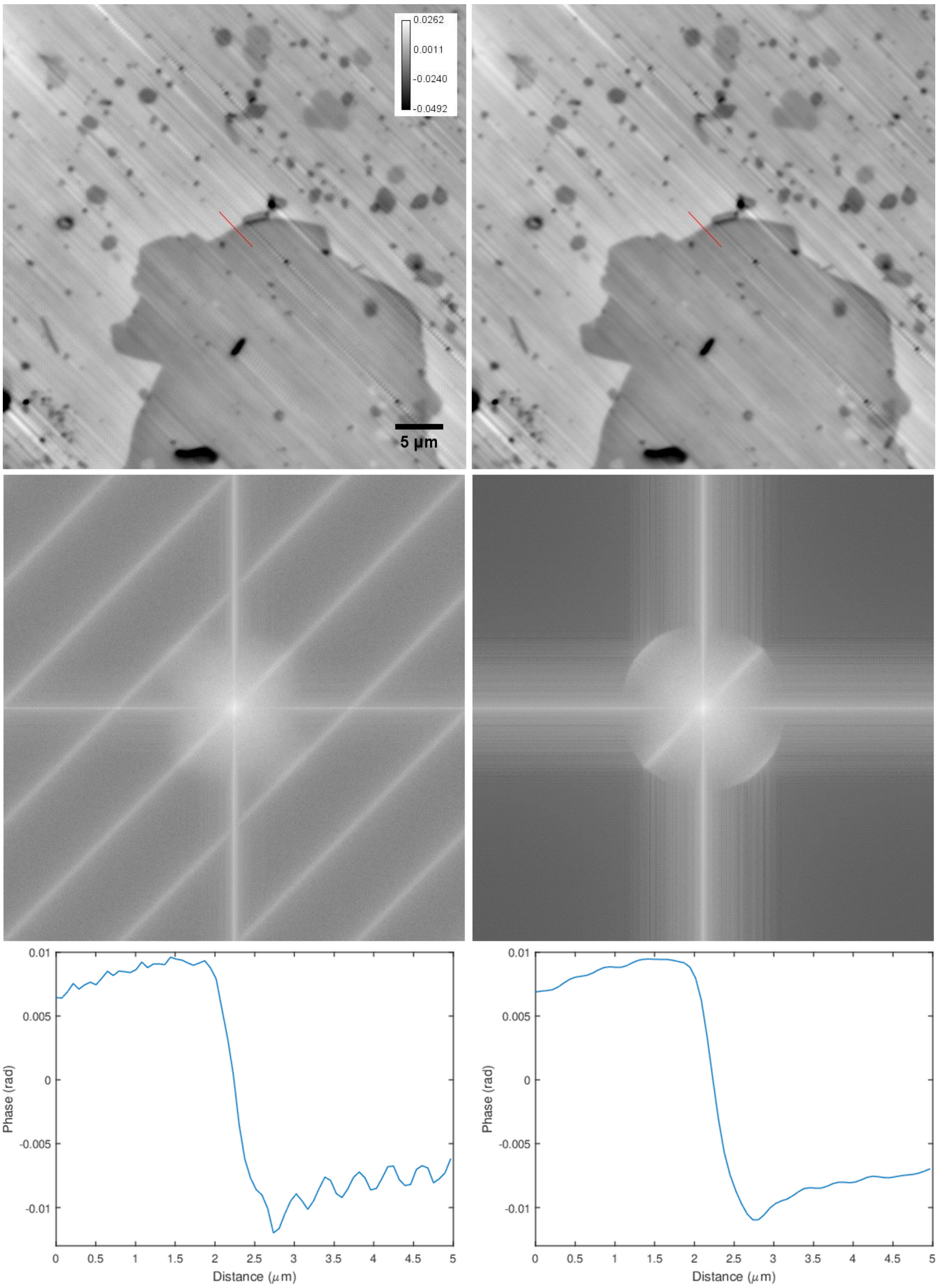

Figure 4.17: k-filtering for qDIC images of lipid bilayers acquired with a 100× objective with 1.5× multiplier. Top left: Wiener filtered phase image (φ) of an image integrated without in-band k-filtering, top right: Wiener filtered phase image (φ) of an image integrated with in-band k-filtering, middle left: FFT image (log_{10} of the absolute values from the FFT) of a Wiener filtered phase image integrated without in-band k-filtering with a minimum value of -6.601, and a maximum 3.342, middle right: FFT of a Wiener filtered phase image integrated with in-band k-filtering with a minimum value of -6.983, and a maximum 3.342, using a user defined NA of 0.85 and $\eta = 0.05$. Bottom left: line plot of taken from the red line in the unfiltered image seen top left, bottom right line plot of taken from the red line in the filtered image seen top right.

4.8 Time course functionality

In addition to the normal mode of operation for the qDIC software, one can use it for the measurement of dynamic samples such as unbound polystyrene beads which bind to the coverslip electrostatically. This is the case of the sample described in Chapter 3.3.2, consisting of a glass coverslip coated with Poly-L-Lysine, onto which polystyrene beads (of nominal 100nm diameter) attach and detach dynamically, while being in a water suspension. The point of difference between the normal mode of operation and the time course mode is the definition of the contrast image $I_c(\mathbf{r})$. For this modality, a time sequence of images is acquired using the same phase offset (+), called I_n, n=1,2,3..... Prior to the image time course, two opposite-angle phase offset images are acquired (I_+ and I_-), as per conventional qDIC acquisition described so far. The contrast is defined as follows:

$$I_{cn}(\mathbf{r}) = \frac{2(I_{n+2} - I_n)}{I_+ + I_-} \tag{4.9}$$

The aim of this new contrast definition is to remove static background, and highlight temporal differences, such as individual beads attaching and detaching onto a surface with large optical roughness. iSCAT is a comparable interferometric method which can be used to image transient behaviours within samples. The main source of difference between this method and iSCAT is that iSCAT is based on an interferometric reflectometry principle,[35] [36] hence it works in reflection, and relies on scattering objects, while DIC is a transmission technique suited for transparent dielectric structures. For this reason, iSCAT is more "background free" and is not limited by the shot-noise of the transmitted light, whereas DIC is. This DIC based method is simpler to set up however and only requires that the microscope being used is capable of imaging in DIC.

4.8.1 Example of time course (Polystyrene beads)

The δ image that derives from the 'normal' contrast image using the following equation (also seen in Chapter 2.1)

$$I_c(\mathbf{r}) = \frac{I_+ - I_-}{I_+ + I_-} \tag{4.10}$$

is shown in figure 4.18 for a sample of polystyrene (PS) beads suspended onto a Poly-L-Lysine coated coverslip, as described in Chapter 3.3.2. The Poly-L-Lysine layer is visible in this image as a source of surface roughness in the optical contrast. As a result, point-like contrast features of the type expected when retrieving the phase image of 100nm polystyrene beads can hardly be distinguished against this background. Most of the observed features are large-contrast debris or aggregates. Images of the PS bead sample were acquired using the 60× 1.27NA water objective, a polariser angle $\theta = 15°$ was used and time course images were acquired with an acquisition time of 1ms with 256 frame averaging. A GIF filter was used in transmission.

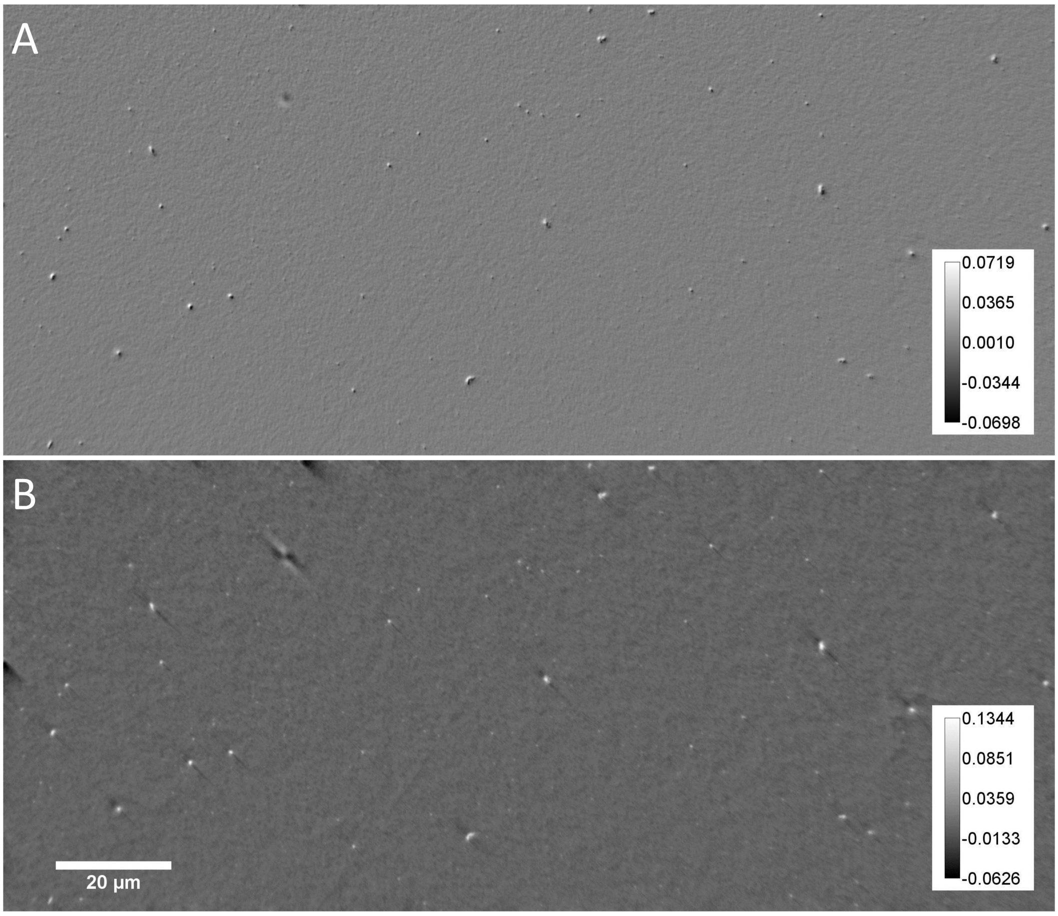

Figure 4.18: Differential phase (δ) and phase (φ) image of the 100nm PS beads sample. **A** is the differential phase (δ) image and **B** is the phase image (φ).

Using equation 4.9, the 100nm PS beads become visible in the differential phase (δ) and the phase image (φ). An example is shown in figure 4.19 for $n = 1$. Note the change in the gray scale range between 4.18 and 4.19, by nearly 2 orders of magnitude which exemplifies how this method enables to suppress the static contrast from the coverslip coated surface. To gain a quantitative measure of the volume of the PS beads the following relations were used. Firstly the integral of the phase φ around the bead area is calculated, called A. By taking into account that the optical phase introduced by a bead is $\varphi(\mathbf{r}) = 2\pi\Delta n t(\mathbf{r})/\lambda_0$, where λ_0 is the wavelength in vacuum, Δn is the refractive index change between polystyrene and water, and $t(\mathbf{r})$ is the thickness profile of the bead, A is simply proportional to the bead volume V via $A = 2\pi\Delta n V/\lambda_0$. An effective bead radius R can then be deduced by assuming $V = (4/3)\pi R^3$.

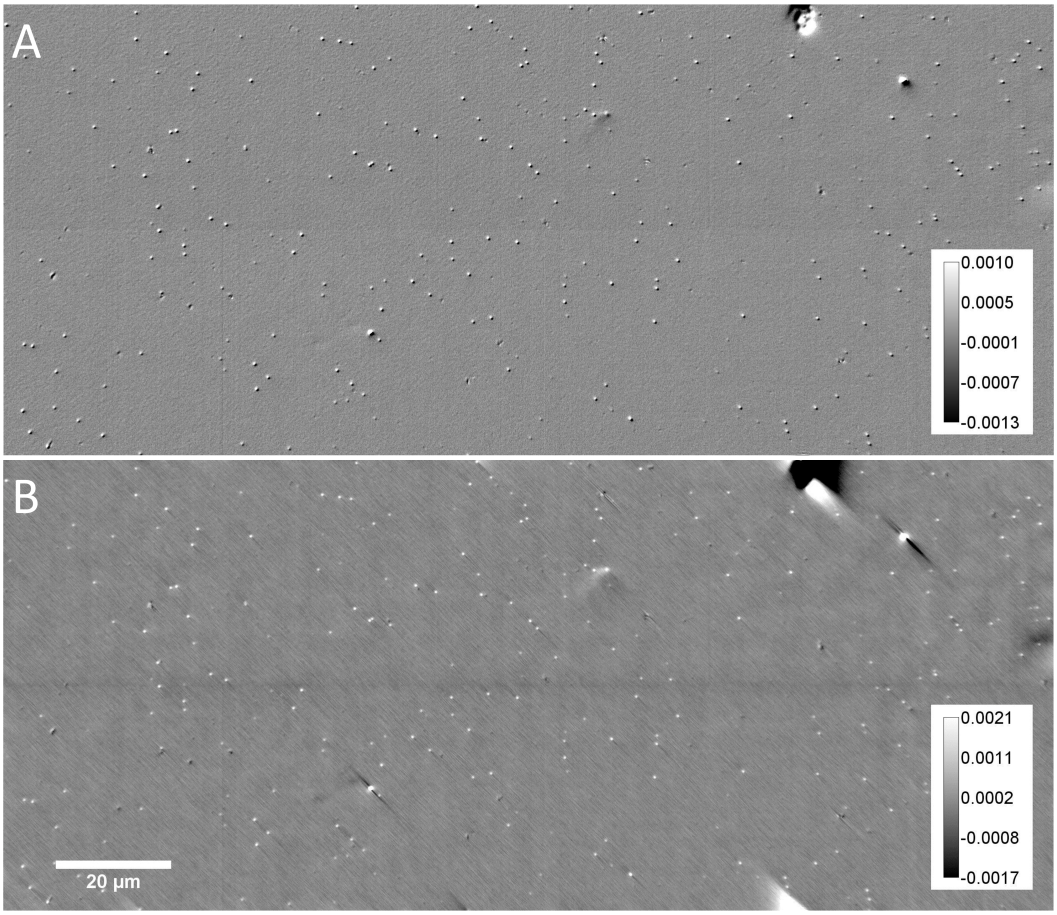

Figure 4.19: Time course differential phase (δ) and phase (φ) image of the 100nm PS beads sample. **A** is the differential phase (δ) image and **B** is the phase image (φ). using equation 4.7 with n=1.

The results from the analysis of figure 4.19 are shown in figure 4.20. The extracted diameter is surprisingly smaller than is expected (nominally the polystyrene spheres are 100nm in diameter with a variance in the 10% range, from the manufacturer description.). We are currently investigating this discrepancy. One possible explanation could be that, once attached, polystyrene beads are buried into Poly-L-Lysene such that the refractive index change between the bead and its surrounding medium is smaller than the one we used, and in turn the calculated bead volume must be higher. Figure 4.20 shows the retrived diameters for a surrounding medium of water ($n = 1.33$) and a surrounding medium of poly-L-lysine ($n = 1.45$). A notable increase in the diameters of PS beads occurs when assuming the surrounding medium has a refractive index of $n = 1.45$, though the retrieved diameters measured remain lower than the nominal diameter of 100nm. A further test is planned by using well resolvable 200nm diameter polystyrene beads on a clean glass surface, in order to test the accuracy of this method.

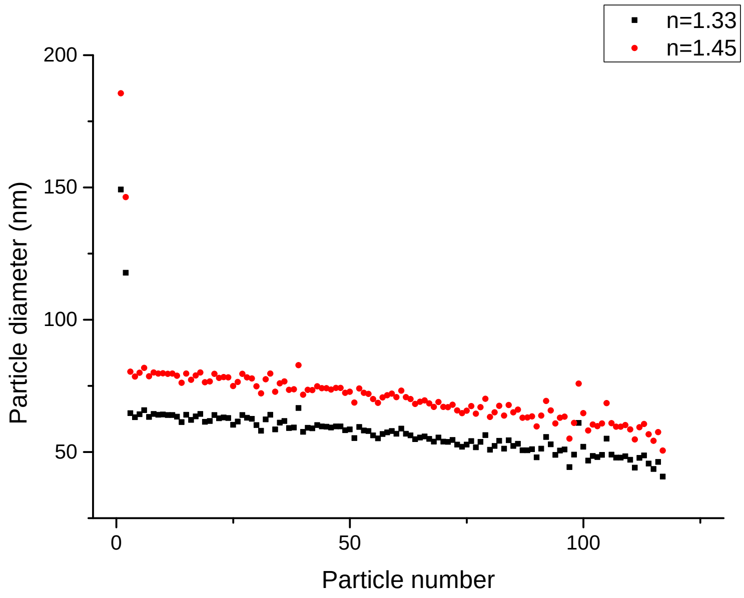

Figure 4.20: Retrieved polystyrene bead diameters from the contrast in figure 4.19, with refractive index for the surrounding medium n indicated. The particle number was dictated by the in-house software used (Extinction suite, developed by Dr Lukas Payne) to integrate the phase time-course phase images.

The attachment of PS beads generally occurred over approximately three frames as is shown in figure 4.21. The second frame within an attachment event gives the full contrast from the PS beads. To obtain a fully representative diameter for the PS beads, the frame with start time n which gives the full contrast for an attachment event should be measured for a given particle.

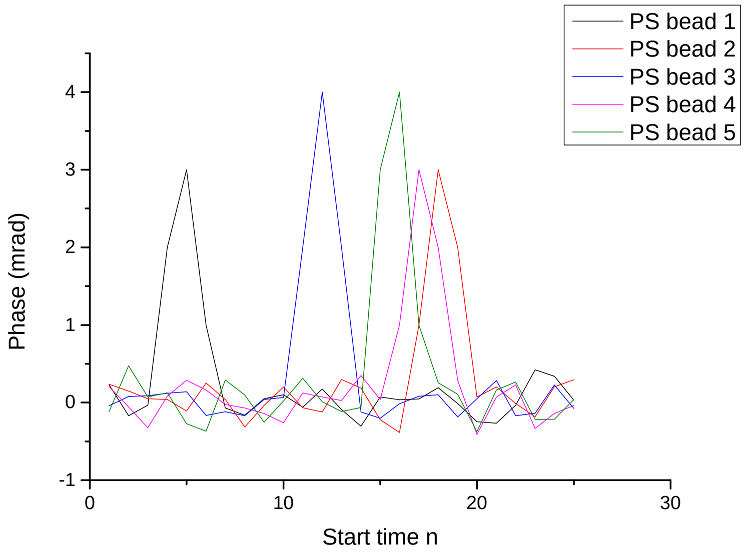

Figure 4.21: Phase measured at the peak pixel value of signal corresponding to PS beads.

4.9 Energy Minimisation

Whilst the Wiener deconvolution method (described in section 2.1.1) provides a fast and efficient method for extracting quantitative data from DIC images, phase objects of interest which are close to high contrast areas may be affected by artefacts which are a result of the Wiener filtering integration process. In order to reduce the effect of these artefacts, we have developed a modified version of an Energy minimisation framework proposed by Koos et al. [66] This energy equation is minimised by a gradient descent method which uses an error E given by two terms. The first term is the deviation between the measured and retrieved phase gradient, implementing the qDIC condition. The second is an additional term which is penalizing phase gradients in general, leading to a smoothing of the phase. This second term was generalized from [66] by including different powers of the gradient, and by also optionally penalising only gradients orthogonal to the shear, which are not constrained by the DIC measurement.

In our software, the Wiener filtered image is used as an initial phase guess which reduces the necessary number of iterations required for convergence to a phase map of the imaged specimen as compared to starting from zero phase as done in [66]. This aspect of the software can also be used without the initial guess of the Wiener filtered image. The energy that is minimised is given by

$$E(\varphi) = (\mathbf{u} \cdot \nabla\varphi - \delta) + \lambda S(\nabla\varphi); S(\nabla\varphi) = \begin{cases} |\nabla\varphi|^{\alpha} \\ |\mathbf{u}^{\perp} \cdot \nabla\varphi|^{\alpha}, \end{cases} \tag{4.11}$$

using an iterative process according to

$$\varphi_{i+1} = \varphi_i - \eta \frac{\partial E(\varphi_i)}{\partial \varphi_i}, \tag{4.12}$$

where $\mathbf{u}$ is the shear vector, i numbers the iterations. η is the integration factor, which is chosen to be as large as possible without causing instability, typically of the order of 1. λ is the smoothing factor, which controls the importance of the image smoothness relative to matching the measured differential phase δ. To test the energy minimisation routine, a synthetic bilayer-like image (shown in figure 4.22) which contains discrete steps, was created as follows. A reproducible noise image was created with a gaussian distributed noise and no spatial correlation in MATLAB, using the RandStream function. The image was then apodized with a $\cos^2$ function so that the edge values of the image were zero and the maximum values were found in the centre of the image. This image was then convolved with a 2D Gaussian kernel of size 33 pixels. After this step, the image was discretized using the imquantize function. A smooth object image (shown in figure 4.23) was created using the same process as the synthetic bilayer-like image, omitting the discretisation. DIC images were created using the imfilter function on the synthetic bilayer-like and the smooth object images, in the same way they are created in equation 4.11, $\mathbf{u} \cdot \nabla\varphi$.

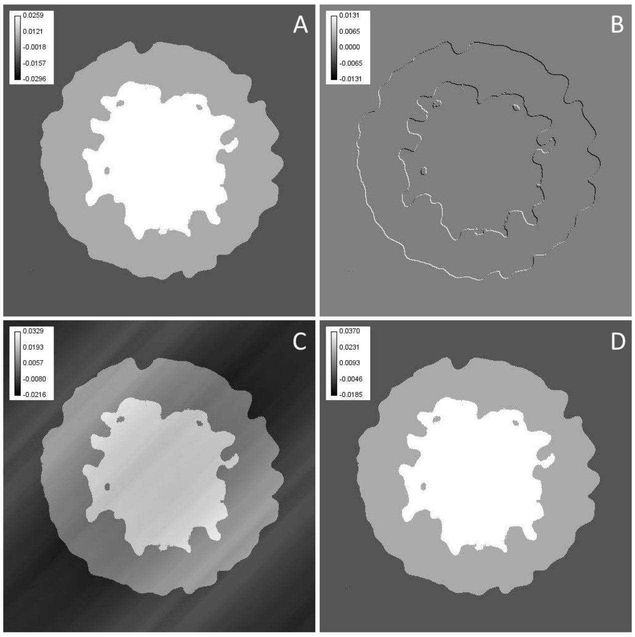
A
0.0259
0.0121
-0.0018
-0.0157
-0.0296
B
0.0131
0.0065
0.0000
-0.0065
-0.0131
C
0.0329
0.0193
0.0057
-0.0080
-0.0216
D
0.0370
0.0231
0.0093
-0.0046
-0.0185

Figure 4.22: Synthetic bilayer-like phase and differential phase images. The synthetic bilayer-like phase image **A** and the corresponding DIC image **B** were calculated. The phase image retrieved from **B** is shown in **C** using Wiener deconvolution $\kappa = 10^5$, and in **D** using the energy minimization with parameters $\alpha = 1$, $\lambda = 10^{-7}$, $\eta = 1$,$S(\nabla\varphi) = (|\nabla\varphi|^{\alpha})$, $\mathbf{u} = 1$ pixel, after 10^7 iterations. Image size = 500×500 pixels.

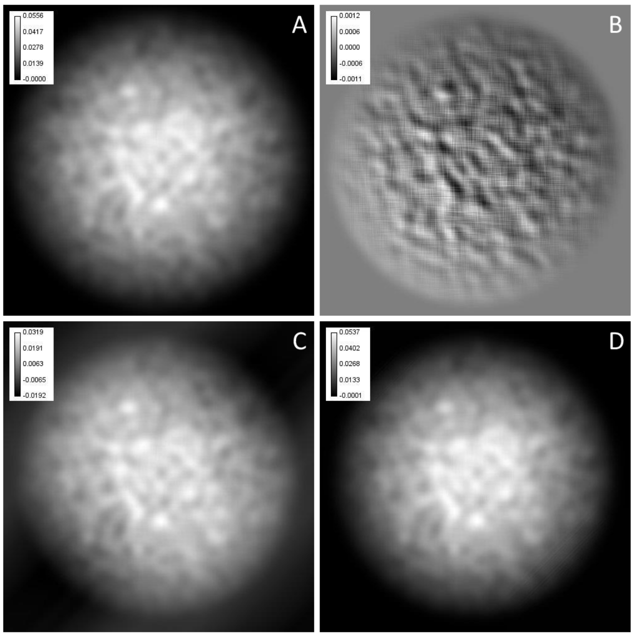
A
0.0556
0.0417
0.0278
0.0139
-0.0000
B
0.0012
0.0006
0.0000
-0.0006
-0.0011
C
0.0319
0.0191
0.0063
-0.0065
-0.0192
D
0.0537
0.0402
0.0268
0.0133
-0.0001

Figure 4.23: Synthetic smooth object phase and differential phase images. The synthetic smooth object phase image **A** and the corresponding DIC image **B** were calculated. The phase image retrieved from **B** is shown in **C** using Wiener deconvolution $\kappa = 10^5$, and in **D** using the energy minimization with parameters $\alpha = 2^{-1/2}$, $\lambda = 10^{-8}$, $\eta = 1$, $S(\nabla\varphi) = (|\nabla\varphi|^{\alpha})$, $\mathbf{u} = 1$pixel, after 10^7 iterations. Image size = 500×500 pixels.

To compare the energy minimised images with the base truth images (shown in figures 4.22 and 4.23), the error relative to the base truth phase image is calculated as

$$\Delta_{\mathrm{BT}} = \log_{10}(||(\varphi_{\mathrm{n}} - \langle\varphi_{\mathrm{n}}\rangle) - (\varphi_{\mathrm{BT}} - \langle\varphi_{\mathrm{BT}}\rangle||) \tag{4.13}$$

where φ_{n} is the energy minimised image after i iterations, and φ_{BT} is the base truth image. The mean was subtracted as it cannot be determined, since only spatial gradients are affecting the differential phase δ and the smoothing factor. The evolution of Δ_{BT} with iteration number (equation 4.11) is shown in figure 4.24 for the synthetic bilayer-like image.

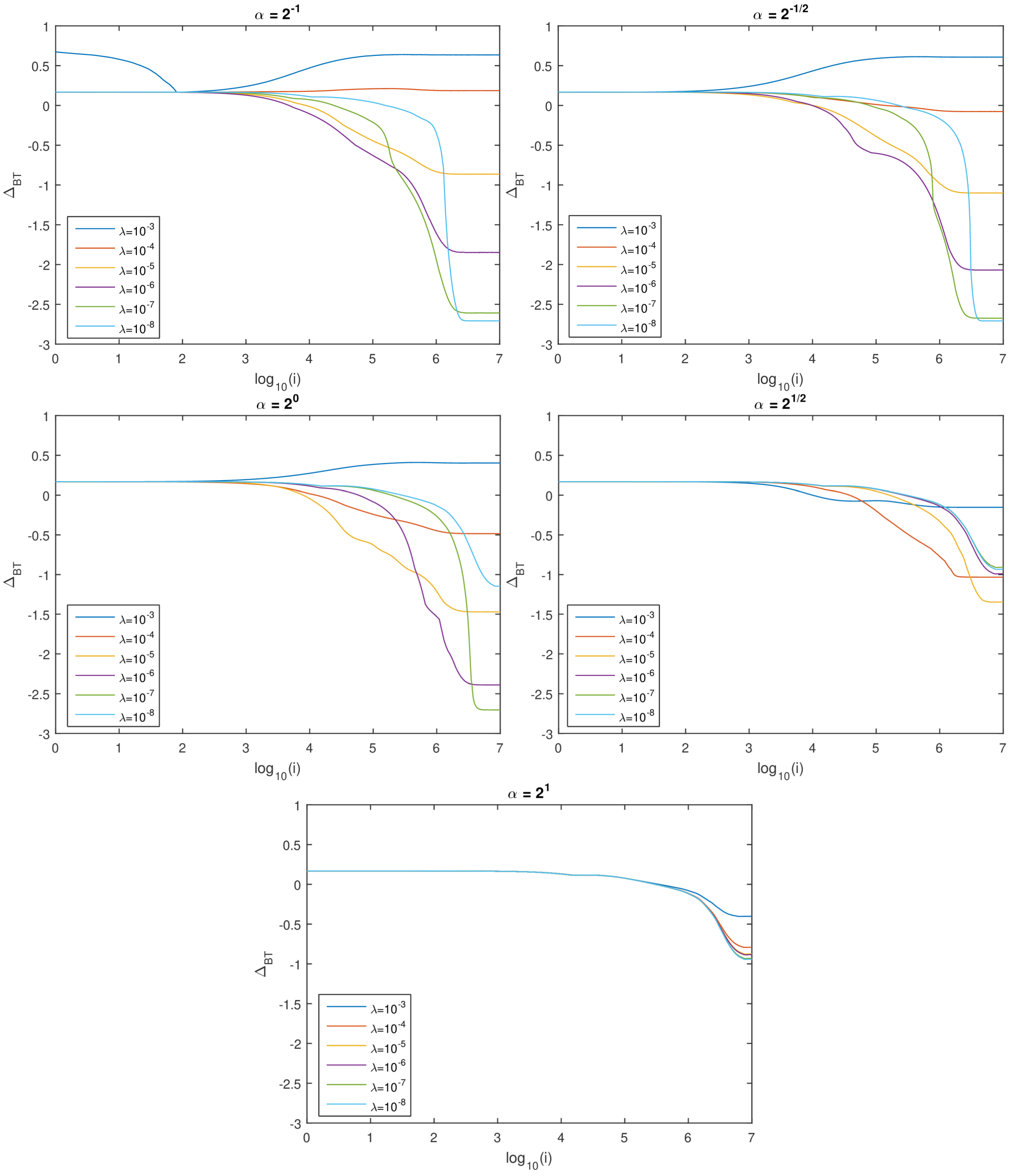

Figure 4.24: Error Δ_{BT} of the retrieved phase versus iteration number i of the energy minimization for the synthetic bilayer-like image with $S = |\nabla\varphi|^{\alpha}$, for different α and λ as given.

For this image which contains step-like features, there are three ranges of smoothing factors for both $S = |\nabla\varphi|^\alpha$ and $S = |\mathbf{u}^\perp \cdot \nabla\varphi|^\alpha$. For factors that are too large: $\lambda \geq 10^{-4}$ for $\alpha = 2^{-1}$, $\lambda = 10^{-3}$ for $\alpha = 2^{-1/2}$ and $\lambda = 10^{-3}$ for $\alpha = 2^0$, Δ_{BT} is increasing with the number of iterations starting from the Wiener filtered image, and the resulting image has an oscillating appearance, indicating an instability.

For intermediate factors $\lambda = 10^{-5}$ to 10^{-6} for $\alpha = 2^{-1}$, $\lambda = 10^{-4}$ to 10^{-6} for $\alpha = 2^{-1/2}$ and for $\alpha = 2^0$, the error is decreasing, faster for larger λ, but reaching a converged value which is lower for smaller λ. For even smaller factors $\lambda = 10^{-7}$ to 10^{-8} for $\alpha = 2^{-1}$ and $\alpha = 2^{-1/2}$ and $\lambda = 10^{-7}$ for $\alpha = 2^1$, the converged error is again increasing with decreasing factors. Notably, a consistently smaller error can be achieved when using the $S = |\mathbf{u}^\perp \cdot \nabla\varphi|^\alpha$ condition in comparison with the $S = |\nabla\varphi|^\alpha$ condition.

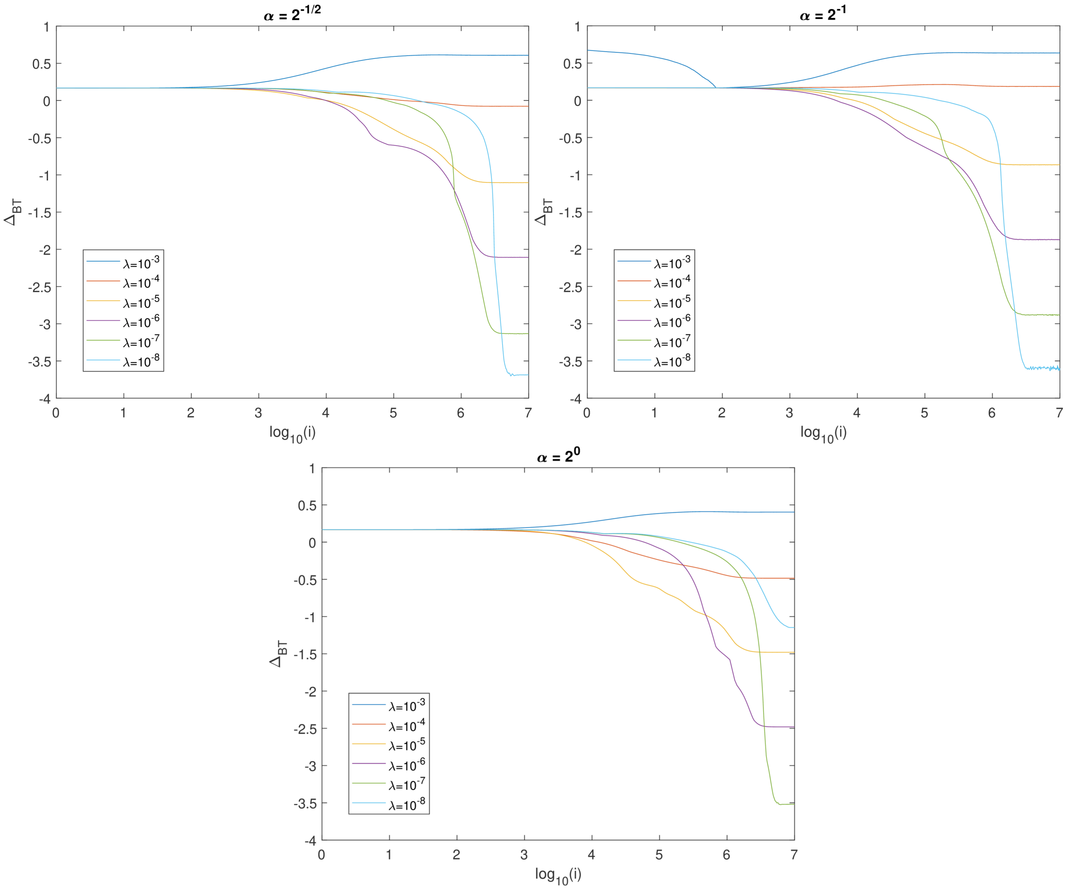

Figure 4.25: As figure 4.24, but using $S = |\mathbf{u}^\perp \cdot \nabla\varphi|^\alpha$.

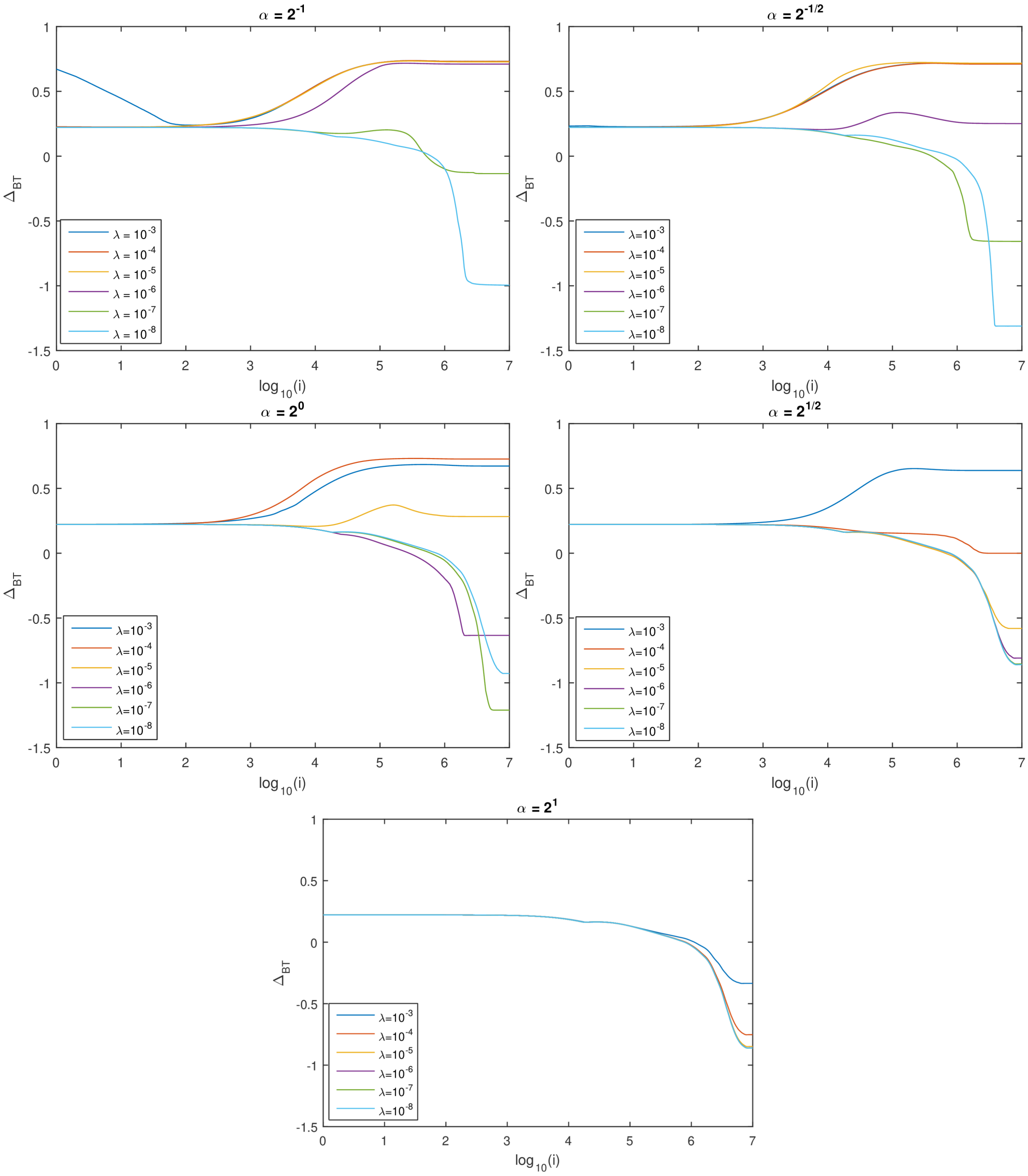

Figure 4.26: Error Δ_{BT} of the retrieved phase versus iteration number i of the energy minimization for the smooth object with $S(\nabla\varphi) = |\nabla\varphi|^{\alpha}$ for different α and λ as given.

A similar behaviour is found for the smooth object as shown in figure 4.26. Again there are smoothing factors which are too large which results in images with an oscillating appearance. These are $\lambda \geq 10^{-6}$ for $\alpha = 2^{-1}$ and $\alpha = 2^{-1/2}$, $\lambda \geq 10^{-5}$ for $\alpha = 2^{-1}$. Intermediate factors which cause the error to decrease quickly are $\lambda = 10^{-8}$ for $\alpha = 2^{-1}$, $\lambda = 10^{-7}$ for $\alpha = 2^{-1/2}$, $\lambda = 10^{-6}$ for $\alpha = 2^{0}$. The small factors which result in the lowest error upon converging are $\lambda = 10^{-8}$ for $\alpha = 2^{-1}$, $\lambda = 10^{-8}$ for $\alpha = 2^{-1/2}$ and $\lambda = 10^{-7}$ for $\alpha = 2^{-1}$. When comparing the errors for $S = |\nabla\varphi|^{\alpha}$ and $S = |\mathbf{u}^{\perp} \cdot \nabla\varphi|^{\alpha}$, no significant difference in the evolution of Δ_{BT} was observed for the smooth object.

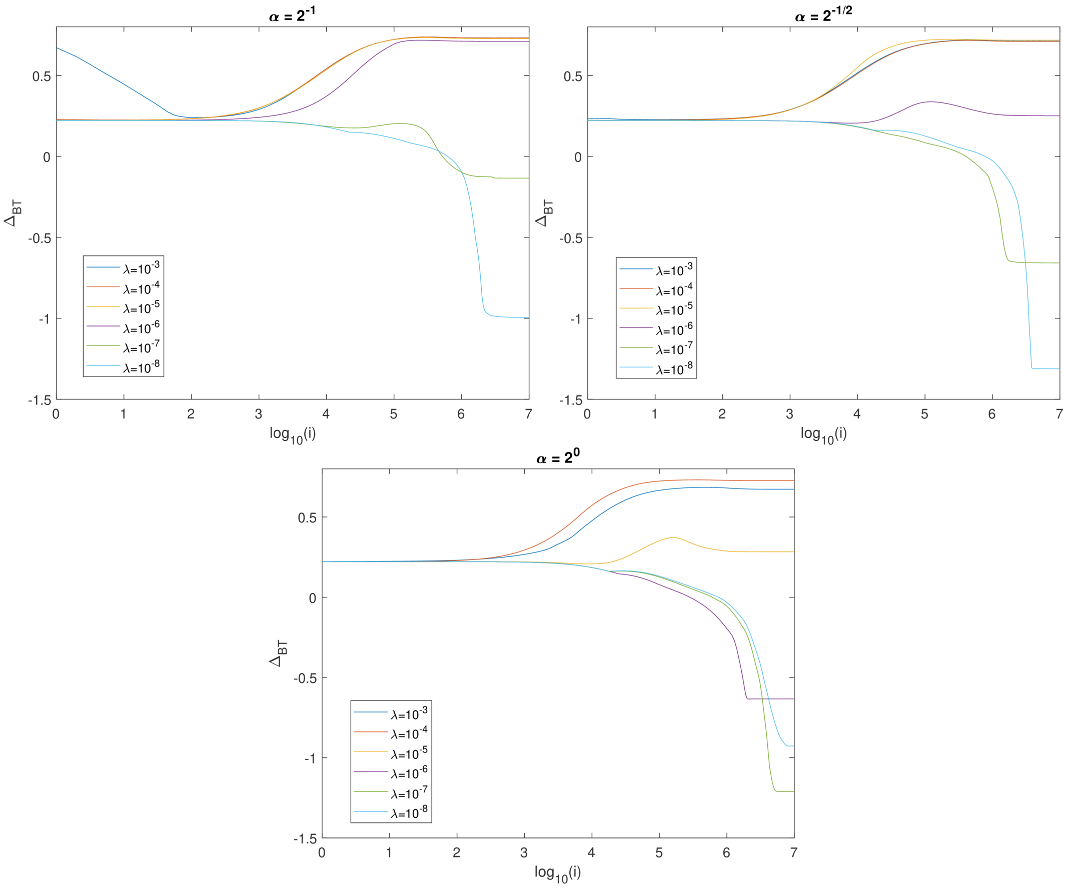

Figure 4.27: As figure 4.26, but using $S = |\mathbf{u}^{\perp} \cdot \nabla\varphi|^{\alpha}$.

In using a Graphics Processing Unit (GPU), the time which the algorithm needs to reach a converged status is reduced significantly. With the use of parallel processing of several images, this further reduces the time in which a convergence is achieved, as multiple images are processed in each iteration, to use the many cores of the GPU (e.g 3584 in the GTX 1080TI used here). Note that single precision floating point (4 bytes per number) was used in all calculations. To optimize convergence speed and final value, it is therefore best to vary the smoothing factor with time, starting from a higher value in the intermediate regime, for fast convergence, and then decreasing the factor to result in a smaller final deviation. This would be done dynamically, observing the speed of convergence for two (or more) different smoothing factors (λ) and then choosing the one with faster convergence, and using for the next convergence period a new factor changed accordingly. To implement this an algorithm would be developed to monitor the evolution of Δ_{BT}, requiring the need for a base truth φ image. Smoothing factors (λ) above and below the optimal choice at iteration i will be used until the end of the user defined convergence period, where the process would be repeated. Judging by the evolution of Δ_{BT} for the synthetic bilayer-like object and the smooth object, the proposed algorithm with dynamically changing smoothing factors (λ) process could reduce the time required for reaching a convergent status by approximately 10 times. The time required for completing 10^7 iterations on the synthetic bilayer-like object and smooth object on 6 images took approximately 72 hours.

In summary, this workflow brings together a method by which a user may image objects in DIC, create a contrast image which is background corrected, integrate the image, at which point the user may extract quantitative information about the thickness of the specimen under scrutiny. The images may then be qualitatively improved through the use of energy minimisation whilst also retaining the edge heights of objects and providing an approximation to the phase distribution of the areas that are not close to phase edges which may be obscured by the striping artefacts that are introduced at the Wiener-like deconvolution stage.

4.10 Extracting Thickness from samples

In order to extract the thickness Δt from a phase profile derived from integrated DIC images (see Figure 4) the following equation is used:

$$\Delta t = \frac{\lambda_0 \Delta\varphi}{2\pi|n_s - n_m|} \tag{4.14}$$

where $\Delta\varphi$ is the change in phase,λ_0 is the central wavelength used in illuminating the sample, and n_s and n_m are the refractive index of the sample and the medium respectively.

4.10.1 SU-8 Waveguide

The thickness Δt of the SU-8 waveguide using the peak and trough values from the line plot shown in 4.3 (signal to noise parameter $\kappa = 10,000$) was measured as 554±21.3nm. A Dektak stylus profilometer was also used to characterise the SU-8 sample by Robin Islam which gave an average thickness of 519±13nm for the waveguide sample. The qDIC thickness measurement shown here is in agreement with the DekTak stylus profilometer measurements within 10% relative error, which is consistent with measurements made on SU-8 waveguides within Robin Islam's PhD thesis. [83] Images were acquired with a 5ms acquisition time with 256 frame averages, and polariser angle of $\theta = 45°$ was used.

4.10.2 Lipid bilayers

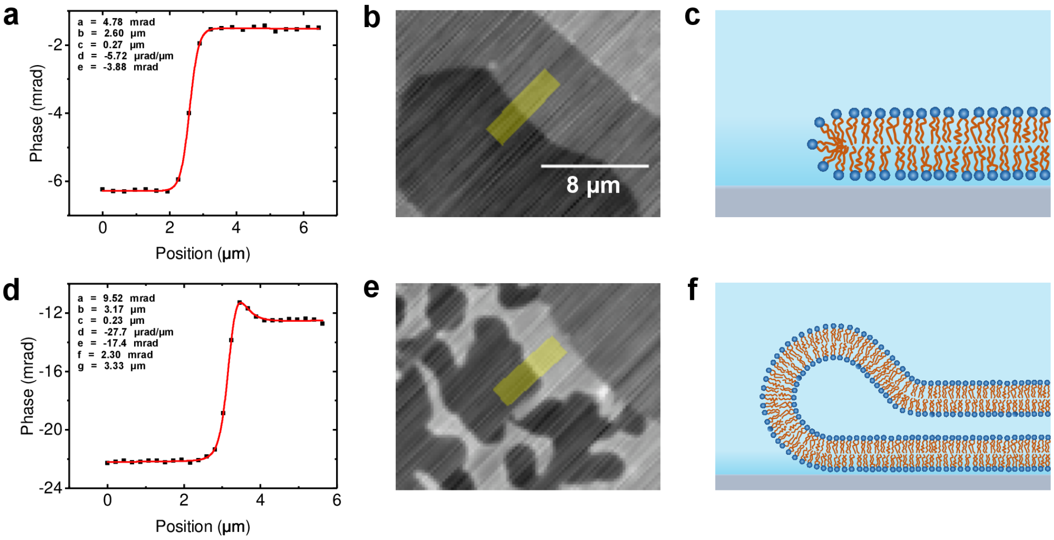

Figure 4.28: Examples of phase profiles taken over bilayer edges. A typical profile over a single bilayer edge fitted with equation 4.15 is shown in (a), with (b) showing the corresponding qDIC phase image, on a gray scale from -12 to +13 mrad. The region from which the profile was extracted is shaded in yellow. (c) Sketch of a corresponding bilayer edge structure (not to scale). Panel (d) shows a fit to a double bilayer step, incorporating the sech term to accomodate a hump in the phase profile, with (e) showing the corresponding qDIC phase image, on a gray scale from -30 to 0 mrad. (f) Sketch of a corresponding bilayer edge structure. The qDIC phase images (b,e) are not treated with the energy minimization process. (Reproduced with permission from [88])

The qDIC method has been used in order to probe sub-nanometre thickness changes in supported lipid bilayers [88], and the method by which the thickness of stacks of bilayers was measured is shown in figure 4.28. Here, line plots from a phase image (φ) of a lipid bilayer sample DC$_{15}$PC:Atto488-DOPE(99.9:0.1) were fitted with equation 4.15 in order to extract the thickness of stacks of bilayers Δt using equation 4.14, using the curve fitting tool in MATLAB. The equation that was fitted to the line plots is as follows.

$$\frac{a}{2}\tanh\left(\frac{\mathrm{x}-\mathrm{b}}{\mathrm{c}}\right)+\mathrm{dx}+\mathrm{e} \tag{4.15}$$

where a is taken to be the height of the bilayer in rad. Line plots from 0 bilayers to 1 bilayer, 0 bilayers to 2 bilayers and 1 bilayer to 2 bilayers were measured. The average thickness extracted from fits from line plots in figure 4.29 for 0 to 1 bilayers was 3.54±0.23nm, for 0 to 2 bilayers 7.39±0.25nm, and for 1 to 2 bilayers 3.71±0.56nm (averaged over 5 line line plots). These values are consistent for measurements (made by a colleague in the Biophotonics and Optoelectronics group, David Regan) on DC$_{15}$PC:Atto488-DOPE(99.9:0.1) in the fluid ordered phase.[87] The qDIC method was used in this way to measure thickness changes during phase transitions of supported lipid bilayers [89]. DIC images of the lipid bilayer were acquired with the used of a 20× objective, with a polariser angle of θ =12.9°, acquisition time 100ms and no averaging. A signal to noise parameter of $\kappa = 4000$ was used to produce the phase image shown in figure 4.29.

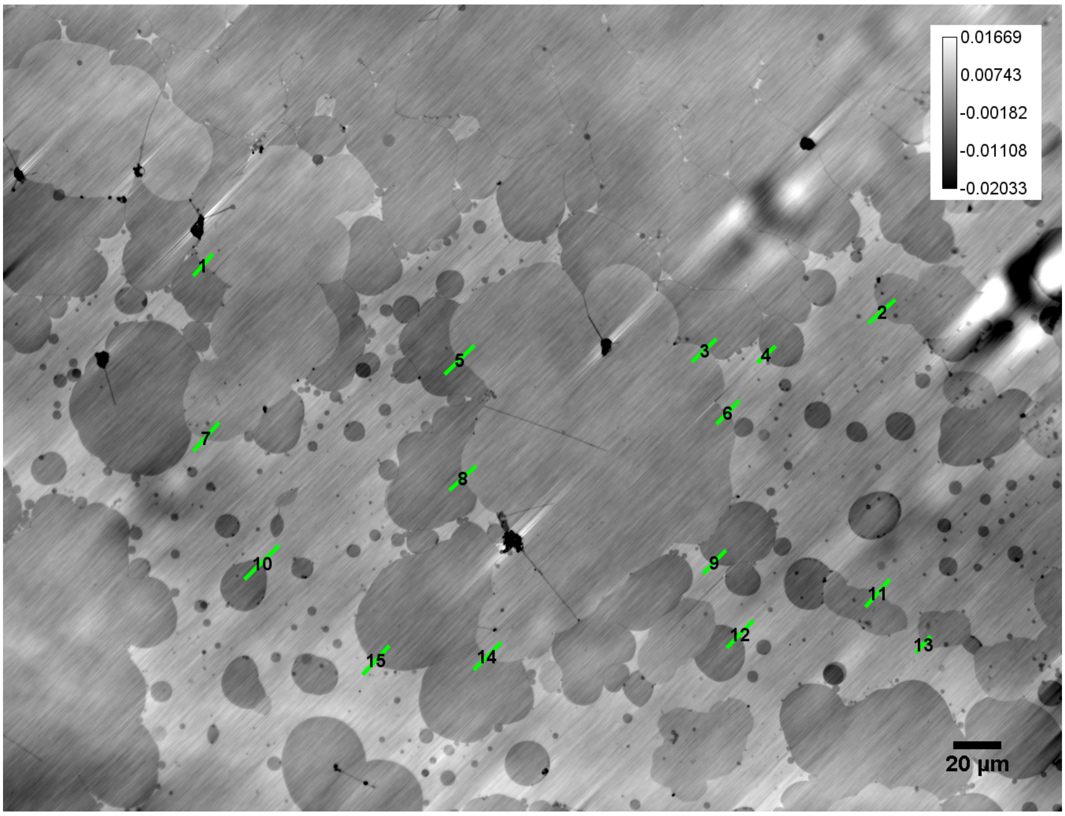
0.01669
0.00743
-0.00182
-0.01108
-0.02033
1
2
3
4
5
6
7
8
9
10
11
12
13
14
15
20 µm

Figure 4.29: Line plots taken over edges of stacks of supported lipid bilayers ($DC_{15}PC$:Atto488-DOPE(99.9:0.1)). Darker areas correspond to thicker stacks of bilayers.

Chapter 5

Correlative Extinction, Epi-fluorescence and FWM microscopy

As discussed in Chapter 1, gold nanoparticles have been researched for many biomedical applications in diagnostics, theranostics, and as drug delivery systems. When conjugated to fluorophores, their interaction with biological cells can be studied *in situ* and in real time using fluorescence microscopy. However, an important question that has remained elusive to answer is whether the fluorophore is a faithful reporter of the nanoparticle location.

This Chapter addresses this question, both experimentally and through the development of a quantitative data analysis methodology. The experiments combine new measurements, which I have acquired, with previous results obtained in the Biophotonics laboratory by the former PhD student Naya Giannakopoulou [1]. The data analysis comprises a methodology to calculate the cross-correlation coefficients (also known as Pearson's coefficient) which I have developed, in order to quantify the degree of co-localisation between images acquired with different optical microscopy techniques.

5.1 Quantitative data analysis: Cross-correlation

A quantitative cross correlation algorithm (written in MATLAB) has been developed here which calculates the image cross-correlation as a function of the relative translation and rotation coordinates between two images. The algorithm can then be used to: i) determine if there is significant spatial overlap across two images, ii) provide the values of relative translation and rotation needed to overlay the images, iii) quantify the cross-correlation coefficient (also known as Pearsons' coefficient). Firstly, input images are prepared in a format such that they have the same pixel size in micron units. Implementing a relative translation in the (x,y) plane between

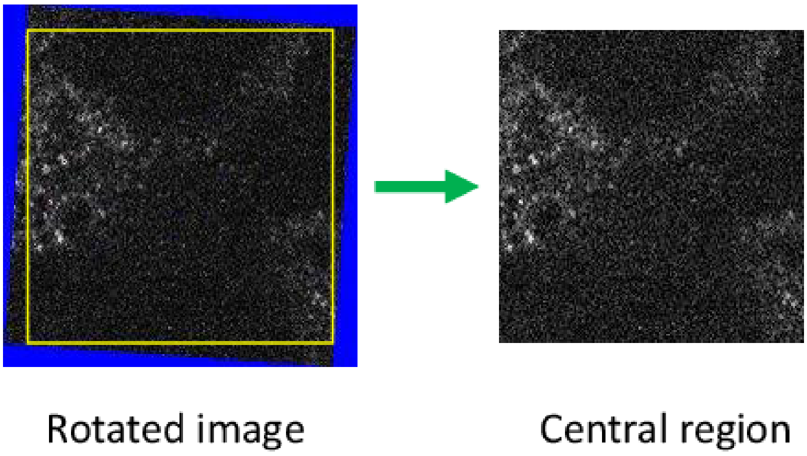

Figure 5.1: The extraction of the central portion of a rotated image. The region highlighted in blue contains zeros, therefore the rectangular region outlined in yellow is extracted from the image. This can be used to be laterally shifted relative to another image.

two images is relatively straightforward (see Appendix for a copy of the algorithm in section C). However, implementing a relative rotation and consequently calculating the cross-correlation is less trivial. In order to do so, one input image is rotated with respect to the other by an adjustable angle, typically in one-degree increments, (using the MATLAB imrotate function), and the central portion is extracted from the rotated image in order to recover a squared or rectangular frame shape (see Appendix for a copy of the algorithm in section B). Briefly, this is done by rotating a binary mask of the same size as the inputted image where the area representing the image is mapped with a value of 1 for each pixel of the image, and zero for the area that surrounds the rotated image (as shown in figure 5.1). The largest rectangular area within the rotated image was found through mapping the largest rectangular area which did not contain zeros within the rotated mask image. The peak Pearson's coefficient values from the cross correlation maps for varying angular and lateral shifts between images can then be used as a tool to determine if there is a significant overlap of spatial pattern between the images, and for which values of relative translation and rotation coordinates this occurs. To calculate the Pearson coefficient for each shift position, the following equation was used:

$$r_p = \frac{\sum_i (A_i - \overline{A}) \times (B_i - \overline{B})}{\sqrt{|\sum_i (A_i - \overline{A})^2| \times |\sum_i (B_i - \overline{B})^2|}} \tag{5.1}$$

where A_i and B_i are the intensities in pixel i in the two images A and B to be cross correlated, and $\bar{A}$ and $\bar{B}$ are the average intensity of image A and B. Upon shift and rotation of one image relative to the other, the summation runs over the overlap area between A and B. Specifically to correlate the fluorescence and FWM images, an angular shift was introduced to the MATLAB script as the samples were imaged using different microscopes where the sample orientation may have not been exactly the same on the two instruments. The correlation maps, namely r_P versus x, y translation shifts and relative rotation angle θ, are then used in order to build overlay images. The peak of the correlation map is used to ascertain the shift between two images. To indicate what a strong correlation looks like using the developed algorithm for normalised cross-correlation, correlation maps between two identical sample images and two different sample images are shown in figure 5.2. The normalised cross-correlation map produced between two similar images (with a high spatial correlation) produces a strong peak near the centre of the map. In a cross-correlation map produced between two dissimilar images, there is no such clear peak near the centre of the map. This normalised cross-correlation algorithm differs from the in-built MATLAB function normxcorr2(template,A), which calculates the normalised cross-correlation map between an image A and a template, which would be the closest in-built alternative.

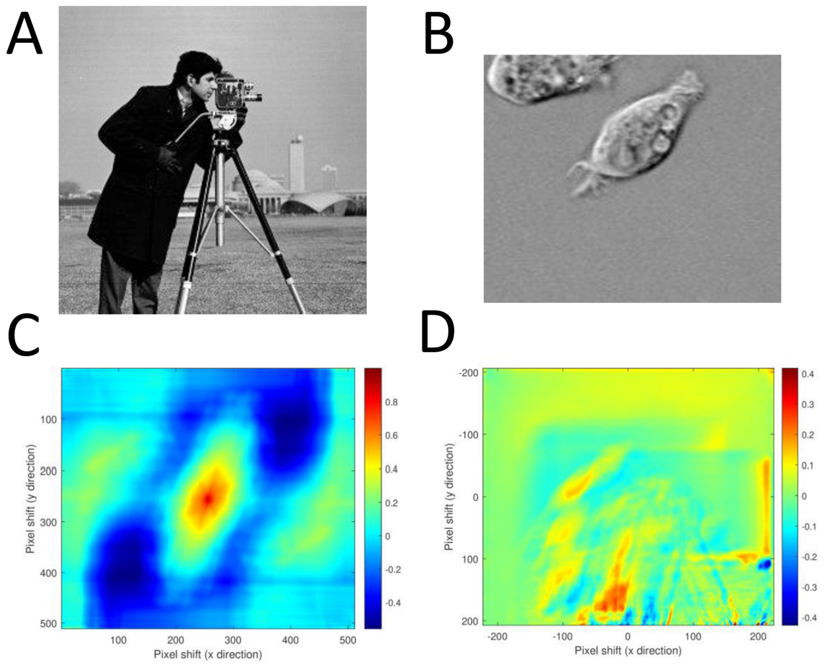

Figure 5.2: Cross correlation results from sample images. **A** and **B** are sample images, **C** shows a cross correlation map where the image shown in **A** is cross correlated with itself, which gives a cross correlation peak with a value of 1 at the centre of the map. **D** shows the cross correlation between the images shown in **A** and **B**. There is no clear peak at the centre of this correlation map as there is a distinct lack of spatial correlation between the two images.

The equation that is closely followed by the normxcorr2 algorithm is the following.

$$\gamma(u,v) = \frac{\sum_{x,y}[f(x,y) - \bar{f}_{u,v}][t(x-u, y-v) - \bar{t}]}{\sqrt{\sum_{x,y}[f(x,y) - \bar{f}_{u,v}]^2 \sum_{x,y}[t(x-u, y-v) - \bar{t}]^2}} \tag{5.2}$$

where f is the image, $\bar{t}$ is the mean of the template and $\bar{f}_{u,v}$ is the mean of $f(x, y)$ in the region under the template. At zero shift between the cross correlated images, both methods yield the same normalised cross correlation coefficient value. For our purposes, it was important to get the Pearson's coefficient of two equally sized and relatively shifted images, which is not possible using equation 5.2, as this assumes a template of smaller size than the image.

5.2 Experimental results

In Naya Giannakopoulou's PhD thesis [1], the intracellular fate of AuNP-fluorophore conjugates loaded into HeLa cells was studied with correlative Four Wave Mixing (FWM) and fluorescence imaging. A lack of colocalisation between the fluorophore label and the supposedly conjugated AuNP was reported. A more direct correlative wide-field fluorescence and extinction study to probe the colocalisation of signal from fluorophores and AuNPs was performed by myself, and is discussed in this section. A further discussion of the results from Giannakopoulou's PhD which motivated this work are found in section 5.4.

The constructs probed in this study are the 20nmAuNP-PC-Ab(A647) and 10nmAuNP-SA(A488), described in the Materials and Methods chapter. Briefly, the 20nmAuNP-PC-Ab(A647) comprises AuNPs of 20nm diameter, covalently bound to the dye Alexa647 via a polymer coating-antibody system. The 10nmAuNP-SA(A488) comprises 10nm diameter AuNPs onto which streptavidin labeled with the dye Alexa488 is adsorbed. When imaging the 20nmAuNP-PC-Ab(A647) construct, finding the surface of the coverslip was possible in transmission due to the presence of AuNP aggregates. To acquire extinction images of the 10nmAuNP-SA(A488) construct, 60nm AuNPs (BBI solutions) were also deposited onto the coverslip as they provide a strong source of contrast in transmission to aid the process of bringing the surface of the coverslip into focus. Once the 60nm particles were found within the field of view, a epi-fluorescence time course would be acquired (36×10s acquisitions).

The shift method was used in order to image the AuNPs in extinction. At each position, 500 images (acquisition time 100ms) were averaged to reduce the effects of shot noise on the Extinction image (see Materials and Methods). In order to verify that the AuNPs were not dielectric debris, images were taken at different positions axially. Through focus, the contrast from an individual absorbing metallic nanoparticle maintains the appearance on an absorption "dip" in a transmission image, whereas dielectric debris change contrast, transitioning from appearing as dark to becoming bright spots when traversing the sample in the axial direction. This is due to the fact that the extinction cross section is dominated by the absorption cross section for AuNPs with a diameter of 10nm, and dielectric debris has a significant scattering cross section. A series of extinction images acquired through focus are shown in figure 5.3, where 60nm and 10nmAuNP-SA(A488) particles are visible along with dielectric debris.

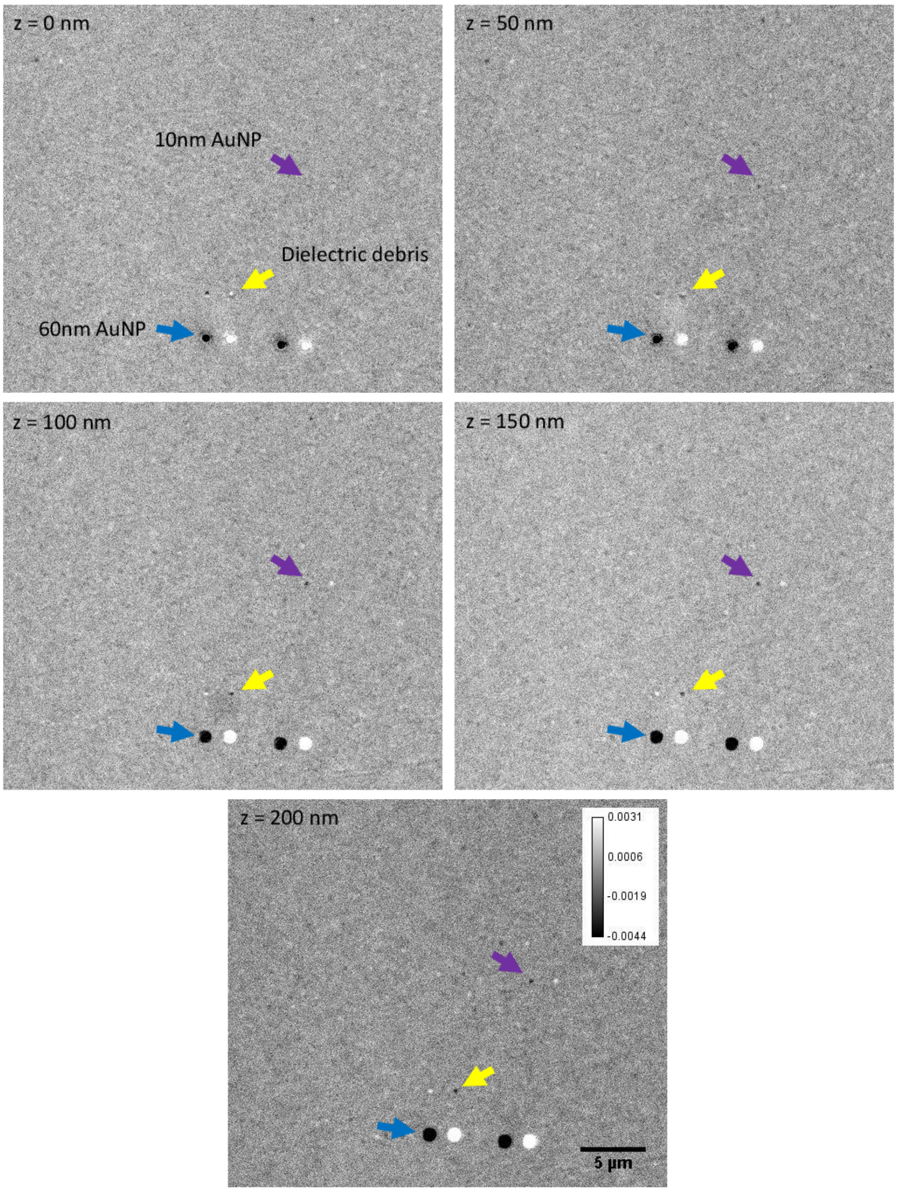

Figure 5.3: Extinction images through focus for the 10nmAuNP-SA(A488) sample. Examples of 10nm AuNPs (purple arrows), 60nm AuNPs (blue arrows) and dielectric debris (yellow arrows) are marked in extinction images acquired through focus. The 60nm AuNPs provide strong contrast in comparison with the 10nm AuNPs, and dielectric debris can be distinguished from metallic particles as the contrast from the debris inverts in contrast as it is imaged through focus, whereas the contrast from metallic particles does not.

Fluorescence measurements for the 20nmAuNP-PC-Ab(A647) and 10nmAuNP-SA(A488) samples were performed in air to keep fluorophores attached to the surface of these constructs. This was done to ensure that the fluorophores did not detach into a solvent, and also to avoid the adding an of a medium which could fluoresce itself. For the 10nmAuNP-SA(A488) sample, fused silica coverslips were used in order to minimise autofluorescence from point-like defects, which can be significant when imaging standard glass under the excitation conditions necessary for Alexa488. Examples of wide-field fluorescence images measured on the 20nmAuNP-PC-Ab(A647) and 10nmAuNP-SA(A488) samples can be seen in figures 5.4 and 5.5 respectively, along with fluorescence images measured on fused silica and glass coverslips, under the same excitation/detection conditions, for comparison.

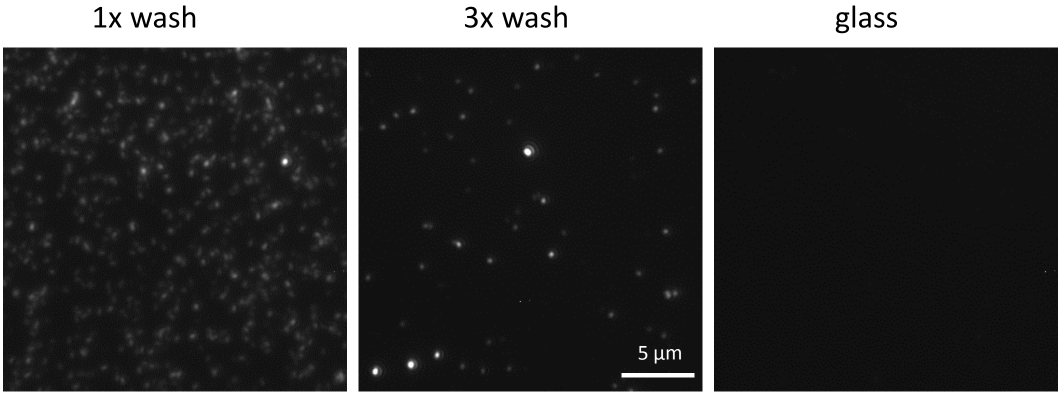

Figure 5.4: Fluorescence measured on 20nmAuNP-PC-Ab(A647) deposited onto a glass coverslip in air. The left and center images are the same images as in figure 5.6. The right image shows the results on a glass coverslip without 20nmAuNP-PC-Ab(A647). All images are plotted on the same grey scale, which is the one used in figure 5.6 for the 1× washed sample.

10nmAuNP-SA(A488) were imaged first in air for fluorescence microscopy, and subsequently in oil which was matched to the refractive index of fused silica ($n = 1.46$) for extinction microscopy. For this sample, we used the 1.27NA objective with correction collar to compensate for spherical aberrations. Notably, part of the excitation in fluorescence microscopy undergoes total internal reflection at the glass-air interface. This gave rise to a relevant background detected by the camera, of 200-300 counts over 10s. To account for this background, we acquired a time course of 36 images (each with 10s exposure) over which photo-bleaching of A488 occurs. We then subtracted the average of the last two frames from the average of the first two frames, to remove the background. These background-subtracted images are the ones shown in Fig.5.4. The oil was inserted *in situ* during microscopy, using a partially cut gasket forming a channel, and a connecting tube which allowed injection of the oil into the imaging chamber via a syringe without removing the sample, for correlative extinction and fluorescence microscopy (see Materials and Methods Chapter 3). Addition of the index matching oil was required to reduce the background due to surface roughness in the extinction measurements, specifically important when imaging AuNPs of small diameters such as for the 10nmAuNP-SA(A488) sample.

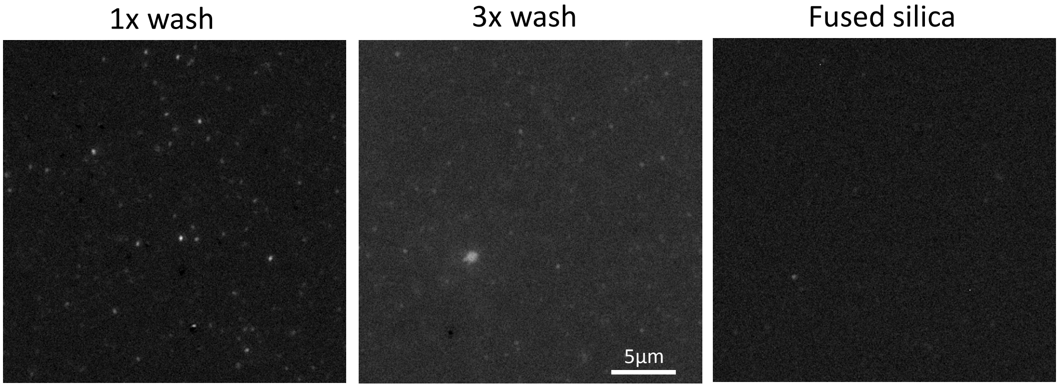

Figure 5.5: Fluorescence measured on 10nmAuNP-SA(A488) deposited onto a fused silica coverslip in air. The left and center images are the same images as in figure 5.8. The right image shows the results on a fused silica coverslip without 10nmAuNP-SA(A488). All images are on the same grey scale as in figure 5.8.

5.3 Correlative wide-field fluorescence and extinction microscopy of 20nmAuNP-PC-Ab(A647) and 10nmAuNP-SA(A488)

The correlative widefield fluorescence and extinction images of the 20nmAuNP-PC-Ab(A647) sample are shown in figure 5.6. A wash protocol recommended by the manufacturer was followed once (1×) and three times (3×) as described in section 3.2.1. Qualitatively, it appears that the 1× washed sample contains significantly more unbound fluorophores, compared with the 3× wash, given the number density of 20nmAuNP visible in the corresponding extinction images. Figure 5.6 also shows the extinction cross sections measured as described in Chapter 2.2.5 (see also Materials and Methods Chapter 3) and corresponding diameters (using Mie theory in the dipole limit, see Chapter 2.2.3) from particles imaged with extinction microscopy.The cross correlation images $r_{\mathrm{P}}(\Delta x, \Delta y)$ versus relative in-plane translation coordinates for the 20nmAuNP-PC-Ab(A647) sample are shown in figure 5.7. For the 1× washed sample the peak cross correlation value was $r_{\mathrm{P}} = 0.099$, which is quite small, denoting poor co-localisation between AuNPs and fluorophores, supporting the conclusion that there are indeed a significant amount of unbound fluorophores in the sample. For the 3× washed sample, a peak cross correlation value of $r_{\mathrm{P}} = 0.476$ shows that the co-localisation between AuNP and fluorophore has improved, consistent with the expectation that the number of unbound fluorophores is significantly reduced after 3× washes. Note that the wash protocol recommended by the manufacurers was followed, in order to obtain a conjugate that is nominally 100% free from unbound antibody. The results presented here show that after 3 washes the 20nmAuNP-PC-Ab(A647) construct is still not 100% free from unbound dyes.

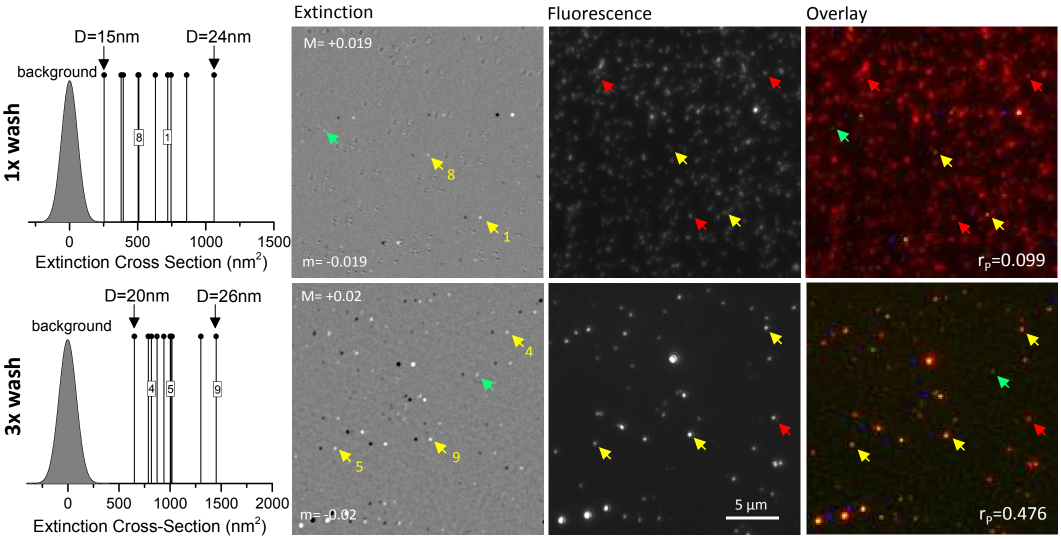

Figure 5.6: 20nmAuNP-PC-Ab(A647) imaged by correlative wide-field fluorescence and extinction microscopy. The AuNP solution was washed once (top) or 3 times (bottom) to reduce the presence of unbound antibodies. AuNPs were deposited on glass and imaged in air. Extinction cross-sections of ten representative single particles in the FOV are indicated on the left panels, with corresponding particle diameter ranges, above the detection limit (background histogram, see text). Extinction contrast images are shown on grey scale from m (black) to M (white), as indicated, with yellow arrows pointing to selected single AuNPs for which the cross-section was quantified, as labelled (images shown are 30% of the FOV). Fluorescence images of the same area are shown on a grey scale from $0.03\mathrm{F_m}$ to $0.39\mathrm{F_m}$ (top) and from $0.03\mathrm{F_m}$ to $0.22\mathrm{F_m}$ (bottom), with $\mathrm{F_m}$ being the maximum amplitude in the FOV. Overlay: fluorescence (red), extinction maxima (green) extinction minima (blue). In the overlay, amplitudes are re-scaled to maximize colour overlap. Green arrows indicate AuNPs visible only in extinction. Red arrows indicate unbound fluorophores. The cross-correlation (Pearson's) coefficient r_P is given.

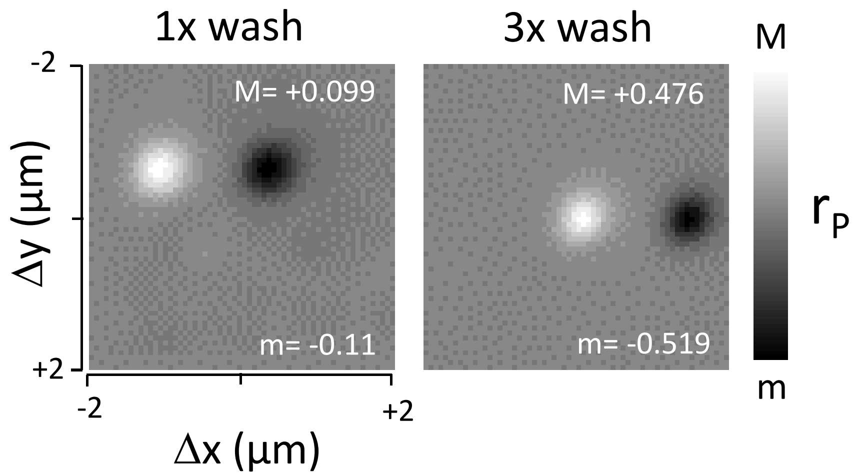

Figure 5.7: Cross correlation coefficient r_P as a function of relative translation (Δx,Δy) coordinates for the 20nmAuNP-PC-Ab(A647) construct shown in figure 5.6.

The correlative widefield fluorescence and extinction imaging of 10nmAuNP-SA(A488) is shown in figure 5.8. Qualitatively, one can see that there is a distinct lack of correlation between the widefield fluorescence and the extinction image. Notably here the correlation between the images from the 3× washed sample is still quite low. These results contrast with those found for the 20nmAuNP-PC-Ab(A647) sample, where the extinction and wide-field fluorescence images exhibit a significant degree of correlation for the 3× washed sample. The cross correlation images $r_{\mathrm{P}}(\Delta x, \Delta y)$ for the 10nmAuNP-SA(A488) sample, shown in figure 5.9, quantitatively confirm no significant correlation between the extinction and widefield fluorescence images, with small values of r_{P} overall. A reduction of unbound fluorophores is observed in the 3× washed sample compared with the 1× washed sample, however the observed AuNPs are mostly not fluorescent. In essence, our results clearly show that, in this commercial product, the fluorophore label does not provide any reliable information about the AuNP location.

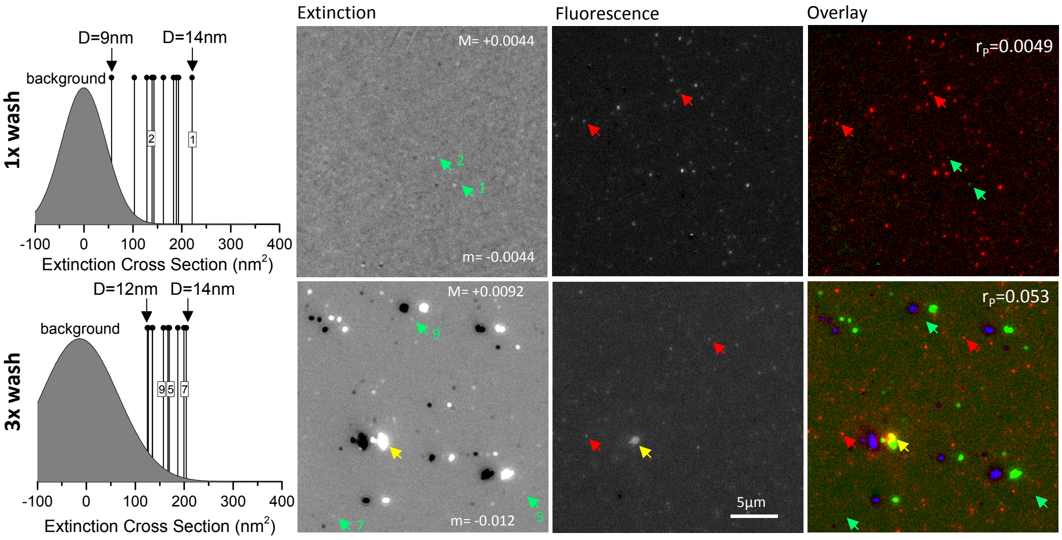

Figure 5.8: 10nmAuNP-SA(A488) imaged by correlative wide-field fluorescence and extinction microscopy. The AuNP solution was washed once (top) or 3 times (bottom) to reduce the presence of unbound streptavidin. AuNPs were deposited onto fused silica coverslips and imaged by wide-field fluorescence microscopy in air, followed by extinction microscopy in index matched oil. Extinction cross-sections of ten representative single particles in the FOV are indicated on the left panels, with corresponding particle diameter ranges, above the detection limit (background histogram, see text). Extinction contrast images are shown on grey scale from m (black) to M (white), as indicated, with green arrows pointing to selected single AuNPs for which the cross-section was quantified, as labelled (images shown are 30% of the FOV). Fluorescence images of the same area (after background subtraction, see text) are shown on a common grey scale from -0.1$\mathrm{F_m}$ to $\mathrm{F_m}$, with $\mathrm{F_m}$ being the maximum amplitude in the FOV for the 1× washed sample. Overlay: fluorescence (red), extinction maxima (green) extinction minima (blue). In the overlay, amplitudes are re-scaled to maximize colour overlap. Red arrows indicate unbound fluorophores. The yellow arrow indicates red-green co-localization. The cross-correlation (Pearson's) coefficient r_{P} is given.

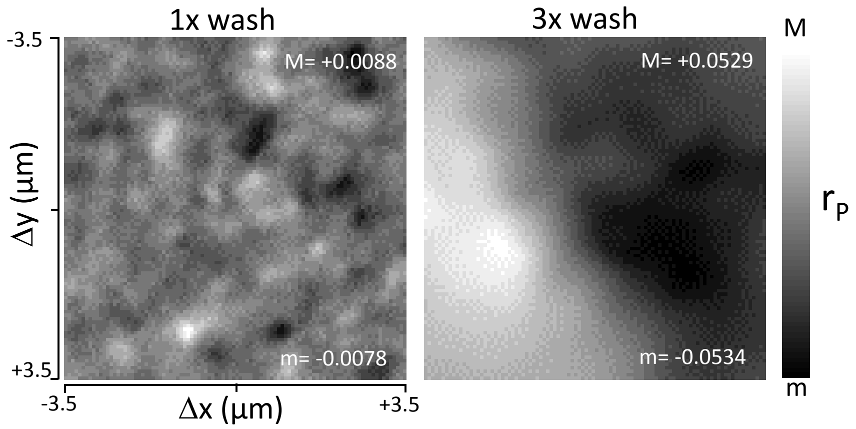

Figure 5.9: Cross correlation coefficient r_{P} as a function of relative translation (Δx,Δy) coordinates for the 10nmAuNP-SA(A488) construct shown in figure 5.8.

5.4 FWM and fluorescence correlation results

As part of Naya Giannakopoulou's work [1], AuNP-Transferrin conjugates (AuNP-Tf) within HeLa cells were investigated. Transferrin (Tf) and its receptor (TfR) are highly relevant in the context of targeted delivery of small and macro-molecular therapeutics into cancer cells [90]. It has been previously shown [82] that by targeting the plasma membrane TfR with biotinylated Tf and subsequently adding streptavidin to cross-link receptor:ligand-biotin complexes, a selective lysosomal delivery of Tf was achieved over a 6 hour time-course. The targeted delivery of (bio)therapeutics such as antibody-drug conjugates to the lysosome is a major clinical need. As a result, navigating therapeutics through the endolysosomal pathway through using this cross-linking strategy has attracted significant attention.

As mentioned in sections 1.3.3 and 1.3.2, a quantitative determination of the cross-correlation between images was required in order to assess the degree of co-localisation between AuNPs and fluorophores, following the acquisition of fluorescence images and FWM images from HeLa cells loaded with the 10nmAuNP-SA(A488)-Bi-Tf(A647) construct (see Materials and Methods 3.1.1), HeLa cells loaded with 40nmAuNP-SA-Bi-Tf(A647) (see Materials and Methods 3.1.3) and HeLa cells loaded with 15nmAuNP-PC-Tf(A488) (see Materials and Methods 3.1.2).

Prior to describing the cross-correlation analysis of these various images, it is useful to briefly explain the working principle of FWM microscopy, and in turn the type of image contrast it can provide. Note that the FWM imaging experiments were performed by Naya Giannakopoulou [1], while I implemented their quantitative analysis through the image cross-correlation method mentioned in the previous sections. The Four Wave Mixing microscopy technique developed in the Biophotonics and Optoelectronics group at Cardiff University can be described as a pump-probe scheme, where $\mathbf{E_1}$ is the pump field and $\mathbf{E_2}$ is the probe field. A 150fs pump pulse of intensity $\mathbf{E_1}\mathbf{E_1}^*$ with a central frequency at the LSPR of the AuNP is absorbed by the nanoparticle and this induces the formation of a hot electron gas within the metal. This process changes the dielectric constant of the AuNP. The resulting change in the reflection of the AuNP is resonantly probed at the LSPR by the probe pulse which arrives onto the sample at an adjustable time delay τ after the pump pulse. This results in a FWM field proportional to $\mathbf{E_1}\mathbf{E_1}^*\mathbf{E_2}$. The FWM field is separated from the $\mathbf{E_1}$ and $\mathbf{E_2}$ using heterodyne detection [47] and is therefore free from scattering backgrounds. This interferometric detection is also insensitive to fluorescence backgrounds. By varying τ, the electron dynamics can be time-resolved. These dynamics reveal the time scale of the electron-electron scattering and formation of the hot electron gas (∼100fs), the subsequent thermalisation with the lattice via electron-phonon scattering (∼1ps) and the thermalisation of the AuNP with the surrounding medium (>100ps).[47][48] Probing these dynamics allows us to distinguish the electronic AuNP response from instantaneous coherent backgrounds and/or long lived photothermal effects. This FWM method for imaging single AuNPs is completely background-free even in scattering and fluorescing cellular environments. The reflected probe and FWM field amplitudes are detected by the FWM set-up and are indicated as A^{+}_{2r} and A^{+}_{FWM} respectively (see also [48] for further details on this notation). Images that have been overlaid on the basis of the peak Pearson's coefficient may be seen in figure 5.10.

Wide field or confocal fluorescence images were acquired by Naya Giannakopoulou for correlation with FWM images. When imaging samples on multiple instruments, DIC imaging or reflected probe images were used in order to map the samples and relocate fields of view between instruments. Images acquired from different instruments were mapped using cell contours from DIC and reflection microscopy without using fiducials, therefore a small rotation and translation adjustment is needed in order to correctly overlay the images. To account for the relative rotation and translation adjustments between images, the Pearson's coefficient r_{P} was calculated as a function of relative translation (Δx,Δy) and rotation (θ) as discussed in the previous sections.

5.4.1 10nmAuNP-SA(A488)-Bi-Tf(A647)

Images of HeLa cells that have internalized the 10nmAuNP-SA(A488)-Bi-Tf(A647) construct (see Materials and Methods 3.1.1) are shown in figure 5.10. DIC and reflection images of the fixed HeLa cells used to map images between different instruments are shown, along with overlaid images between the $A_{\mathrm{FWM}^{+}}$ and the widefield fluorescence from the A647 (WF A647) and the A488 fluorophores (WF A488). From the overlaid images, it is qualitatively clear that there is no correlation between the spatial patterns observed in FWM and epi-fluorescence from the sample.

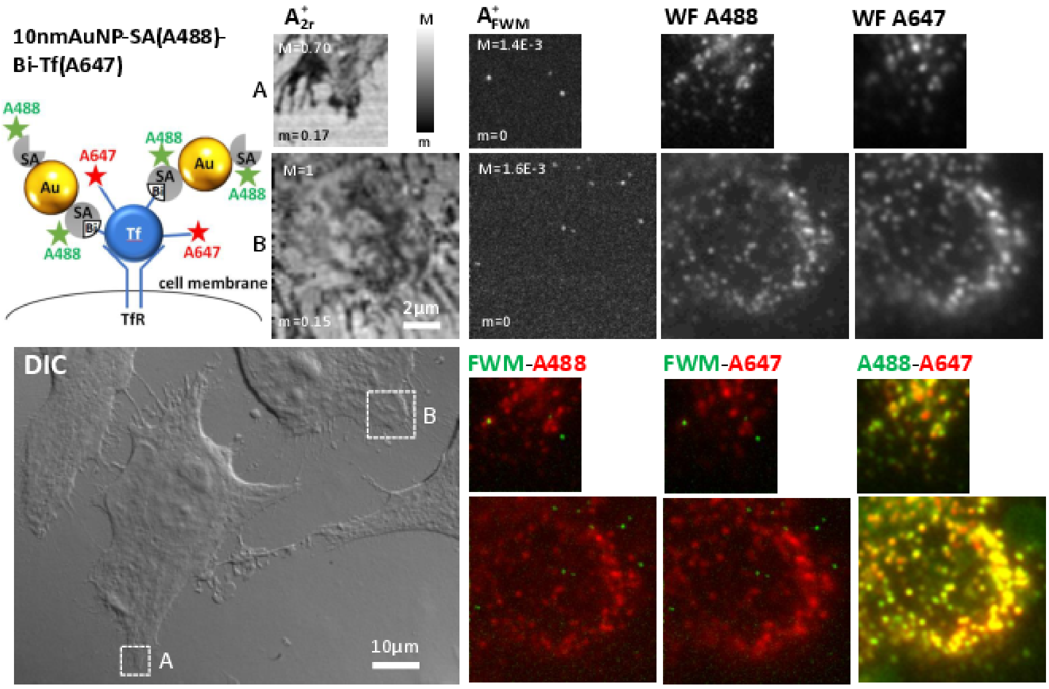

Figure 5.10: Top left: Sketch of the AuNP construct. Bottom left: Fixed HeLa cells that have internalized 10nmAuNP-SA(A488)-Bi-Tf(A647) imaged by differential interference contrast microscopy. Top Right: Reflection amplitude (A^+_{2r}), FWM amplitude (A^+_{FWM}) and wide-field fluorescence microscopy of the regions highlighted in DIC. FWM was acquired with a pump-probe delay time of 0.5 ps, pump (probe) power at the sample of 94 μW (47 μW), 5 ms-pixel dwell time in A and 3 ms in B, pixel size in plane of 38 nm and z stacks over 1 μm in 100 nm z steps. FWM is shown as a maximum amplitude projection over the z stack, while the reflection is on a single x,y plane (scanning the sample position) axially located near to the glass substrate interface. Grey scales are linear from m to M for field amplitudes, as indicated (M=1 corresponds to 7.8mV rms detected by the lock-in). Wide-field fluorescence of the Alexa488 and Alexa647 labels are shown, scaled to their maximum intensity, and indicated as WF A488 and WF A647 respectively. Overlays of FWM amplitude and wide-field fluorescence are shown color coded, as indicated. In the overlay of WF A488 (green) and WF A647 (red) images are re-scaled to highlight low intensity co-localisation (green intensity from 0.035 to 0.23 of its maximum, red intensity from 0.019 to 0.32). Reproduced with permission from [1].

Cross correlation images ($r_{\mathrm{P}}(\Delta x, \Delta y, \Delta\theta)$ for the 10nmAuNP-SA(A488)-Bi-Tf(A647) construct are shown in figure 5.11. No well defined maximum is visible near the centre of the images where the cross correlation coefficient is $r_{\mathrm{P}} < 0.05$. One would expect a well defined maximum near the centre of the cross correlation images if there were a visible colocalisation of the FWM and epi-fluorescence images.

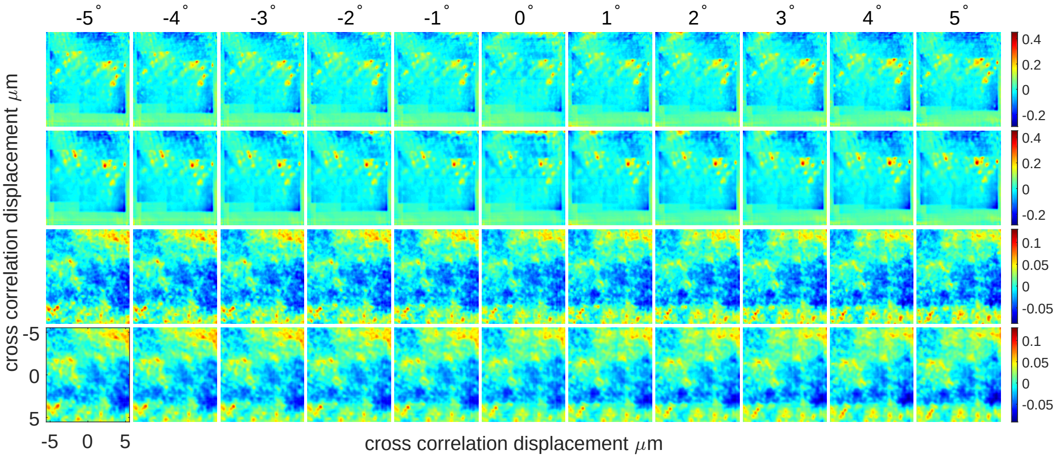

Figure 5.11: Cross correlation coefficient r_P as a function of relative translation (Δx,Δy) and rotation ($\Delta\theta$) coordinates for the results on HeLa cells loaded with the 10nmAuNP-SA(A488)-Bi-Tf(A647) construct shown in figure 5.10. First and second row refer to region A in figure 5.10 (the first row refers to the A488 fluorophore, the second row to the A647). The third and fourth row refer to region B (Third row: A488; Fourth row: A647). For each region, 11 tiles are plotted corresponding to a series of rotation angles from -5° to +5° in 1° step, as indicated.

5.4.2 15nmAuNP-PC-Tf(A488)

Images of HeLa cells that have internalized the 15nmAuNP-PC-Tf(A488) construct (see Materials and Methods 3.1.2) are shown in figure 5.12. DIC and reflection images of the fixed HeLa cells used to map images between different instruments are shown, along with overlaid images between the A_{FWM^+} and the confocal fluorescence from the A488 (Confocal A488). From the overlaid images, the correlation between the spatial patterns observed in FWM and epi-fluorescence from the sample is generally poor.

Cross correlation images ($r_\mathrm{P}(\Delta x$,Δy,$\Delta\theta$) for the 15nmAuNP-PC-Tf(A488) construct are shown in figure 5.13. A maximum near the centre of the correlation map for region B (row 2 in figure 5.13) at -4° has a value of $r_\mathrm{P} = 0.15$ which indicates some (albeit still low) spatial correlation. This result also suggests that there is an angular shift of -4° between the FWM and confocal fluorescence images, due to the fact that different instruments were used to image the sample for the different imaging modalities.

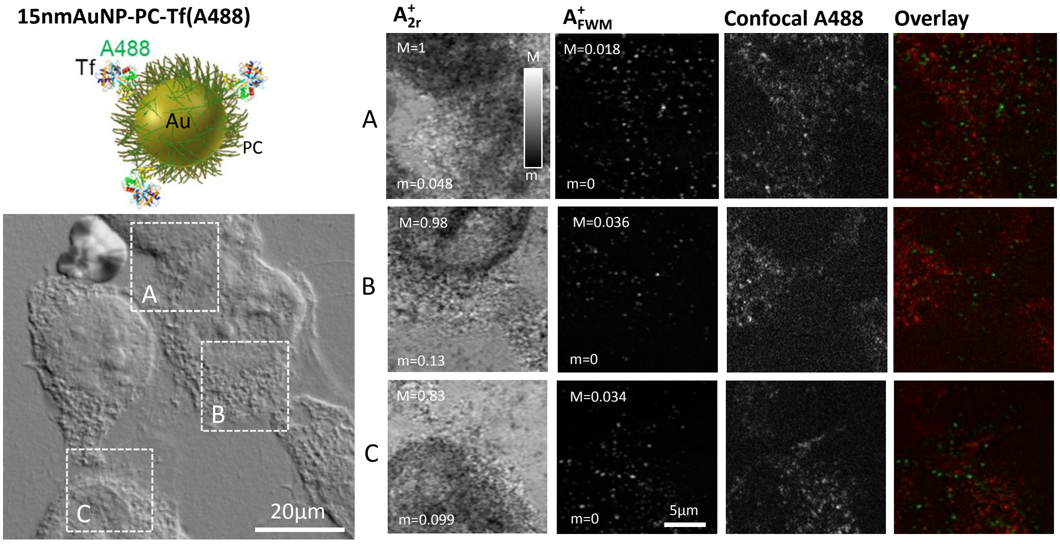

Figure 5.12: Top left: Sketch of the AuNP construct. Bottom left: Fixed HeLa cells that have internalized 15nmAuNP-PC-Tf(A488) imaged by differential interference contrast microscopy. Right: Reflection amplitude (A^+_{2r}), FWM amplitude ($A^+_{\rm FWM}$) and confocal fluorescence microscopy of the regions highlighted in DIC. FWM was acquired with a pump-probe delay time of 0.5 ps, pump (probe) power at the sample of 31 μW (16 μW), 2 ms-pixel dwell time, pixel size in plane of 94 nm and z stacks over 5 μm in 250 nm z steps. FWM, reflection, and fluorescence are shown on a single x,y plane at the glass substrate interface. Grey scales are linear from m to M for field amplitudes, as indicated (M=1 corresponds to 10mV rms detected by the lock-in). Confocal fluorescence of the Alexa488 is shown, scaled from 0 to its maximum intensity, without applying any background subtraction. Overlay: fluorescence (red), FWM amplitude (green). Reproduced with permission from [1].

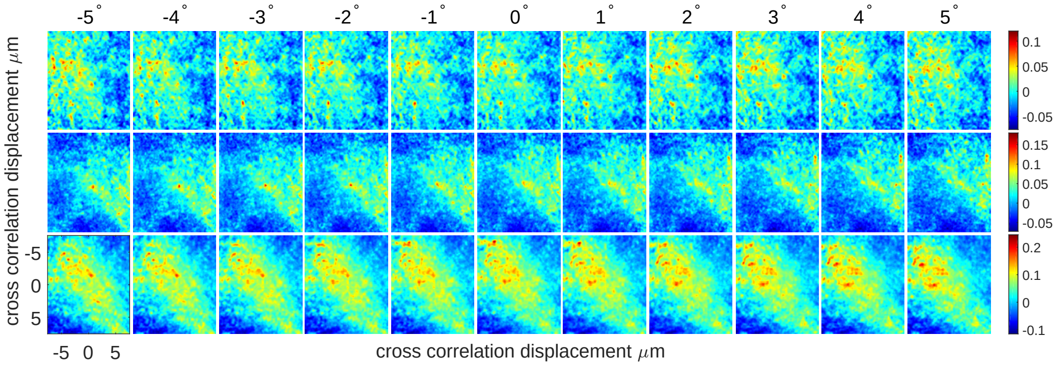

Figure 5.13: Cross correlation coefficient $r_{\rm P}$ as a function of relative translation (Δx,Δy) and rotation ($\Delta\theta$) coordinates for the results on HeLa cells loaded with the 15nmAuNP-PC-Tf(A488) construct shown in figure 5.12. Row 1 corresponds to region A in figure 5.12, Row 2 to region B, Row 3 to region C. For each region, 11 tiles are plotted corresponding to a series of rotation angles from -5° to +5° in 1° step, as indicated.

5.4.3 40nmAuNP-SA-Bi-Tf(A647)

Images of HeLa cells that have internalized the 40nmAuNP-SA-Bi-Tf(A647) construct (see Materials and Methods 3.1.3) are shown in figure 5.14. DIC and reflection images of the fixed HeLa cells used to map images between different instruments are shown, along with overlaid images between the A_{FWM^+} and the confocal fluorescence from the A647 (Confocal A647). Again, from the overlaid images, it is qualitatively clear that there is no correlation between the spatial patterns observed in FWM and epi-fluorescence from the sample.

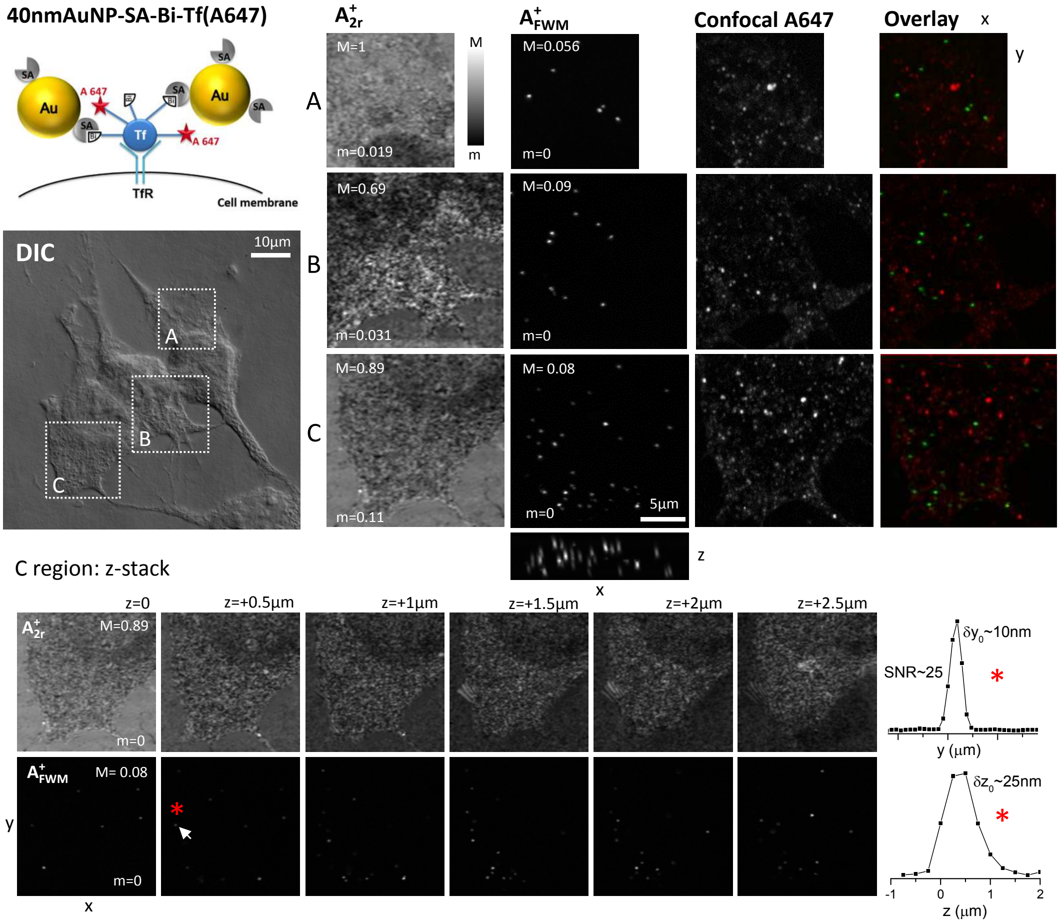
40nmAuNP-SA-Bi-Tf(A647)
Au
SA
A 647
Tf
TfR
Cell membrane
DIC
10μm
A^+_{2r}
A^+_{FWM}
Confocal A647
Overlay
x
y
M
m
M=1
m=0.019
M=0.056
m=0
M=0.69
m=0.031
M=0.09
m=0
M=0.89
m=0.11
M= 0.08
m=0
5μm
z
A
B
C
C region: z-stack
z=0
z=+0.5μm
z=+1μm
z=+1.5μm
z=+2μm
z=+2.5μm
M=0.89
m=0
M= 0.08
m=0
δy₀~10nm
SNR~25
y (μm)
δz₀~25nm
z (μm)
-1
0
1
2

Figure 5.14: Top left: Sketch of the AuNP construct. Center left: Fixed HeLa cells that have internalized 40nmAuNP-SA-Bi-Tf(A647) imaged by differential interference contrast microscopy. Top Right: Reflection amplitude (A^+_{2r}), FWM amplitude (A^+_{FWM}) and confocal fluorescence microscopy of the regions highlighted in DIC. FWM was acquired with a pump-probe delay time of 0.5 ps, pump (probe) power at the sample of 30 μW (15 μW), 2 ms-pixel dwell time, pixel size in plane of 95 nm and z stacks over 5 μm in 250 nm z steps. FWM is shown as a maximum amplitude projection in the x,y plane over the z stack (and in the x,z plane for region C). The reflection is on a single x,y plane (scanning the sample position) axially located near to the glass substrate interface. Grey scales are linear from m to M for field amplitudes, as indicated (M=1 corresponds to 8.9mV rms detected by the lock-in). Confocal fluorescence of the Alexa647 label is a maximum intensity projection over a 6.9 μm z-stack in 250 nm z steps. Overlay: fluorescence (red), FWM amplitude (green). Bottom: series of reflection and FWM images for region C at different z planes, as indicated. For the AuNP indicated by the red asterisk and white arrow, 1D cuts along y and z are shown on the right. Reproduced with permission from [1].

Cross correlation images ($r_{\mathrm{P}}(\Delta x,\Delta y,\Delta\theta)$ for the 40nmAuNP-SA-Bi-Tf(A647) construct are shown in figure 5.15. No well defined maximum is visible near the centre of the images where the cross correlation coefficient is $r_{\mathrm{P}} < 0.05$. This result quantitatively confirms what is qualitatively visible in 5.15, that there is no correlation between the spatial patterns observed in FWM and epi-fluorescence from the sample.

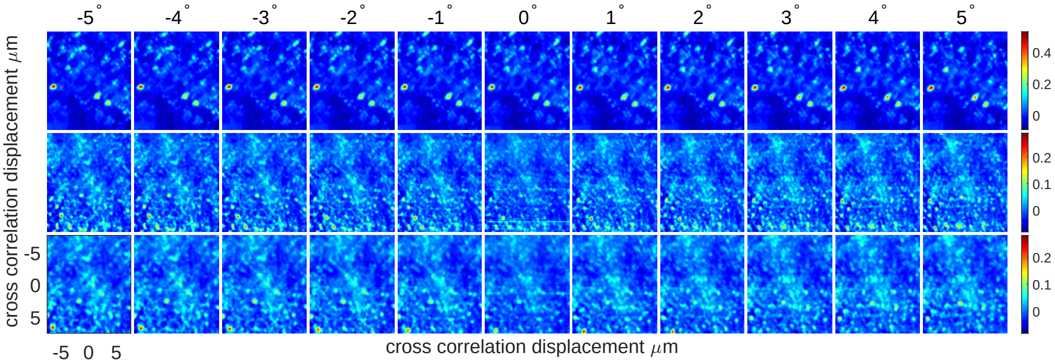

Figure 5.15: Cross correlation coefficient r_{P} as a function of relative translation (Δx,Δy) and rotation ($\Delta\theta$) coordinates for the results on HeLa cells loaded with the 40nmAuNP-SA-Bi-Tf(A647) construct shown in figure 5.14. Row 1 corresponds to region A, Row 2 to region B, Row 3 to region C in figure 5.14. For each region, 11 tiles are plotted corresponding to a series of rotation angles from -5° to +5° in 1° step, as indicated.

Chapter 6

Nanoparticle Heating

As discussed in Chapter 1, through the use of an experimental setup reported in the recent literature comprising a AuNP surrounded by a lipid bilayer, [2] it is possible to measure the surface temperature of AuNPs (see figure 6.1).

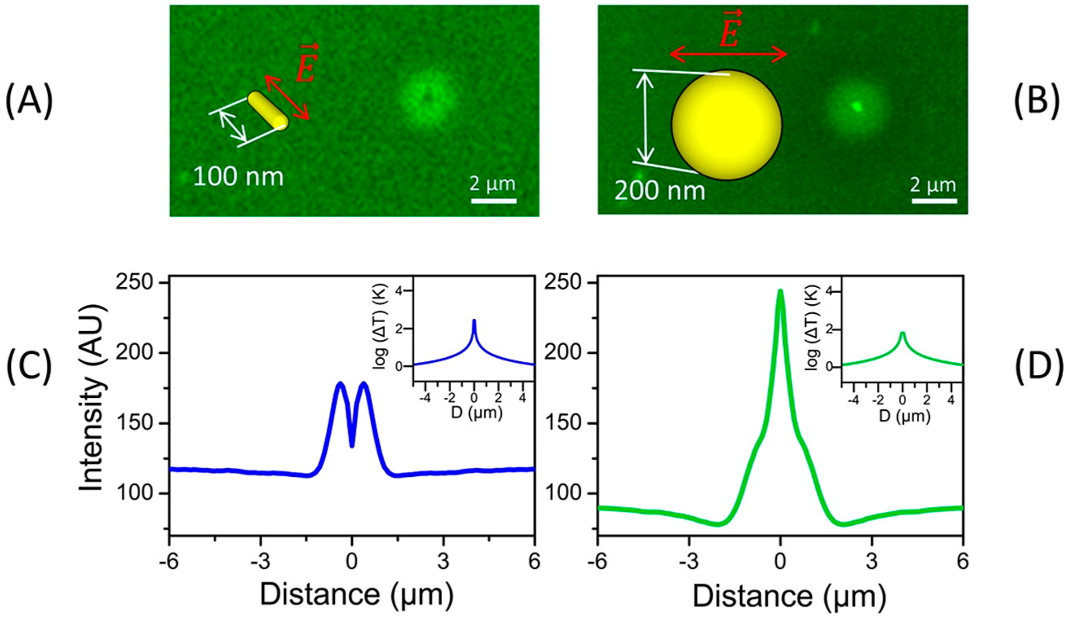

Figure 6.1: Quantification of melting fingerprint and temperature profile. (A,B) Confocal images of fluorophores partitioning in fluid regions around an irradiated gold nanorod (of nominal size 20 nm×100 nm) (A) or a gold nanosphere (nominal diameter = 200 nm) (B) under identical illumination conditions (1.8×10^{10}W/m^2). (C,D) Intensities of fluorophores as a function of distance from the center of the irradiated nanoparticles, (C) is for the rod shown in (A), (D) is for the sphere shown in (B). Insets show the logarithm of the temperature increase as function of distance from the center of the irradiated nanoparticles. Reproduced with permission from [2].

The particle is resonantly irradiated, and the resulting temperature increase in its vicinity induces a phase transition at a distance away from the AuNP. The phase transition of the lipid bilayer is well characterised, and a temperature profile around an irradiated AuNP can be modelled [72], using the location of the phase boundary between the fluid and solid gel phase of the lipid bilayer and literature values for the relevant physical parameters. However, the precise position of the phase boundary is not clearly observed when imaging using fluorescence labels, as the fluorescence labels diffuse into the fluid phase, leaving a depleted region around the liquid phase region which gives an uncertainty as to where the phase boundary exists. Moreover, fluorophores may change the lipid phase transition temperature. Conversely, label-free qDIC may produce a reliable phase contrast which precisely shows the location of the phase boundary, and can use well characterised unlabelled lipids. In this Chapter, the experimental procedure developed in order to perform the experiment reported in [2] with increased accuracy using an in-house developed qDIC method is discussed.

6.1 Experimental results

A description of the setup used for these experiments is given in Chapter 3.34. Briefly a CW laser at 532nm wavelength and controlled power, was used to induce a photothermal heating onto individual 50nm diameter AuNPs deposited onto a glass coverslip and surrounded by a lipid bilayer. As a first test we used a fluorescently labelled lipid ($DC_{15}PC$:Atto425-DOPE in a 99.9:0.1 ratio), for direct comparison with the results in [2]. The alignment of the laser beam for the photothermal heating of AuNPs was conducted in a manner described in section 3.5.4. Before imaging, microscope objective and condenser heating units were used to set to a temperature of 28.5°C, close to, but not above the phase transition temperature of the lipid. To image the lipid bilayer sample, a 1.4NA 100× objective was used with the 1.5× tube lens. An LED light source (Thorlabs) with a central wavelength of 530nm (with a current of 80mA) was used to acquire DIC images and locate AuNPs in transmission as the 50nm AuNPs strongly absorb wavelengths around 530nm. Extinction images were then acquired to verify that these objects are 50nm AuNPs, an example of which is shown in figure 6.2 **A**. To verify that the lipid bilayer was fluorescing, a fluorescence image was acquired with an exposure time of 500ms and 0 frame averages, again using the Thorlabs LED light source at the 405nm central wavelength setting at (500mA), and with the use of the GFP filter cube for detection together with the Thorlabs 450nm filter in the excitation. This image is shown in figure 6.2 **B**. For DIC imaging, a polariser angle of 15° was used, and images within a time course were acquired with an exposure of 50ms with 32 frame averaging. For the I_+ and I_- images, an exposure time of 100ms and 128 frame averaging were used. The differential phase (δ) and phase image (φ) of the lipid bilayer surrounding the nanoparticle are shown in figure 6.2 **C** and **D** respectively. A nominal power of 40mW was used for the photothermal heating of the AuNP with the 532nm laser source. Using a 10× objective, the power measured transmitted through the optics with a nominal power of 100mW was 8mW. The AuNP was irradiated with approximately 1.6×10^{8}W/m^2

for the nominal 40mW setting.

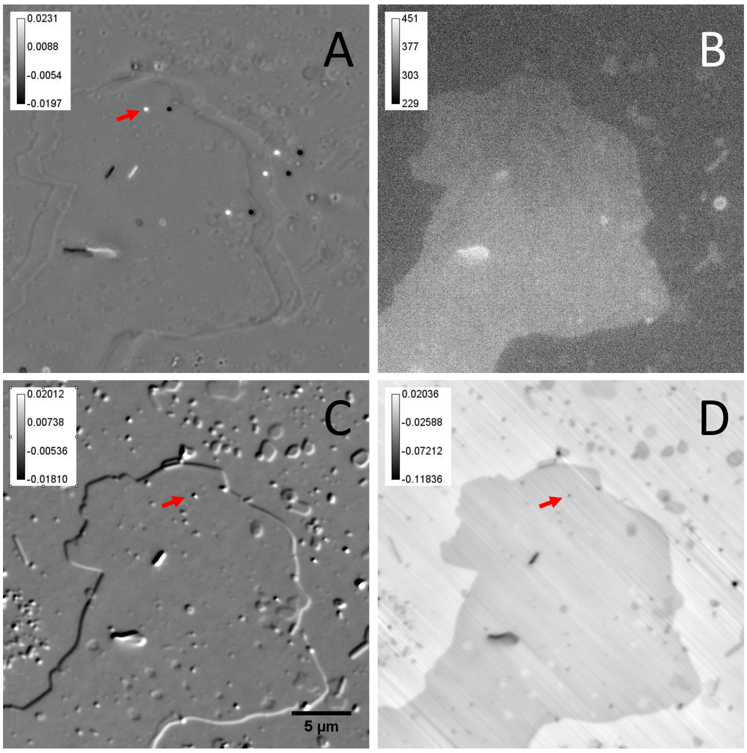

Figure 6.2: Nanoparticle heating experiment. **A** 50nm AuNPs are found in transmission, these nanoparticles are shown in an extinction image. **B** Sample imaged in transmission fluorescence. **C** Differential phase (δ) image **D** Phase image of sample. The heated AuNP is indicated where possible.

Upon carrying out the nanoparticle heating measurements, it was noticed that the expected phase profile of a solid to liquid ordered phase transition was not observed around the AuNP. Phase transitions have previously been observed with the use of the qDIC method detailed in this thesis, typically the thickness change in lipid bilayers when transitioning from the solid ordered phase to liquid ordered phase are of the order of 1nm.[88][89] Figure 6.3 shows the effect of increasing irradiation powers on the AuNP position and surrounding bilayer. The AuNP is clearly visible for nominal laser powers of 10mW and 20mW using time course DIC, which suggests that the AuNP had moved during irradiation. This would suggest the AuNP was weakly bound to the glass substrate, which would impact the accuracy of results gained for its surface heating. The model used requires that the AuNP is stationary when calculating this quantity using the model described in section 2.4 , When a power of 40mW was used a blister effect occured, the evolution of which may be seen in figure 6.4. To create the time course images in 6.3, images acquired 8s apart were used to show the effect of using increasing nominal laser powers for heating purposes. The first DIC image (n=3, the third image in the time course) was acquired before the laser was switched on, the second DIC image used (n=8) was acquired when the laser was switched on. The time course images seen in figure 6.3 were prepared in the same manner as shown in section 4.8.

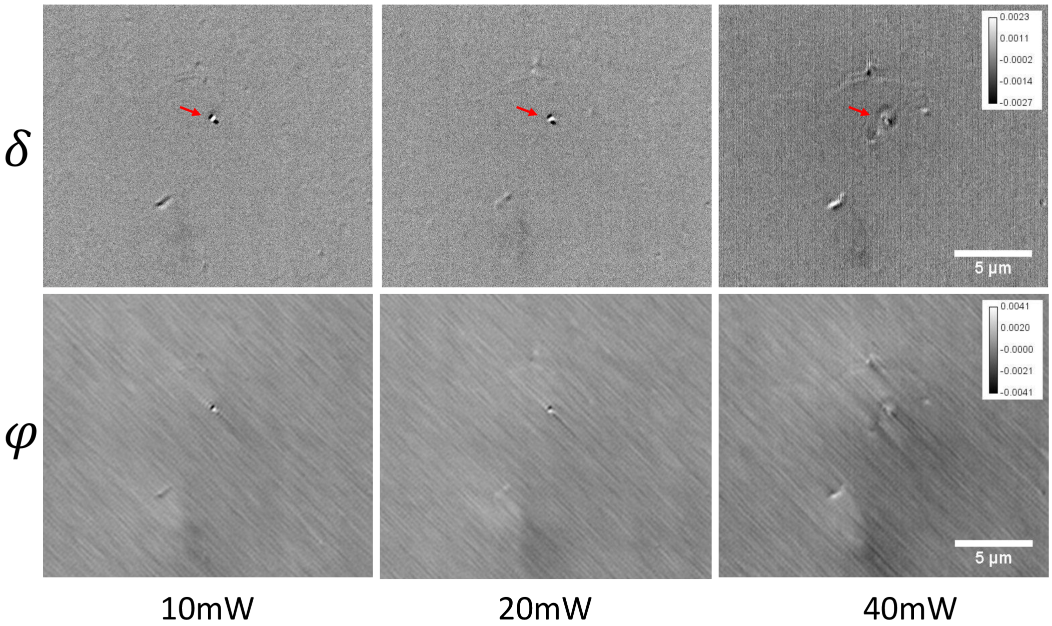
δ
φ
0.0023
0.0011
-0.0002
-0.0014
-0.0027
0.0041
0.0020
-0.0000
-0.0021
-0.0041
5 μm
5 μm
10mW
20mW
40mW

Figure 6.3: Time course DIC performed on the AuNP (indicated with red arrows) with increasing laser powers. The slight movement of the AuNP is visible for powers of 10mW and 20mW, though no blister effect is observed. For a power of 40mW, a blister is formed in the vicinity of the AuNP.

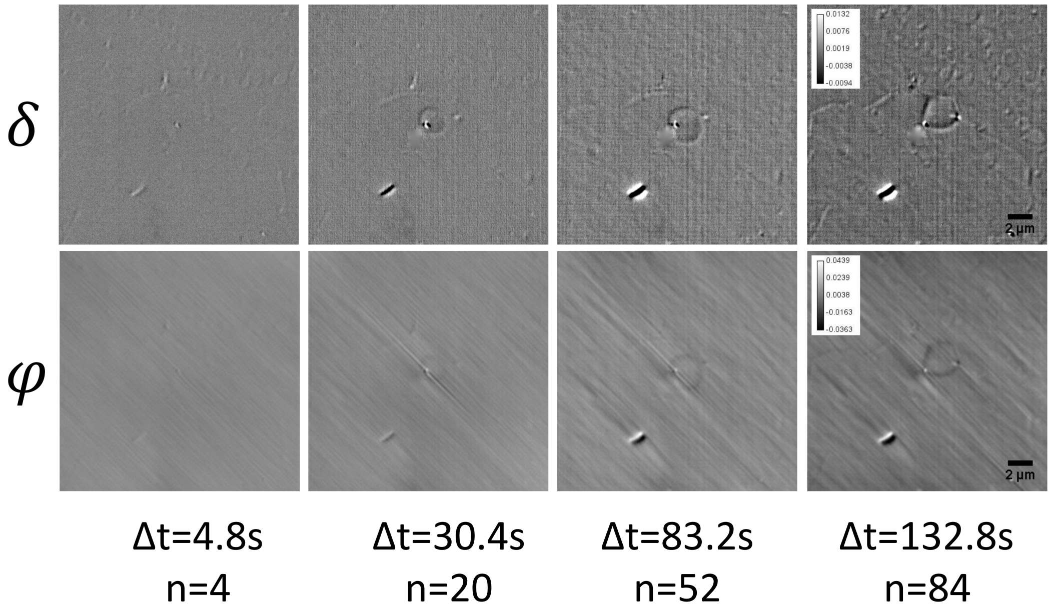
δ
φ
0.0132
0.0076
0.0019
-0.0038
-0.0094
0.0439
0.0239
0.0038
-0.0163
-0.0363
2 μm
2 μm
Δt=4.8s
n=4
Δt=30.4s
n=20
Δt=83.2s
n=52
Δt=132.8s
n=84

Figure 6.4: Blister effect observed during NP heating experiment. Time-course DIC was used in an attempt to measure the phase transition around a photothermally heated AuNP. Images were registered to account for the drift that occurs during the time course measurement. Differential phase (δ) and phase contrast (φ) between the first frame in the time course (n=1) and n (as indicated below the images) are shown. The time difference between acquiring images Δt is also indicated.

A further example of time course measurements is shown in figure 6.4, in this case, the laser was switched on at t=6.4s. The equation for the contrast images to show the evolution of the hypothesised blister formation was as follows.

$$I_{cn}(\mathbf{r}) = \frac{2(I_n - I_1)}{I_+ + I_-} \tag{6.1}$$

The results in figure 6.4 suggests that a blister is forming around the heated AuNP, with the lipid bilayer detaching from the coverslip in the ring-shaped region surrounding the NP (see sketch in figure 6.6 **B**). The observed ring-shaped phase change in figure 6.4 carries an information about the amount of lipid which has lifted from the surface and is bent, causing an apparent thickness change. To determine the approximate length of this lifted layer (the birefringence within the lipid bilayer is not accounted for in this measurement), we analyse the data as follows. A line plot of the edge of the blister phase change is shown in figure 6.5, and is fitted using the following equation (using the curve fitting tool in MATLAB) .

$$a\mathrm{sech}\left(\frac{(\mathrm{x}-\mathrm{b})}{\mathrm{c}}\right) + \mathrm{dx} + \mathrm{e} \tag{6.2}$$

As we are not concerned with the phase contribution originating from the linear background we can ignore the parameters d and e, and calculate the integral of this line plot which is equal to πac. This value has units of radians×pixels, and provides the combined volumetric information of the phase introduced by the bent bilayer, which can be approximated as a bent length times the bilayer thickness. The latter can be also quantified in qDIC, as shown in figure 6.5 **B**. As a result, we deduce a length of the bent blister of 25.67nm after approximately 128s of heating. The fitted line plots are seen in figure 6.5.

Notably, the results obtained so far did not provide the sought information about the AuNP surface temperature. Instead, they highlighted a different behaviour, which we hypothesise as the formation of a blister. A close inspection of the sample preparation used in [2] indicates that a possible reason is the use of different lipids. Specifically in [2] the lipid bilayer incorporated a positively charged lipid. The incorporation of positive charges has been shown to reduce or eliminate the lateral expansion of the bilayer over the phase transition, and in turn prevent blister formation.[91]

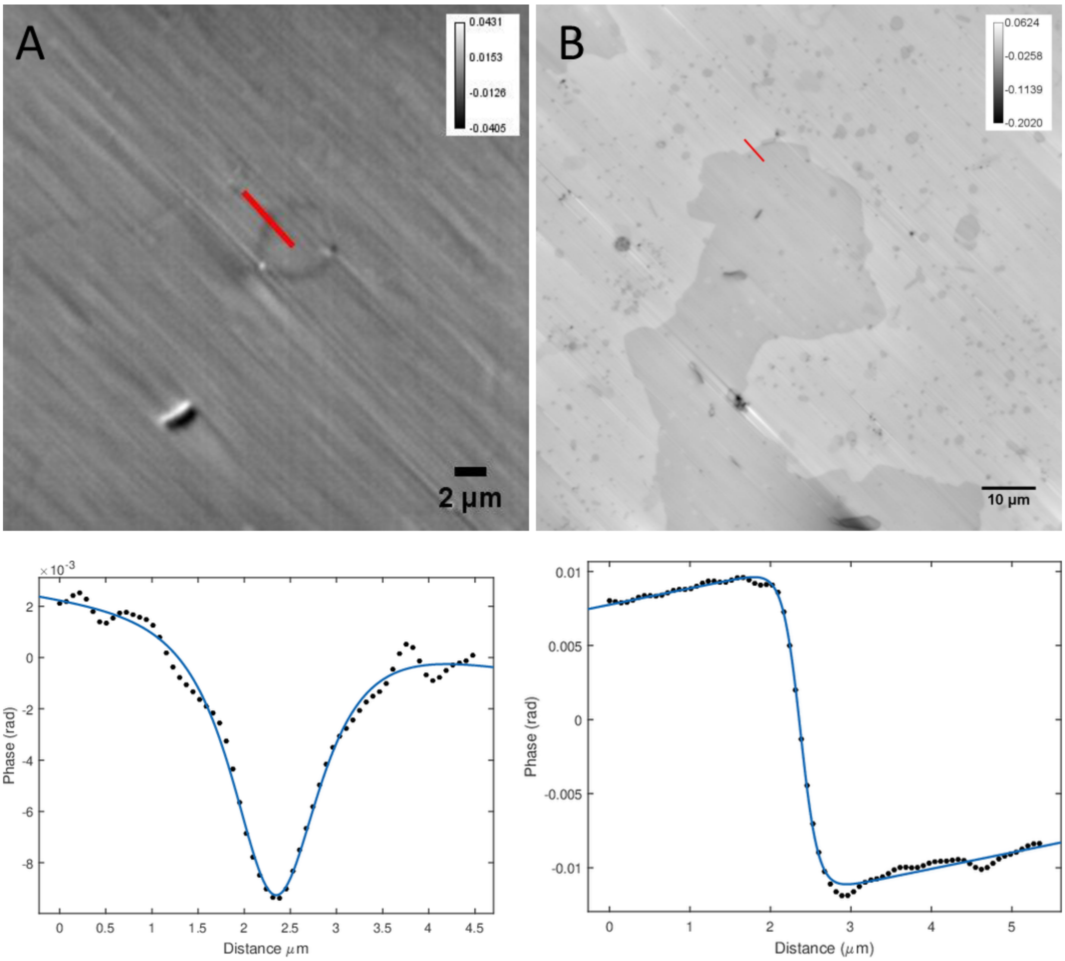

Figure 6.5: **A** Time course phase image of blister after 128s **B** A phase image of the lipid bilayer surrounding the AuNP, below left: a fitted line plot from the edge of the blister, below right: a fitted line plot at the edge of the lipid bilayer.

No phase dynamics typical of a phase transition were observed when imaging the fluorescently labelled lipid bilayer using epi-fluorescence imaging. During laser heating, a significant fluorescence background from the glass surface was observed, which dominated any signal from the fluorescently labelled lipid bilayer. In an attempt to reduce this effect, a notch filter was used to block wavelengths around 532nm, a Semrock 417/60nm Brightline single-band bandpass filter and a Thorlabs FB450-40 band pass filter were used in order to attempt to filter out the fluorescence background from the glass whilst passing the fluorescence signal from the fluorescently labelled lipid bilayer. For future experiments, the microscope setup has been modified in order to be able to insert multiple additional bandpass filters to further minimise the fluorescence background.

In the experiment reported in [2], it was shown that the location of a phase boundary within a lipid bilayer at a distance away from a photothermally heated AuNP was visible in fluorescence. In principle, this experiment could be replicated with the use of qDIC, as phase transitions have previously been detected using this

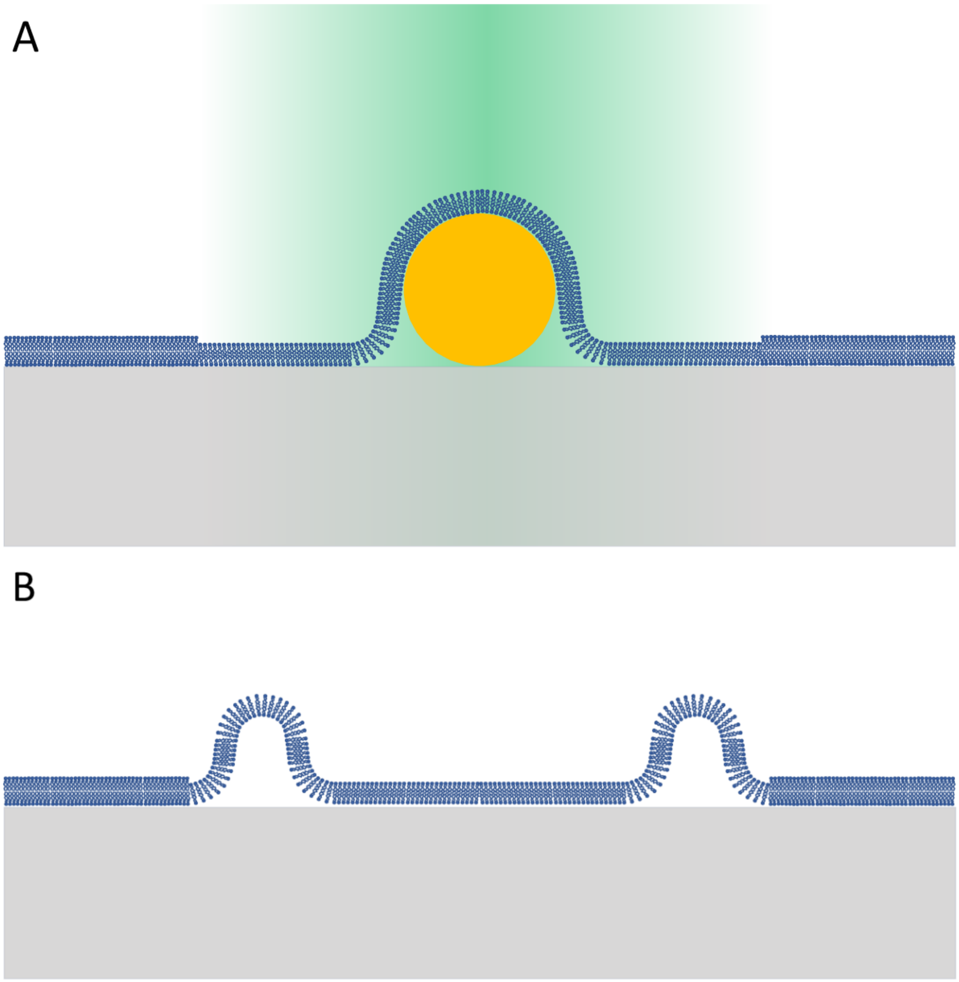

Figure 6.6: Geometry of the AuNP photothermal heating experiment. Upon irradiation from a 532nm laser, the lipid bilayer in the vicinity of the 50nm AuNP undergoes a phase trasition. This phase transition can be resolved and imaged in DIC. Measuring the location of the phase transition relative to the centre of the AuNP can give a quantitative measure for the surface heating of the particle. **A**: sketch of the lipid bilayer on top of the AuNP prior to heating. **B**: sketch of the "blister" and lifting of lipid bilayer after heating (the AuNP is omitted in **B** for simplicity).

imaging modality. [89][88] It would also be possible to conduct a similar experiment described in [2] in epi-fluorescence (as was attempted) if the background fluorescence can be filtered sufficiently.

Chapter 7

Conclusions and Outlook

In summary, this thesis covers a series of experiments and data analysis developments which I have performed, in order to address a number of challenges in relation to imaging quantitatively bio-nanostructures. As stated in Chapter 1, the work in this thesis was motivated by three main questions, namely: i) how far can quantitative DIC microscopy be expanded and improved to accurately measure the thickness of single lipid bilayers, ii) do AuNP-fluorophore conjugates provide a stable and reliable dual probe for correlative imaging studies, iii) can DIC offer a label-free quantitative method to accurately measure the surface temperature of a AuNP.

As part of this work, in relation to the first question, a software has been developed which extracts optical phase information from a specimen imaged with differential interference contrast. Using a simple workflow detailed within this thesis one can extract a differential phase image from images acquired using a conventional De Sénarmont DIC setup. A Wiener filtering approach is used to integrate the differential phase contrast image, to obtain an optical phase image of the specimen. The quality of Wiener filtered images is improved through the use of an apodization process to produces a two dimensional window around the differential phase image similar to the Hann window often used in one dimensional Fast Fourier Transform algorithm. This method of integration (of the order of 20-30s) provides a fast tool by which one can obtain phase images of specimens. Additionally, an energy minimisation routine further improves the quality of the retrieved phase images. From results presented in this thesis, it has been shown that one can perform the energy minimisation algorithm on multiple images in parallel with varied parameters. Images reach a converged status after approximately 10^7 iterations. To perform 10^7 iterations on graphics processing units (GPUs), it takes approximately 72 hours. To expand on the work presented in this thesis, an extension to the energy minimisation algorithm is proposed, whereby the dynamic changing of minimisation parameters would result in a (possibly $10\times$) faster convergence relative to a base truth image.

In relation to the second question mentioned above, following the acquisition of a series of confocal fluorescence and FWM amplitude images from bioconjugated fluorescently labelled AuNPs in Naya Giannakopoulou's thesis [1], a cross-correlation algorithm has been developed to quantify the Pearson's coefficient for lateral shifts between these images. To accommodate for any angular discrepancies between these images, a further algorithm was developed in order to rotate images relative to one another so that cross the images may be cross correlated. Pearson's coefficients from cross correlated images showed a lack of colocalisation between FWM amplitude and fluorescence images of HeLa cells loaded with AuNP-fluorophore constructs, generally resulting in values $r_{\mathrm{P}} < 0.05$ (apart from one instance where $r_{\mathrm{P}} = 0.15$) which confirms what was qualitatively reported in [1]. A direct study of the correlation between extinction and epi-fluorescence images of AuNP-fluorophore constructs prepared (washed) as per manufacturer specification and deposited onto a glass surface was subsequently performed. The cross correlation of extinction and epi-fluorescence images from a 10nm AuNP-fluorophore construct (10nmAuNP-SA(A-488)) gave Pearson's coefficients $r_{\mathrm{P}} < 0.06$ for 1× and 3× washes, clearly indicating that the supposedly attached fluorophores are not reliable reporters of the NP location. Conversely, 20nm diameter AuNPs covalently bound to fluorescently labelled antibodies revealed a good degree of colocalisation with the fluorophore ($r_{\mathrm{P}} = 0.476$) after 3× washes.

Generally these results indicated that care should be taken when using AuNP-fluorophore conjugates, and that relying solely on the fluorescence readout might lead to misleading/incorrect conclusions about the AuNP location.

Finally, in relation to the third question motivating this thesis work, a AuNP heating set-up was developed, using the qDIC imaging method outlined in this thesis. Briefly, a lipid bilayer was overlaid above a AuNP bound to a coverslip, and was photothermally heated at the localised surface plasmon resonance. The heat which dissipates from the AuNP induces a phase transition in the lipid bilayer in its vicinity. By locating the phase boundary in the lipid bilayer, one can quantitatively measure the surface heating of the AuNP. In principle, the precise location of a phase boundary in a lipid bilayer is observable in qDIC. However, the dynamics observed through acquiring a qDIC time course did not resemble the behaviour previously observed in fluorescence measurements in [2]. In particular, it is hypothesized that a blister effect occurred during resonant photothermal heating of a 50nm AuNP at the LSPR, lifting the lipid bilayer and generating an apparent thickness change. In a future experiment, a positively charged lipid species in [2] will be used to minimise bilayer expansion to avoid the formation of a blister.

Appendix A

qDIC Theory: Jones matrix formulation

The Jones Matrix formulation for Differential Interference Contrast in a configuration that does not involve using a variable retarder is described in this section. The field from the lamp is split into two polarised fields as they traverse the polariser:

$$E_{\text{polarised}} = E \begin{pmatrix} \cos\alpha \\ \sin\alpha \end{pmatrix} = \frac{E_0}{\sqrt{2}} \begin{pmatrix} 1 \\ 1 \end{pmatrix} \tag{A.1}$$

where $\alpha = \pi/4$. The two polarised beams are sheared by the Wollason prism, and are separated by a shear distance Δ. Upon traversing a specimen each polarisation acquires a phase ρ which is position dependent, this results in an optical path difference between the beams that are recombined upon traversing a second Wollaston prism. The specimen matrix is formulated as the following

$$M_{\text{specimen}} = \begin{pmatrix} e^{i\rho(x-\frac{\Delta}{2})} & 0 \\ 0 & e^{i\rho(x+\frac{\Delta}{2})} \end{pmatrix} \tag{A.2}$$

Once the beams are recombined they traverse an analyser (a polariser with angle α').

$$M_{\text{analyser}} = \begin{pmatrix} 1 & 0 \\ 0 & 0 \end{pmatrix} \begin{pmatrix} \cos\alpha' & \sin\alpha' \\ -\sin\alpha' & \cos\alpha' \end{pmatrix} = \begin{pmatrix} \cos\alpha' & \sin\alpha' \\ 0 & 0 \end{pmatrix} \tag{A.3}$$

The interaction of the sheared beams with the analyser is thus described by the follwing linear operation to obtain the output field $E_{\text{output}} = M_{\text{analyser}} M_{\text{specimen}} E_{\text{polarised}}$:

$$E_{\text{output}} = \begin{pmatrix} \cos\alpha' & \sin\alpha' \\ 0 & 0 \end{pmatrix} \begin{pmatrix} e^{i\rho(x-\frac{\Delta}{2})} & 0 \\ 0 & e^{i\rho(x+\frac{\Delta}{2})} \end{pmatrix} \frac{E_0}{\sqrt{2}} \begin{pmatrix} 1 \\ 1 \end{pmatrix} \tag{A.4}$$

$\alpha' = -\pi/4$ which gives the following expression for the output in plane field $E_{||}$

$$E_{||} = E_0 \frac{1}{2} (e^{i\rho(x-\frac{\Delta}{2})} - e^{i\rho(x+\frac{\Delta}{2})}) \tag{A.5}$$

Using the first terms of the Taylor expansion we can obtain an expression for $\rho(x)$ at point x_0

$$\rho(x) \approx \rho(x_0) + \frac{\partial\rho}{\partial x}(x - x_0) \tag{A.6}$$

Equation A.5 can be recast as the following:

$$E_{||} = \frac{E_0}{2} e^{i\rho(x)} \Big(e^{i\frac{\partial\rho}{\partial x}(-\frac{\Delta}{2}))} - e^{i\frac{\partial\rho}{\partial x}(\frac{\Delta}{2}))} \Big) \tag{A.7}$$

Using the trigonometric identity: $\sin(\theta) = \frac{e^{i\theta} - e^{-i\theta}}{2i}$, Equation A.7 can be expressed as the following:

$$E_{||} = \frac{E_0}{2} e^{i\rho(x)} 2i \sin\Big(\frac{\partial\rho}{\partial x}\frac{\Delta}{2}\Big) = iE_0 e^{i\rho(x)} \sin\Big(\frac{\partial\rho}{\partial x}\frac{\Delta}{2}\Big) \tag{A.8}$$

which yields an intensity $I \propto E_0^2 \sin^2\Big(\frac{\partial\rho}{\partial x}\frac{\Delta}{2}\Big)$, and given that $\frac{\partial\rho}{\partial x}\frac{\Delta}{2} << 1$, $I \propto {E_0}^2 \Big(\frac{\partial\rho}{\partial x}\frac{\Delta}{2}\Big)^2$

A.1 Variable Retarder

When a variable retarder is introduced as is the case in the De Senarmont configuration for DIC, an additional phase bias ρ_0 is introduced which can can be used in order to increase the differential phase contrast

$$M_{\text{specimen}} = \begin{pmatrix} e^{i\rho(x-\frac{\Delta}{2})} & 0 \\ 0 & e^{i\rho(x+\frac{\Delta}{2})+i\rho_0} \end{pmatrix} \tag{A.9}$$

The in plane field $E_{||}$ becomes the following once the beams are recombines by the Wollaston prism and traverse the analyser:

$$E_{||} = \frac{E_0}{2} \Big(e^{i\rho(x-\frac{\Delta}{2})} - e^{i\rho(x+\frac{\Delta}{2})+i\rho_0} \Big) \tag{A.10}$$

Once more we can use the first terms of the Taylor expansion of $\rho(x)$ with an additional ρ_0 term in order to recast equation A.10:

$$\rho(x) - \frac{\rho_0}{2} \approx \rho(x_0) + \frac{\partial\rho}{\partial x}(x - x_0) - \frac{\rho_0}{2} = \rho(x_0) + \frac{\partial\rho}{\partial x}\Big(\pm\frac{\Delta}{2}\Big) \pm \frac{\rho_0}{2} \tag{A.11}$$

recasting equation A.10

$$E_{||} = \frac{E_0}{2} e^{i\frac{\rho_0}{2}} e^{i\rho(x)} \left(e^{i(\frac{\partial\rho}{\partial x}(-\frac{\Delta}{2})-\frac{\rho_0}{2}} - e^{i(\frac{\partial\rho}{\partial x}(\frac{\Delta}{2})+\frac{\rho_0}{2}} \right) \tag{A.12}$$

and again using the trigonometric identity $\sin(\theta) = \frac{e^{i\theta}-e^{-i\theta}}{2i}$ yields

$$E_{||} = \frac{E_0}{2} e^{i\frac{\rho_0}{2}} e^{i\rho(x)} (-2i) \sin\left(\frac{\partial\rho}{\partial x}\left(\frac{\Delta}{2}\right) + \frac{\rho_0}{2} \right) \tag{A.13}$$

which gives an intensity $I \propto E_0^2 \sin^2\left(\frac{\partial\rho}{\partial x}\left(\frac{\Delta}{2}\right) + \frac{\rho_0}{2}\right)$. Using the trigonometric identity

$$\cos(\alpha + \beta) = \cos\alpha\cos\beta - \sin\alpha\sin\beta \tag{A.14}$$

We find an intensity I:

$$I \propto \frac{E_0^2}{2}\left(1 - \cos\left(\frac{\partial\rho}{\partial x}\Delta + \rho_0\right)\right) \tag{A.15}$$

Appendix B

Image rotation code

```
function [L,Q]=central_port_2(pp,C,R)
%C is the image that is to be rotated
%R is the non-rotated image
%pp is the angle of rotation
%L is the central portion of the outputted non-rotated image
%Q is the central portion of the rotated image
c=size(C);
CC=ones(c);

F=imrotate(C,pp);
FF=imrotate(CC,pp);
f=size(F);
%% Mapping the rotated image in binary
B=FF~=0;
kk=500;
%% Finding the dimensions of and extracting the central portion of the...
      rotated image and the non rotated image
for nn=1:kk
    b_top=B((1+nn-1),1+(nn-1):(end-nn+1));
    [min_b_top, b_top_imin] = min(b_top(:));
    b_bottom=B((end-nn+1),(1+nn-1):(end-nn+1));
    [min_b_bottom, b_bottom_imin] = min(b_bottom(:));
    b_left=B((1+nn-1):(end-nn+1),(1+nn-1));
    [min_b_left, b_left_imin] = min(b_left(:));
    b_right=B((1+nn-1):(end-nn+1),(end-nn+1));
    [min_b_right, b_right_imin] = min(b_right(:));
    if min_b_bottom==0 || min_b_left==0 || min_b_right==0 || min_b_top...
        ==0
        continue
    else
        r=(1+nn-1);
        j=(f(1)-nn+1);
        q=((f(2)-nn+1));
        Q=F(r:j,r:q);
        break
    end
```

```
end

q_s=size(Q);

 if mod(q_s(1),2)~=0
     Q=Q(2:end,:);
end
 if mod(q_s(2),2)~=0
     Q=Q(:,2:end);
end
q_s=size(Q);

%% Extracting the central portion of the non-rotated image
K=R(1:end,1:end);
k_s=size(K);

 if q_s(1)<=k_s(1) && q_s(2)<=k_s(2)
     K=R((((k_s(1)-q_s(1))/2)+1:end-((k_s(1)-q_s(1))/2)),((k_s(2)-q_s...
         (2))/2)+1:end-((k_s(2)-q_s(2))/2));
 else if q_s(1)>=k_s(1) && q_s(2)>=k_s(2)
         K=R((((q_s(1)-k_s(1))/2)+1:end-((q_s(1)-k_s(1))/2)),((q_s(2)-...
             k_s(2))/2)+1:end-((q_s(2)-k_s(2))/2));
     end
end

K1=K;
L=K1;

end
```

Appendix C

Normalised cross-correlation algorithm (Pearson's coefficient)

```
function [A,A1,B_norm,C_norm]=corr_norm_3(B,C,cent_rang,whole)
%B and C are the inputted images to be correlated
%cent_rang is the variable which prompts the function to only ...
    calculate the
%cross correlation between B and C in a user-defined range of shifts
%whole is the logical value which prompts the function to calculate ...
    the
%cross correlation for all shifts

b=size(B);
c=size(C);
A=zeros((b(1)+c(1)-1),(b(2)+c(2)-1));
a=size(A);

%% Normalising input images
C=(C-mean(C(:)))/(sqrt(mean(mean((C-mean(C(:))).^2))));
B=(B-mean(B(:)))/(sqrt(mean(mean((B-mean(B(:))).^2))));

%% Defining a range of shifts based on cent_rang
r=ceil((a(1)-c(1))/2);
l=ceil((a(1)-c(1))/2)+c(1);
rl_diff=floor((l-r)/2);
rr=r+rl_diff-cent_rang;
ll=r+rl_diff+cent_rang;
m=ll-rr;

h=ceil((a(2)-c(2))/2);
g=ceil((a(2)-c(2))/2)+c(2);
hg_diff=floor((g-h)/2);
hh=h+hg_diff-cent_rang;
gg=h+hg_diff+cent_rang;

if whole
```

```
    rr=1;
    ll=a(1);
    hh=1;
    gg=a(2);
end
%% Calculating the Pearson's coefficient for all shifts / or a user ...
    defined range of shifts

for yy=rr:ll
    for xx=hh:gg
        if yy<=b(1)&& xx<=b(2)
            T=(B((end+1)-yy:end,(end+1)-xx:end)==0);
            J=sum(sum(T>0));
            A(yy,xx)=sum(sum(B((end+1)-yy:end,(end+1)-xx:end).*C(1:yy...
                ,1:xx)))./((size(C(1:yy,1:xx),1)*(size(C(1:yy,1:xx),2)...
                ))-J);%left and top
        else if yy<=b(1) && xx>=b(2) && xx<=c(2)
                T=(B((end+1)-yy:end,1:b(2))==0);
                J=sum(sum(T>0));
                A(yy,xx)=sum(sum(B((end+1)-yy:end,1:b(2)).*C(1:yy,(xx-...
                    b(2)):(b(2)+(xx-b(2))-1))))./((size(C(1:yy,(xx-b...
                    (2)):(b(2)+(xx-b(2))-1)),1)*size(C(1:yy,(xx-b(2))...
                    :(b(2)+(xx-b(2))-1)),2))-J);
            else if yy>=b(1) && xx<=b(2) && yy<=c(1)
                    T=(B(1:b(1),(end+1)-xx:end)==0);
                    J=sum(sum(T>0));
                    A(yy,xx)=sum(sum(B(1:b(1),(end+1)-xx:end).*C((yy-b...
                        (1)):(b(1)+(yy-b(1))-1),1:xx)))./((size(C((yy-...
                        b(1)):(b(1)+(yy-b(1))-1),1:xx),1)*size(C((yy-b...
                        (1)):(b(1)+(yy-b(1))-1),1:xx),2))-J);
                else if yy>=b(1) && xx>=b(2) && xx<=c(2) && yy<=c(1)
                        T=(B==0);
                        J=sum(sum(T>0));
                        A(yy,xx)=sum(sum(B.*C((yy-b(1)):(b(1)+(yy-b(1)...
                            )-1),(xx-b(2)):(b(2)+(xx-b(2)))-1)))./((...
                            size(B,1)*size(B,2))-J);%middle
                    else if yy>b(1) && xx>=c(2) && yy<=c(1)
                            T=(B(1:b(1),1:(b(2)-(xx-c(2))))==0);
                            J=sum(sum(T>0));
                            A(yy,xx)=sum(sum(B(1:b(1),1:(b(2)-(xx-c(2)...
                                ))).*C(yy-b(1):b(1)+(yy-b(1))-1,(c(2)-...
                                b(2)+(xx-c(2))+1):end)))./((size(B(1:b...
                                (1),1:(b(2)-(xx-c(2)))),1)*size(B(1:b...
                                (1),1:(b(2)-(xx-c(2)))),2))-J);
                        else if yy>=c(1) && xx>=c(2)
                                T=(B(1:(b(1)-(yy-c(1))),1:(b(2)-(xx-c...
                                    (2))))==0);
                                J=sum(sum(T>0));
                                A(yy,xx)=sum(sum(B(1:(b(1)-(yy-c(1)))...
                                    ,1:(b(2)-(xx-c(2)))).*C((c(1)-b(1)...
                            +(yy-c(1))+1):end,(c(2)-b(2)+(xx-c...
                            (2))+1):end)))./((size(B(1:(b(1)-(...
                            yy-c(1))),1:(b(2)-(xx-c(2)))),1)*...
                            size(B(1:(b(1)-(yy-c(1))),1:(b(2)...
                            -(xx-c(2)))),2))-J);
                    else if yy<=b(1) && xx>=c(2)
                            T=(B((end+1)-yy:end,1:(b(2)-(xx-c...
                                (2))))==0);
                            J=sum(sum(T>0));
                            A(yy,xx)=sum(sum(B((end+1)-yy:end...
                                ,1:(b(2)-(xx-c(2)))).*C(1:yy,(...
                                c(2)-b(2)+(xx-c(2))+1):end)))...
                                ./((size(B((end+1)-yy:end,1:(b...
                                (2)-(xx-c(2)))),1)*size(B((end...
                                +1)-yy:end,1:(b(2)-(xx-c(2)))))...
                                ,2))-J);
                        else if yy>c(1) && xx>b(2) && xx<=c(2)
                                T=(B(1:(b(1)-(yy-c(1))),1:(b...
                                    (2)))==0);
                                J=sum(sum(T>0));
                                A(yy,xx)=sum(sum(B(1:(b(1)-(yy...
                                    -c(1))),1:(b(2))).*C((c(1)...
                                    -b(1)+(yy-c(1))+1):end,(xx...
                                    -b(2)):(xx-b(2)+b(2))-1)))...
                                    ./((size(B(1:(b(1)-(yy-c...
                                    (1))),1:(b(2))),1)*size(B...
                                    (1:(b(1)-(yy-c(1))),1:(b...
                                    (2))),2))-J);
                            else if yy>=c(1) && xx<=b(2)
                                    T=(B(1:(b(1)-(yy-c(1))),...
                                        end-xx+1:end)==0);
                                    J=sum(sum(T>0));
                                    A(yy,xx)=sum(sum(B(1:(b(1)...
                                        -(yy-c(1))),end-xx+1:...
                                        end).*C((c(1)-b(1)+(yy...
                                        -c(1))+1):end,1:xx)))...
                                        ./((size(B(1:(b(1)-(yy...
                                        -c(1))),end-xx+1:end)...
                                        ,1)*size(B(1:(b(1)-(yy...
                                        -c(1))),end-xx+1:end)...
                                        ,2))-J);
                                end
                            end
                        end
                    end
                end
            end
        end
    end
end
```

```
        end
        A1=A(rr:ll ,hh:gg);
        B_norm=B;
        C_norm=C;
end
end
```

Bibliography

[1] Panagiota Giannakopoulou. Four-wave mixing heterodyne interferometric imaging of gold nanoparticles in cells. *PhD Thesis, Cardiff University*, 2018.

[2] H. Ma, P. M. Bendix, and L. B. Oddershede. Large-scale orientation dependent heating from a single irradiated gold nanorod. *Nano Lett.*, 12:3954–3960, 2012.

[3] The demonstration of pneumococcal antigen in tissues by the use of fluorescent antibody. *The Journal of Immunology*, 45(3):159–170, 1942.

[4] Douglas C. Prasher, Virginia K. Eckenrode, William W. Ward, Frank G. Prendergast, and Milton J. Cormier. Primary structure of the aequorea victoria green-fluorescent protein. *Gene*, 111(2):229–233, February 1992.

[5] M Chalfie, Y Tu, G Euskirchen, WW Ward, and DC Prasher. Green fluorescent protein as a marker for gene expression. *Science*, 263(5148):802–805, 1994.

[6] Roger Heim and Roger Y Tsien. Engineering green fluorescent protein for improved brightness, longer wavelengths and fluorescence resonance energy transfer. *Current Biology*, 6(2):178 – 182, 1996.

[7] Stefan W. Hell and Jan Wichmann. Breaking the diffraction resolution limit by stimulated emission: stimulated-emission-depletion fluorescence microscopy. *Opt. Lett.*, 19(11):780–782, Jun 1994.

[8] Stefan W. Hell. Far-field optical nanoscopy. *Science*, 316(5828):1153–1158, 2007.

[9] Michael J Rust, Mark Bates, and Xiaowei Zhuang. Sub-diffraction-limit imaging by stochastic optical reconstruction microscopy (STORM). *Nature Methods*, 3(10):793–796, August 2006.

[10] Eric Betzig, George H. Patterson, Rachid Sougrat, O. Wolf Lindwasser, Scott Olenych, Juan S. Bonifacino, Michael W. Davidson, Jennifer Lippincott-Schwartz, and Harald F. Hess. Imaging intracellular fluorescent proteins at nanometer resolution. *Science*, 313(5793):1642–1645, 2006.

[11] Yasushi Sako, Shigeru Minoghchi, and Toshio Yanagida. Single-molecule imaging of EGFR signalling on the surface of living cells. *Nature Cell Biology*, 2(3):168–172, February 2000.

[12] Neveen A. Hosny, Mingying Song, John T. Connelly, Simon Ameer-Beg, Martin M. Knight, and Ann P. Wheeler. Super-resolution imaging strategies for cell biologists using a spinning disk microscope. *PLoS ONE*, 8(10):e74604, October 2013.

[13] Otto S. Wolfbeis. An overview of nanoparticles commonly used in fluorescent bioimaging. *Chemical Society Reviews*, 44(14):4743–4768, 2015.

[14] Gregory V. Hartland. Optical studies of dynamics in noble metal nanostructures. *Chemical Reviews*, 111(6):3858–3887, 2011. PMID: 21434614.

[15] Subinoy Rana, Avinash Bajaj, Rubul Mout, and Vincent M. Rotello. Monolayer coated gold nanoparticles for delivery applications. *Advanced Drug Delivery Reviews*, 64(2):200 – 216, 2012. Biological Interactions of Nanoparticles.

[16] Fen-Ying Kong, Jin-Wei Zhang, Rong-Fang Li, Zhong-Xia Wang, Wen-Juan Wang, and Wei Wang. Unique roles of gold nanoparticles in drug delivery, targeting and imaging applications. *Molecules*, 22(9), 2017.

[17] Partha Ghosh, Gang Han, Mrinmoy De, Chae Kyu Kim, and Vincent M. Rotello. Gold nanoparticles in delivery applications. *Advanced Drug Delivery Reviews*, 60(11):1307 – 1315, 2008. Inorganic Nanoparticles in Drug Delivery.

[18] Erik C. Dreaden, Alaaldin M. Alkilany, Xiaohua Huang, Catherine J. Murphy, and Mostafa A. El-Sayed. The golden age: gold nanoparticles for biomedicine. *Chem. Soc. Rev.*, 41:2740–2779, 2012.

[19] Elodie Boisselier and Didier Astruc. Gold nanoparticles in nanomedicine: preparations, imaging, diagnostics, therapies and toxicity. *Chem. Soc. Rev.*, 38:1759–1782, 2009.

[20] Erik C. Dreaden, Megan A. Mackey, Xiaohua Huang, Bin Kang, and Mostafa A. El-Sayed. Beating cancer in multiple ways using nanogold. *Chem. Soc. Rev.*, 40:3391–3404, 2011.

[21] Alaaldin M. Alkilany and Catherine J. Murphy. Toxicity and cellular uptake of gold nanoparticles: what we have learned so far? *Journal of Nanoparticle Research*, 12(7):2313–2333, April 2010.

[22] Gora M'Baye, Yves Mély, Guy Duportail, and Andrey S. Klymchenko. Liquid ordered and gel phases of lipid bilayers: Fluorescent probes reveal close fluidity but different hydration. *Biophysical Journal*, 95(3):1217–1225, August 2008.

[23] Erdinc Sezgin, Ilya Levental, Satyajit Mayor, and Christian Eggeling. The mystery of membrane organization: composition, regulation and roles of lipid rafts. *Nature Reviews Molecular Cell Biology*, 18(6):361–374, March 2017.

[24] Sung-Tae Yang, Volker Kiessling, and Lukas K. Tamm. Line tension at lipid phase boundaries as driving force for HIV fusion peptide-mediated fusion. *Nature Communications*, 7(1), April 2016.

[25] Mihaela Delcea, Nadine Sternberg, Alexey M. Yashchenok, Radostina Georgieva, Hans Baumler, Helmuth Mohwald, and Andre G. Skirtach. Nanoplasmonics for dual-molecule release through nanopores in the membrane of red blood cells. *ACS Nano*, 6(5):4169–4180, 2012. PMID: 22463598.

[26] Wei Qian, Xiaohua Huang, Bin Kang, and Mostafa A. El-Sayed. Dark-field light scattering imaging of living cancer cell component from birth through division using bioconjugated gold nanoprobes. *Journal of Biomedical Optics*, 15(4):1 – 9 – 9, 2010.

[27] Hiroshi Ueno, So Nishikawa, Ryota Iino, Kazuhito V. Tabata, Shouichi Sakakihara, Toshio Yanagida, and Hiroyuki Noji. Simple dark-field microscopy with nanometer spatial precision and microsecond temporal resolution. *Biophysical Journal*, 98(9):2014 – 2023, 2010.

[28] Mengmeng Liu, Qian Li, Le Liang, Jiang Li, Kun Wang, Jiajun Li, Min Lv, Nan Chen, Haiyun Song, Joon Lee, Jiye Shi, Lihua Wang, Ratnesh Lal, and Chunhai Fan. Real-time visualization of clustering and intracellular transport of gold nanoparticles by correlative imaging. *Nature Communications*, 8(1), May 2017.

[29] David Boyer, Philippe Tamarat, Abdelhamid Maali, Brahim Lounis, and Michel Orrit. Photothermal imaging of nanometer-sized metal particles among scatterers. *Science*, 297(5584):1160–1163, 2002.

[30] Stéphane Berciaud, Laurent Cognet, Gerhard A. Blab, and Brahim Lounis. Photothermal heterodyne imaging of individual nonfluorescent nanoclusters and nanocrystals. *Phys. Rev. Lett.*, 93:257402, Dec 2004.

[31] Stéphane Berciaud, David Lasne, Gerhard A. Blab, Laurent Cognet, and Brahim Lounis. Photothermal heterodyne imaging of individual metallic nanoparticles: Theory versus experiment. *Phys. Rev. B*, 73:045424, Jan 2006.

[32] David Lasne, Gerhard A. Blab, Stephane Berciaud, Martin Heine, Laurent Groc, Daniel Choquet, Laurent Cognet, and Brahim Lounis. Single nanoparticle photothermal tracking (snapt) of 5-nm gold beads in live cells. *Biophysical Journal*, 91(12):4598 – 4604, 2006.

[33] David Lasne, Gerhard. A. Blab, Francesca De Giorgi, François Ichas, Brahim Lounis, and Laurent Cognet. Label-free optical imaging of mitochondria in live cells. *Opt. Express*, 15(21):14184–14193, Oct 2007.

[34] Christophe Pache, Noelia L. Bocchio, Arno Bouwens, Martin Villiger, Corinne Berclaz, Joan Goulley, Matthew I. Gibson, Christian Santschi, and Theo Lasser. Fast three-dimensional imaging of gold nanoparticles in living cells with photothermal optical lock-in optical coherence microscopy. *Opt. Express*, 20(19):21385–21399, Sep 2012.

[35] Jaime Ortega-Arroyo and Philipp Kukura. Interferometric scattering microscopy (iscat): new frontiers in ultrafast and ultrasensitive optical microscopy. *Phys. Chem. Chem. Phys.*, 14:15625–15636, 2012.

[36] Jaime Ortega Arroyo, Daniel Cole, and Philipp Kukura. Interferometric scattering microscopy and its combination with single-molecule fluorescence imaging. *Nature Protocols*, 11(4):617–633, March 2016.

[37] Benjamin T. Miles, Elizabeth C. Robinson, Erik M. H. P. van Dijk, Ian D. Lindsay, Niek F. van Hulst, and Henkjan Gersen. Sensitivity of interferometric cross-polarization microscopy for nanoparticle detection in the near-infrared. *ACS Photonics*, 2(12):1705–1711, 2015.

[38] B. T. Miles, A. B. Greenwood, D. Benito-Alifonso, H. Tanner, M. C. Galan, P. Verkade, and H. Gersen. Direct evidence of lack of colocalisation of fluorescently labelled gold labels used in correlative light electron microscopy. *Scientific Reports*, 7:44666, 2017.

[39] Lukas M. Payne, Wolfgang Langbein, and Paola Borri. Polarization-resolved extinction and scattering cross-sections of individual gold nanoparticles measured by wide-field microscopy on a large ensemble. *Applied Physics Letters*, 102(13):131107, 2013.

[40] Lukas Payne, George Zoriniants, Francesco Masia, Kenton P. Arkill, Paul Verkade, Darren Rowles, Wolfgang Langbein, and Paola Borri. Optical microspectroscopy of single metallic nanoparticles: quantitative extinction and transient resonant four-wave mixing. *Faraday Discuss.*, 184:305–320, 2015.

[41] Lukas M. Payne, Wolfgang Langbein, and Paola Borri. Wide-field imaging of single-nanoparticle extinction with sub-nm^2 sensitivity. *Phys. Rev. Applied*, 9:034006, Mar 2018.

[42] Attilio Zilli, Wolfgang Langbein, and Paola Borri. Quantitative measurement of the optical cross sections of single nano-objects by correlative transmission and scattering microspectroscopy. *ACS Photonics*, 6(8):2149–2160, 2019.

[43] Wei Min, Sijia Lu, Markus Rueckel, Gary R. Holtom, and X. Sunney Xie. Near-degenerate four-wave-mixing microscopy. *Nano Letters*, 9(6):2423–2426, June 2009.

[44] Yong Wang, Xuejun Liu, Aaron R. Halpern, Kyunghee Cho, Robert M. Corn, and Eric O. Potma. Wide-field, surface-sensitive four-wave mixing microscopy of nanostructures. *Applied Optics*, 51(16):3305, May 2012.

[45] Yong Wang, Chia-Yu Lin, Alexei Nikolaenko, Varun Raghunathan, and Eric O. Potma. Four-wave mixing microscopy of nanostructures. *Advances in Optics and Photonics*, 3(1):1, September 2010.

[46] Francesco Masia, Wolfgang Langbein, Peter Watson, and Paola Borri. Resonant four-wave mixing of gold nanoparticles for three-dimensional cell microscopy. *Opt. Lett.*, 34(12):1816–1818, Jun 2009.

[47] Francesco Masia, Wolfgang Langbein, and Paola Borri. Measurement of the dynamics of plasmons inside individual gold nanoparticles using a femtosecond phase-resolved microscope. *Phys. Rev. B*, 85:235403, Jun 2012.

[48] George Zoriniants, Francesco Masia, Naya Giannakopoulou, Wolfgang Langbein, and Paola Borri. Background-free 3d nanometric localization and sub-nm asymmetry detection of single plasmonic nanoparticles by four-wave mixing interferometry with optical vortices. *Phys. Rev. X*, 7:041022, Oct 2017.

[49] Yong Keun Park, Christian Depeursinge, and Gabriel Popescu. Quantitative phase imaging in biomedicine. *Nature Photonics*, 12(10):578–589, 10 2018.

[50] Chris Edwards, Amir Arbabi, Basanta Bhaduri, Xiaozhen Wang, Raman Ganti, Peter J. Yunker, Arjun G. Yodh, Gabriel Popescu, and Lynford L. Goddard. Measuring the nonuniform evaporation dynamics of sprayed sessile microdroplets with quantitative phase imaging. *Langmuir*, 31(40):11020–11032, 2015. PMID: 26389788.

[51] Yann Cotte, Fatih Toy, Pascal Jourdain, Nicolas Pavillon, Daniel Boss, Pierre Magistretti, Pierre Marquet, and Christian Depeursinge. Marker-free phase nanoscopy. *Nature Photonics*, 7(2):113–117, January 2013.

[52] Onur Mudanyali, Euan McLeod, Wei Luo, Alon Greenbaum, Ahmet F. Coskun, Yves Hennequin, Cédric P. Allier, and Aydogan Ozcan. Wide-field optical detection of nanoparticles using on-chip microscopy and self-assembled nanolenses. *Nature Photonics*, 7(3):247–254, January 2013.

[53] Natan T. Shaked, Lisa L. Satterwhite, George A. Truskey, Adam P. Wax, and Marilyn J. Telen. Quantitative microscopy and nanoscopy of sickle red blood

cells performed by wide field digital interferometry. *Journal of Biomedical Optics*, 16(3):1 – 4 – 4, 2011.

[54] G. Binnig, C. F. Quate, and Ch. Gerber. Atomic force microscope. *Phys. Rev. Lett.*, 56:930–933, Mar 1986.

[55] PK Hansma, VB Elings, O Marti, and CE Bracker. Scanning tunneling microscopy and atomic force microscopy: application to biology and technology. *Science*, 242(4876):209–216, 1988.

[56] Andrea Alessandrini and Paolo Facci. Phase transitions in supported lipid bilayers studied by afm. *Soft Matter*, 10:7145–7164, 2014.

[57] C.I. McPhee, G. Zoriniants, W. Langbein, and P. Borri. Measuring the lamellarity of giant lipid vesicles with differential interference contrast microscopy. *Biophysical Journal*, 105(6):1414 – 1420, 2013.

[58] Iestyn Pope, Lukas Payne, George Zoriniants, Evan Thomas, Oliver Williams, Peter Watson, Wolfgang Langbein, and Paola Borri. Coherent anti-stokes raman scattering microscopy of single nanodiamonds. *Nat Nano*, 9(11):940–946, Nov 2014. Article.

[59] Michael T. Carlson, Aurangzeb Khan, and Hugh H. Richardson. Local temperature determination of optically excited nanoparticles and nanodots. *Nano Letters*, 11(3):1061–1069, 2011. PMID: 21306114.

[60] Guillaume Baffou, Pierre Bon, Julien Savatier, Julien Polleux, Min Zhu, Marine Merlin, HervÃ© Rigneault, and Serge Monneret. Thermal imaging of nanostructures by quantitative optical phase analysis. *ACS Nano*, 6(3):2452–2458, 2012. PMID: 22305011.

[61] Yeonee Seol, Amanda E. Carpenter, and Thomas T. Perkins. Gold nanoparticles: enhanced optical trapping and sensitivity coupled with significant heating. *Optics Letters*, 31(16):2429, July 2006.

[62] Hiroshi Ishiwata, Masahide Itoh, and Toyohiko Yatagai. A new method of three-dimensional measurement by differential interference contrast microscope. *Optics Communications*, 260(1):117 – 126, 2006.

[63] E. B. Van Munster, L. J. Van Vliet, and J. A. Aten. Reconstruction of optical pathlength distributions from images obtained by a wide-field differential interference contrast microscope. *Journal of Microscopy*, 188(2):149–157, 1997.

[64] Van Munster, Winter, and Aten. Measurement-based evaluation of optical pathlength distributions reconstructed from simulated differential interference contrast images. *Journal of Microscopy*, 191(2):170–176, 1998.

[65] Shan Shan Kou, Laura Waller, George Barbastathis, and Colin J. R. Sheppard. Transport-of-intensity approach to differential interference contrast (ti-dic) microscopy for quantitative phase imaging. *Opt. Lett.*, 35(3):447–449, Feb 2010.

[66] Krisztian Koos, Mólnár Jósef, Lóránd Kelemen, Gábor Támás, and Peter Horvath. Dic image reconstruction using an energy minimization framework to visualize optical path length distribution. *Scientific Reports*, 6(30420), 2016.

[67] E. Dulkeith, A. C. Morteani, T. Niedereichholz, T. A. Klar, J. Feldmann, S. A. Levi, F. C. J. M. van Veggel, D. N. Reinhoudt, M. Möller, and D. I. Gittins. Fluorescence quenching of dye molecules near gold nanoparticles: Radiative and nonradiative effects. *Phys. Rev. Lett.*, 89:203002, Oct 2002.

[68] Irawati K. Kandela and Ralph M. Albrecht. Fluorescence quenching by colloidal heavy metals nanoparticles: Implications for correlative fluorescence and electron microscopy studies. *Scanning*, 29(4):152–161, 2007.

[69] Irawati K. Kandela, Reiner Bleher, and Ralph M. Albrecht. Multiple correlative immunolabeling for light and electron microscopy using fluorophores and colloidal metal particles. *Journal of Histochemistry & Cytochemistry*, 55(10):983–990, 2007. PMID: 17652267.

[70] Pascal de Boer, Jacob P Hoogenboom, and Ben N G Giepmans. Correlated light and electron microscopy: ultrastructure lights up! *Nature Methods*, 12:503–513, 2015.

[71] S. Bolte and F. P. Cordeliéres. A guided tour into subcellular colocalization analysis in light microscopy. *Journal of Microscopy*, 224(3):213–232, 2006.

[72] G. Baffou, R. Quidant, and C. Girard. Thermoplasmonics modeling, a greens function approach. *Phys. Rev. B*, 82:165424, 2010.

[73] Gustav Mie. Beiträge zur optik trüber medien, speziell kolloidaler metallösungen. *Annalen der Physik*, 330(3):377–445, 1908.

[74] C. Bohren and D. R. Huffman. *Absorption and Scattering of Light by Small Particles.* Wiley Science Paperback Series, 1998.

[75] Xiaohua Huang and Mostafa A. El-Sayed. Gold nanoparticles: Optical properties and implementations in cancer diagnosis and photothermal therapy. *Journal of Advanced Research*, 1(1):13–28, January 2010.

[76] Prashant K. Jain, Kyeong Seok Lee, Ivan H. El-Sayed, and Mostafa A. El-Sayed. Calculated absorption and scattering properties of gold nanoparticles of different size, shape, and composition: Applications in biological imaging and biomedicine. *The Journal of Physical Chemistry B*, 110(14):7238–7248, 2006. PMID: 16599493.

[77] M. A. van Dijk, A. L. Tchebotareva, M. Orrit, M. Lippitz, S. Berciaud, D. Lasne, L. Cognet, and B. Lounis. Absorption and scattering microscopy of single metal nanoparticles. *Phys. Chem. Chem. Phys.*, 8:3486–3495, 2006.

[78] Lukas Payne. Optical extinction and coherent multiphoton micro-spectroscopy of single nanoparticles. *PhD Thesis, Cardiff University*, 2015.

[79] A. O. Govorov, W. Zhang, T. Skeini, H. Richardson, J. Lee, and N. A. Kotov. Gold nanoparticle ensembles as heaters and actuators: melting and collective plasmon resonances. *Nanoscale Res. Lett.*, 1:84–90, 2006.

[80] Guillaume Baffou, Romain Quidant, and F. Javier GarcÃa de Abajo. Nanoscale control of optical heating in complex plasmonic systems. *ACS Nano*, 4(2):709–716, 2010. PMID: 20055439.

[81] Edward J. Sayers, Johannes P. Magnusson, Paul R. Moody, Francesca Mastrotto, Claudia Conte, Chiara Brazzale, Paola Borri, Paolo Caliceti, Peter Watson, Giuseppe Mantovani, Jonathan Aylott, Stefano Salmaso, Arwyn T. Jones, and Cameron Alexander. Switching of macromolecular ligand display by thermoresponsive polymers mediates endocytosis of multiconjugate nanoparticles. *Bioconjugate Chemistry*, 29(4):1030–1046, 2018. PMID: 29481068.

[82] Paul R Moody, Edward J Sayers, Johannes P Magnusson, Cameron Alexander, Paola Borri, Peter Watson, and Arwyn T Jones. Receptor crosslinking: A general method to trigger internalization and lysosomal targeting of therapeutic receptor:ligand complexes. *Molecular Therapy*, 23(12):1888–1898, December 2015.

[83] Muhammad H Islam. Towards optical biosensors based on whispering-gallery modes in microsphere resonators. *PhD Thesis, Cardiff University*, 2018.

[84] Gary P. Misson. A mueller matrix model of haidinger's brushes. *Ophthalmic and Physiological Optics*, 23(5):441–447, September 2003.

[85] R. B. Blackman and J. W. Tukey. The measurement of power spectra from the point of view of communications engineering — part i. *The Bell System Technical Journal*, 37(1):185–282, January 1958.

[86] Juan Martinez-Carranza, Konstantinos Falaggis, and Tomasz Kozacki. Fast and accurate phase-unwrapping algorithm based on the transport of intensity equation. *Appl. Opt.*, 56(25):7079–7088, Sep 2017.

[87] David Regan. Measurement of thickness and phase transitions in supported lipid bilayers using quantitative interference contrast microscopy. *PhD Thesis, Cardiff University*, 2019.

[88] David Regan, Joseph Williams, Paola Borri, and Wolfgang Langbein. Lipid bilayer thickness measured by quantitative dic reveals phase transitions and effects of substrate hydrophilicity. *Langmuir*, 35(43):13805–13814, 2019. PMID: 31483674.

[89] David Regan, Joseph Williams, Francesco Masia, Paola Borri, and Wolfgang Langbein. Measuring sub-nanometre thickness changes during phase transitions of supported lipid bilayers with quantitative differential interference contrast microscopy. *Proceedings of SPIE*, 10887, 2019.

[90] Stephanie Tortorella and Tom C. Karagiannis. Transferrin receptor-mediated endocytosis: A useful target for cancer therapy. *The Journal of Membrane Biology*, 247(4):291–307, Apr 2014.

[91] Liangfang Zhang, Tighe A. Spurlin, Andrew A. Gewirth, and Steve Granick. Electrostatic stitching in gel-phase supported phospholipid bilayers. *The Journal of Physical Chemistry B*, 110(1):33–35, January 2006.

Publications, oral and poster presentations

Publications

David Regan, Joseph Williams, Francesco Masia, Paola Borri and Wolfgang Langbein. Measuring sub-nanometre thickness changes during phase transitions of supported lipid bilayers with quantitative differential interference contrast microscopy. *Proceedings of SPIE*, 10887, 2019.

David Regan, Joseph Williams, Paola Borri and Wolfgang Langbein. Lipid bilayer thickness measured by quantitative DIC reveals phase transitions and effects of substrate hydrophilicity. *Langmuir*, accepted 2019.

Naya Giannakopoulou, Joseph B. Williams, Paul R. Moody, Edward J. Sayers, Johannes P. Magnusson, Iestyn Pope, Lukas Payne, Cameron Alexander, Arwyn T. Jones, Wolfgang Langbein, Peter Watson and Paola Borri. Four-wave-mixing microscopy reveals non-colocalisation between gold nanoparticles and fluorophore conjugates inside cells. *Nanoscale*, accepted 2019.

Oral and poster presentations

Joseph Williams, David Regan, George Zorinyants, Wolfgang Langbein and Paola Borri. qDIC - Extracting quantitative information from Differential Interference Contrast (DIC) images. Poster presentation at the BioNano Photonics Symposium, Cardiff, UK (18-19 September 2017).

Joseph Williams, Francesco Masia, David Regan, George Zoriniants, Wolfgang Langbein and Paola Borri. qDIC - Extracting quantitative information from Differential Interference Contrast (DIC) Images. Oral presentation at Photon 2018, Birmingham, UK (3-6 September 2018).